論文 / 著書情報
Article / Book Information

題目(和文)	電波透過性に優れたコンクリートの実現に向けたジオポリマーの適用検討
Title(English)	Investigation on the Application of Geopolymer for Achieving Concrete with High Radio Wave Transparency
著者(和文)	坂本亮
Author(English)	Ryo Sakamoto
出典(和文)	学位:博士(工学), 学位授与機関:東京科学大学, 報告番号:甲第340号, 授与年月日:2025年3月26日, 学位の種別:課程博士, 審査員:千々和 伸浩,岩波 光保,林 幸,松﨑 裕,丸山 泰蔵,齋藤 健太郎
Citation(English)	Degree:Doctor (Engineering), Conferring organization: Institute of Science Tokyo, Report number:甲第340号, Conferred date:2025/3/26, Degree Type:Course doctor, Examiner:,,,,,
学位種別(和文)	博士論文
Type(English)	Doctoral Thesis

Investigation on the Application of Geopolymer for Achieving Concrete with High Radio Wave Transparency

電波透過性に優れたコンクリートの実現に向けたジオポリマーの適用検討

Ryo Sakamoto

Supervisor: Professor Nobuhiro Chijiwa

Department of Civil and Environmental Engineering

Institute of Science Tokyo

A dissertation submitted in partial fulfillment of the requirements

for the degree of doctor of engineering

February 2025

Table of Contents

Table of Figures

CHAPTER 1. INTRODUCTION

1.1. Background

In recent years, advancements in ICT and other fields have ushered in an "era of significant transformation," characterized by daily changes in societal and economic structures. As domestic and global challenges intensify and become increasingly complex, the need to promote science, technology, and innovation has grown substantially. In Japan, the Fifth Science and Technology Basic Plan[(1)] emphasized the importance of Japan spearheading this transformative era by creating major changes of its own. A central pillar of this plan was the strong promotion of "Society 5.0," aimed at realizing a "super-smart society" ahead of the rest of the world. The Sixth Science, Technology, and Innovation Basic Plan[(2)] further elaborated on specific policies to achieve Society 5.0.

A "super-smart society" is defined as a society that "provides the necessary goods and services to the right people at the right time and in the right amount, finely addressing diverse social needs. It is a society where everyone can receive high-quality services and live vibrant, comfortable lives, transcending differences in age, gender, region, and language." Society 5.0 is conceptualized as a human-centered society that achieves both economic development and the resolution of social challenges through a system that deeply integrates cyber space (virtual space) and physical space (real space). This system involves aggregating vast amounts of data from sensors in the physical space into the cyber space, where artificial intelligence (AI) analyzes this big data and feeds the results back to humans in the physical space in various forms[(3)].

In Society 5.0, all societal elements are constructed as digital twins within the cyber space, enabling the redesign of institutions, business frameworks, urban planning, and regional development. These redesigned elements are then reflected in the physical space to transform society. Achieving this transformation requires a robust foundation for collecting and accumulating high-quality data in a form that allows for advanced analysis, as well as leveraging mathematical models and data analytics technologies for in-depth cyber space analysis[(2)].

Currently, "smart cities" are being promoted as pioneering examples of Society 5.0. These sustainable cities and regions utilize new technologies, such as ICT, to enhance management processes (planning, development, and operation) to address various urban and regional challenges while continually creating new value in terms of comfort and convenience.

To build smart cities and ultimately realize Society 5.0, information and communication technologies, as well as communication infrastructures that bridge the cyber and physical spaces, are indispensable. The commercialization of the fifth-generation mobile communication system (5G) in 2020 has enabled wireless communication using higher frequency bands, such as millimeter waves (~60 GHz), in addition to conventional microwave bands (~2 GHz). By around 2030, the next-generation sixth-generation mobile communication system (6G) is expected to be commercialized.

These systems are characterized by ultra-high speed, low latency, ultra-reliability, and the ability to connect a massive number of devices simultaneously, playing a critical role in real-time data transmission within Society 5.0.

In Society 5.0, the cyber and physical spaces are seamlessly connected through a cyber-physical system (CPS). The cyber space includes big data and artificial intelligence (AI), while the physical space encompasses sensors such as cameras and LiDAR, databases like dynamic maps, decision-making edge computing (e.g., Multi-access Edge Computing, MEC), and actuators such as vehicles. These elements are interconnected via 5G/6G to enable the realization of Society 5.0 (**Figure 1-1**)[4]. Therefore, a stable and extensive 5G/6G communication environment is essential, and its early deployment is a pressing requirement.

A significant obstacle in establishing 5G/6G communication environments is concrete, widely used in infrastructure and high-rise buildings. High-frequency signals are highly directional and easily affected by obstacles. Concrete, in particular, has low radio wave transparency, making it challenging to secure service areas in building shadows or indoors (**Figure 1-2**)[5-10]. While current solutions involve improving and expanding base stations and antennas, their effectiveness is limited. Moreover, with the anticipated adoption of communication standards using even higher frequency bands, such as 6G and 7G, this issue is expected to become more severe, necessitating fundamental solutions.

Concrete is an essential construction material for large-scale structures such as infrastructure and high-rise buildings due to its ability to achieve high compressive strength and durability at low cost compared to other construction materials. Therefore, replacing concrete with alternative materials solely to enhance radio wave transparency is not a practical solution for such large-scale structures. Consequently, a fundamental approach to addressing this issue requires improving the radio wave transparency of concrete members while maintaining the necessary mechanical properties and durability.

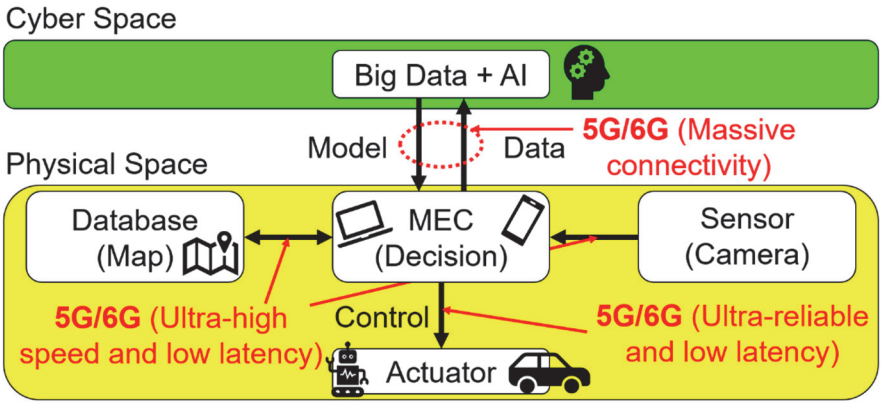

Figure 1-1 Schematic diagram of the super smart society (Society 5.0)**(1)**

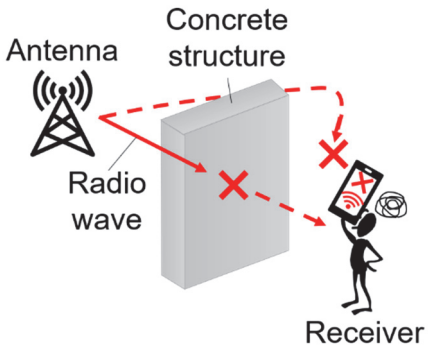

Figure 1-2 Schematic diagram of the shielding of radio waves by concrete structures

1.2. Objective and positioning

The objective of this research is to develop concrete that exhibits high radio wave transparency while maintaining sufficient mechanical performance as a construction material. When considering the use of concrete in construction, reinforcement materials such as steel bars are incorporated to compensate for its low tensile strength. Thus, realizing concrete members with excellent radio wave transparency necessitates evaluating the radio wave transparency of both the concrete and the reinforcement materials.

Figure 1-3 illustrates the research concept. First, for concrete, the mix proportions will be optimized to significantly enhance its radio wave transparency while ensuring adequate mechanical performance for use as a building material. Next, for reinforcement materials, the feasibility of controlling radio wave transparency through material selection and arrangement optimization will be explored. Based on these considerations, the study ultimately aims to propose a design methodology for reinforced concrete members that balances both mechanical and radio wave transparency performance.

This research focuses on the concrete component, investigating methods to significantly enhance its radio wave transparency while maintaining mechanical performance. As will be discussed in detail in CHAPTER 2, reducing the moisture content in concrete is key to improving its radio wave transparency. This research examines the effectiveness of using geopolymer (GP) as a means of reducing moisture and enhancing radio wave transparency. Additionally, since the complete properties and mechanisms of GP remain unclear, investigations were conducted on the mechanical properties of GP and analytical methods to elucidate the mechanisms governing both its radio wave transparency and mechanical properties, thereby assessing its applicability in concrete structural members.

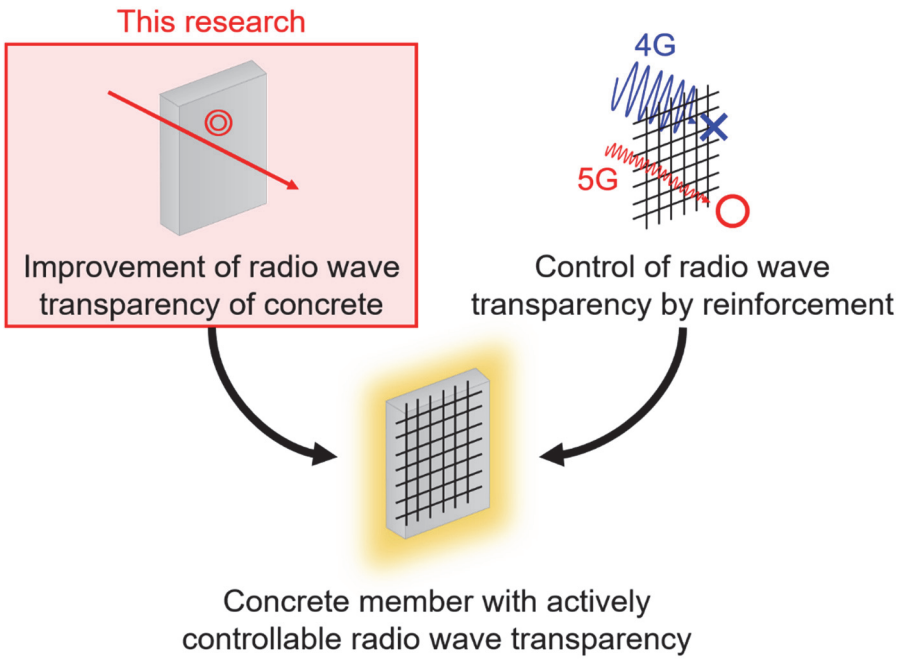

Figure 1-3 Schematic diagram of the research concept and the positioning of this research

1.3. Geopolymer overview

Geopolymer (GP) is a solidified material primarily formed through the polycondensation reaction between aluminosilicate powders (active fillers) such as fly ash (FA) and ground granulated blast furnace slag (BS) and alkaline silica solutions (alkaline solutions) such as sodium silicate and sodium hydroxide. Its solidification mechanism differs entirely from the hydration reaction of cement, as metal ions dissolved from active fillers interact with sodium silicate, leading to dehydration and the cross-linking of silicate complexes into polymers, thereby forming an inorganic adhesive structure that binds the active filler particles[(11)] (**Figure 1-4**).

Concrete that uses GP as a binder instead of cement exhibits significantly lower CO_2 emissions during production compared to conventional concrete. Additionally, it enables the effective utilization of industrial by-products, offers excellent resistance to strong acids and high temperatures, and possesses the capability to immobilize hazardous substances such as heavy metals and cesium. These characteristics make GP a promising material for achieving a low-carbon society, applications in extreme environments such as highly acidic or high-temperature conditions, and further development into new environmental remediation technologies[(12)].

This research focuses on GP's unique solidification mechanism via dehydration reactions. As mentioned in Section 1.2, reducing the moisture content in concrete is key to improving radio wave transparency. Since GP solidifies through dehydration reactions, no hydration products remain within the solidified material, which is expected to reduce moisture content and subsequently enhance radio

wave transparency compared to cementitious materials. Details will be discussed in CHAPTER 2.

While GP is advancing toward practical applications as a concrete material, there remain numerous academic challenges that must be addressed to expand its use. In particular, shrinkage and other time-dependent deformations can lead to cracking, which affects not only the mechanical performance of structural elements but also their radio wave transparency. However, the time-dependent deformation characteristics of GP remain largely unexplored and lack systematic study. Therefore, to ensure the long-term retention of both high radio wave transparency and mechanical performance, this study focuses on elucidating the time-dependent deformation behavior of GP, as discussed in CHAPTER 3.

The properties of GP, including radio wave transparency and time-dependent deformation characteristics, are believed to be significantly influenced by its microstructure, including pore structure, skeletal strength, and skeletal composition. However, due to the amorphous nature of its primary reaction products and the wide range of influencing factors, the microstructural formation mechanism of GP has not been well understood. This study aims to clarify the relationship between radio wave transparency, time-dependent deformation characteristics, and microstructure by investigating the formation process of reaction products. Furthermore, an analytical method was examined to visualize these growth processes, as detailed in CHAPTER 4.

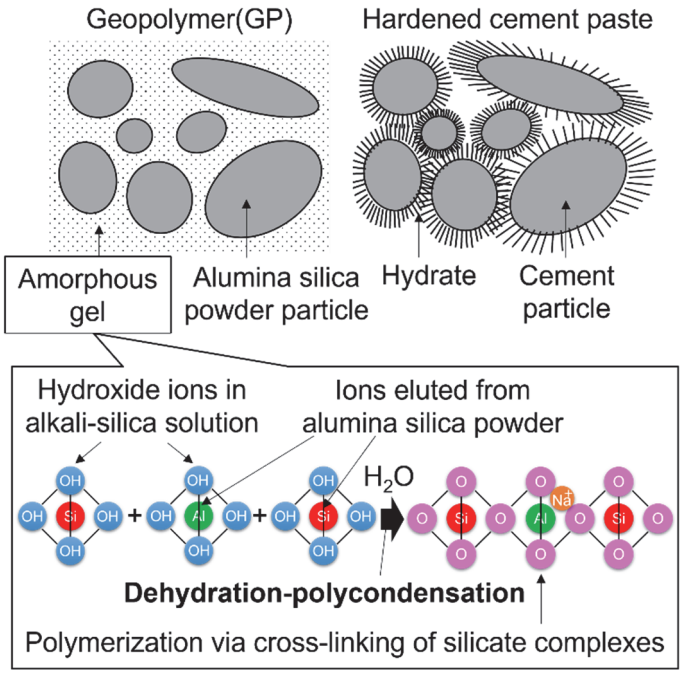

Figure 1-4 Schematic diagram of geopolymer solidified products and solidification mechanism

1.4. Impact

Concrete is primarily recognized for its structural performance, and its interaction with electromagnetic waves, including radio waves, remains largely unexplored. However, electromagnetic waves are already used for the non-destructive testing of concrete structures, and research to elucidate the relationship between electromagnetic waves and concrete properties is advancing to improve inspection accuracy[13, 14]. Furthermore, concrete is utilized in nuclear facilities such as reactor buildings and containment vessels for radiation shielding, and research is ongoing to maintain its shielding performance[15–19]. Interest in the shielding properties of concrete against electromagnetic waves beyond radiation has also increased. Tanai et al.[20, 21] demonstrated the potential for shielding specific frequency electromagnetic waves by adjusting the reinforcement arrangement in reinforced concrete and modifying concrete's dielectric properties. Additionally, studies have investigated altering concrete's surface geometry or mix proportions to shield or reflect electromagnetic waves[22–24]. Furthermore, with the emergence of ultra-smart societies as discussed in Section 1.1, studies on estimating radio wave propagation environments based on concrete's electromagnetic properties are actively progressing[25–29]. While research has focused on enhancing concrete's shielding performance under the assumption that "concrete does not transmit electromagnetic waves," no studies have aimed to improve its radio wave transparency.

This study challenges the conventional notion that "concrete does not transmit electromagnetic waves." By improving concrete's radio wave transparency, this research not only reduces radio wave shielding by buildings but also enables control over the shielding and transmission properties of buildings, allowing users to actively manage radio wave propagation environments through construction materials. This approach could lead to more flexible communication system designs, for instance, allowing higher-frequency radio waves (above 5G) to pass through while shielding lower-frequency waves (below 4G). Through this study, concrete buildings can gain new value as communication infrastructure, contributing to the development of novel communication system designs incorporating building structures. Additionally, research on GP conducted in this study is expected to advance understanding of GP's properties and mechanisms, ultimately facilitating its broader adoption as a construction material.

1.5. Thesis structure

This paper consists of five chapters (**Figure 1-5**).

CHAPTER 1 presents the background of this research, outlining challenges in wireless communication from the present to the future. It also describes the objective, positioning, and potential societal impact, along with an overview of GP and its relevance to the following chapters.

CHAPTER 2 discusses various methods for improving the radio wave transparency of

unreinforced concrete members, including an evaluation of the effectiveness of GP application.

CHAPTER 3 investigates the time-dependent deformation characteristics of various geopolymer (GP) materials, including low water-to-binder ratio (W/P) GP, which was identified in CHAPTER 2 as having the potential for high radio wave transparency, influencing their long-term radio wave transparency and mechanical performance.

CHAPTER 4 focuses on the formation mechanisms of GP microstructures, particularly the growth process of reaction products. An analytical method for visualizing these growth processes is explored.

CHAPTER 5 integrates the findings from CHAPTER 2, 3, and 4 to propose concrete with both high radio wave transparency and sufficient mechanical performance as a construction material. Furthermore, future research prospects for its practical application are discussed.

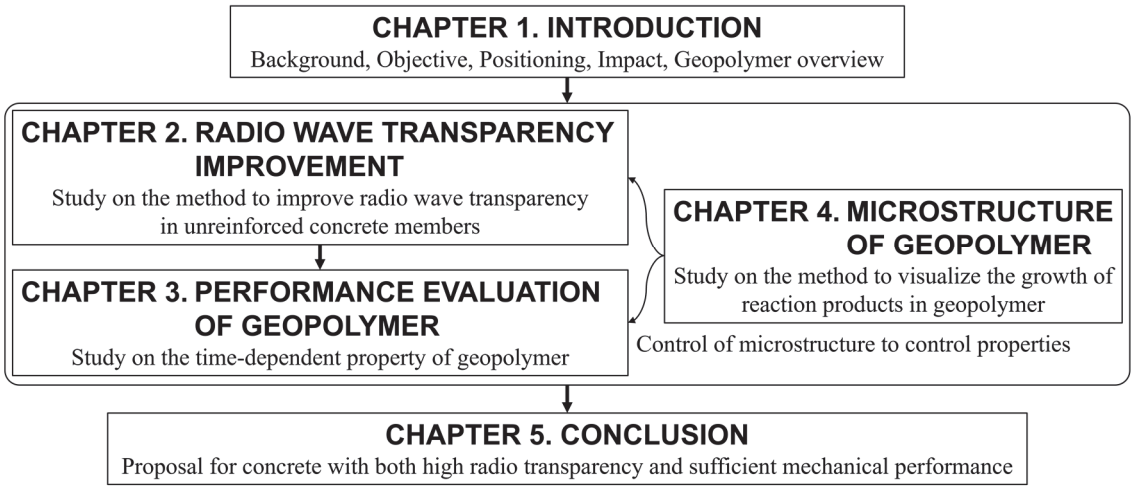

Figure 1-5 Thesis structure

References

(1) 内閣府. 第 5 期科学技術基本計画. 2016.

(2) 内閣府. 第 6 期科学技術・イノベーション基本計画. 2021.

(3) 内閣府. 第 5 期科学技術基本計画で提唱した Society 5.0 のコンセプト. 2016.

(4) Sakaguchi, K., Nakazato, J., Kubota, K., Fukuda, E., Kuchitsu, M., Masuko, S. Evolution of B5G/6G Empowered by Edge Computing towards Super Smart Society. The Journal of Institute of Electronics, Information and Communication Engineers. 2023, Vol. 106, No. 2, pp. 129–135.

(5) Horikoshi, J, Tanaka, K., Morinaga, T. 1.2 GHz band wave propagation measurements in concrete building for indoor radio communications. IEEE Transactions on Vehicular Technology. 1986, Vol. 35, No. 4, pp. 146–152.

(6) Chiba, H., Miyazaki, Y. Reflection and Transmission Characteristics of Radio Wave at

Reinforced Concrete Slabs for Mobile Communication Frequency Band. ITE Technical Report. 1996, Vol. 20, No. 72, pp. 89–96.

(7) Young, W. F., Holloway, C. L., Koepke, G., Camell, D., Becquet, Y., Remley, K. A. Radio-Wave Propagation Into Large Building Structures—Part 1: CW Signal Attenuation and Variability. IEEE Transactions on Antennas and Propagation. 2010, Vol. 58, No. 4, pp. 1279–1289.

(8) Shiihara, K., Matsunaga, T., Matsunaga, M. Radio Disturbance Being Occurred by Adjacent Concrete Buildings. ITE Technical Report. 2011, Vol. 35.3, pp. 53–56.

(9) Rodriguez, I., Nguyen, H. C., Jorgensen, N. T. K., Sorensen, T. B., Mogensen. P. Radio Propagation into Modern Buildings: Attenuation Measurements in the Range from 800 MHz to 18 GHz. 2014 IEEE 80th Vehicular Technology Conference (VTC2014-Fall). 2014, pp. 1–5.

(10) Agnieszka, C., Tomasz, S., Dariusz, K. The Influence of Building Materials and Electrical Parameter Variability on Electromagnetic Wave Propagation. Energies. 2024, Vol. 17, No. 23.

(11) 一宮一夫. 低炭素で高機能バインダーとしてのジオポリマー：セメント産業への期待. セメント・コンクリート. 2021, No. 890, pp. 18–23.

(12) 土木学会. コンクリート技術シリーズ No.132 土木分野におけるジオポリマー技術の実用化推進のための研究小委員会（361 委員会）成果報告書. 2022.

(13) Tanaka, S., Yamada, M. Non-Destructive Inspection of Concrete Structures Using an Electromagnetic Wave (Radar) Based on a Signal Propagation Model. Transactions of the Society of Instrument and Control Engineers. 2003, Vol. 39, No. 5, pp. 432–440.

(14) Haddad, R. H., Al-Qadi, I. L. Characterization of portland cement concrete using electromagnetic waves over the microwave frequencies. Cement and Concrete Research. 1998, Vol. 28, No. 10, pp. 1379–1391.

(15) 青山博之. 原子力関連施設とコンクリート―概要―. コンクリート工学. 1989, Vol. 27, No. 4, pp. 6-11.

(16) 秋野金次, 山下利夫. 原子力関連施設とコンクリート―原子炉建屋―. コンクリート工学. 1989, Vol. 27, No. 4, pp. 12-20.

(17) 加藤宗明. 原子力関連施設とコンクリート―格納容器(PCCV)―. コンクリート工学. 1989, Vol. 27, No. 4, pp. 21-28.

(18) 加藤欽也. 原子力関連施設とコンクリート―格納容器(RCCV)―. コンクリート工学. 1989, Vol. 27, No. 4, pp. 29-34.

(19) 岡村甫, 青柳征夫, 片平冬樹. 原子力関連施設とコンクリート―土木構造物―. コンクリート工学. 1989, Vol. 27, No. 4, pp. 35-40.

(20) Tanoi, L., Kawase, T. A Study on Electromagnetic Shielding Characteristics of Reinforced Concrete Wall - A Study on Electromagnetic Shielding Method of specific frequency -. 東急建設技術研究所報. 2011, No. 37, pp. 61-64.

(21) Tanoi, L., Kawase, T. A Study on Electromagnetic Shielding Characteristics of Reinforced

Concrete Wall with Wire Mesh. 東急建設技術研究所報. 2012, No. 38, pp. 43‑46.

(22) Takahashi, M., Nakagawa, Y., Abe, M., Kikuchi, A. Reflection and Transmission Characteristics of Electromagnetic wave for Concrete wall. The Institute of Image Information and Television Engineers Technical Report. 1997, Vol. 21.60, pp. 25‑30.

(23) Fu, X., Chung, D. D. L. Radio-wave-reflecting concrete for lateral guidance in automatic highways. Cement and Concrete Research. 1998, Vol. 28, No. 6, pp. 795–801.

(24) Sato, H., Domae, H., Takahashi, M., Abe, M. Reflection and Transmission Control of Electromagnetic wave for Concrete Walls. The IEICE Transactions on Communications. 1999, Vol. 82, No. 4, pp. 674-682.

(25) Yang, M., Stavrou, S., Brown, A.K. Hybrid ray-tracing model for radio wave propagation through periodic building structures. IET Microwaves, Antennas & Propagation. 2011, Vol. 5, No. 3, pp. 340–348.

(26) Suzuki, Y., Omiya, M. Computer simulations for a site-specific modeling of indoor radio wave propagation. 2016 IEEE Region 10 Conference (TENCON). 2016, pp. 123–126.

(27) Sarkar, T. K., Abdallah, M. N., Salazar-Palma, M. Survey of Available Experimental Data of Radio Wave Propagation for Wireless Transmission. IEEE Transactions on Antennas and Propagation. 2018, Vol. 66, No. 12, pp. 6665–6672.

(28) Haneda, K., Rudd, R., Vitucci, E., He, D., Kyösti, P., Tufvesson, F., Salous, S., Miao, Y., Joseph, W., Tanghe, E. Chapter 2 - Radio propagation modeling methods and tools. Inclusive Radio Communications for 5G and Beyond. Academic Press, 2021, pp. 7‑48, ISBN978-0-12-820581-5. https://www.sciencedirect.com/science/article/pii/B9780128205815000080.

(29) Sammut, S., Gatt, E., Borg, R. P. Wireless Data Transmission through Concrete Structures. Journal of Sustainable Architecture and Civil Engineering. 2024, Vol. 36, No. 3, pp. 161–179.

CHAPTER 2. RADIO WAVE TRANSPARENCY IMPROVEMENT

This chapter presents the results of an investigation into methods for improving radio wave transparency in unreinforced concrete members.

2.1. Literature review

In this section, based on the theory of electromagnetic wave propagation in concrete and a review of previous studies, the impact of moisture in concrete on radio wave transparency is discussed. Additionally, the forms of moisture in concrete and their classifications are organized, and the focal points of this study are outlined.

2.1.1. Radio wave propagation in lossy media

Radio waves used for wireless communications, including 5G, are a type of electromagnetic wave. Electromagnetic waves propagate without loss in a vacuum; however, when passing through a medium with attenuation properties, they propagate with energy losses. Considering first the propagation of electromagnetic waves in free space without obstacles, the transmission gain G in free space can be expressed as the ratio of received power P_{r} to transmitted power P_{t}, as shown in Equation (2-1)[(1)].

$$G = \frac{P_{\mathrm{r}}}{P_{\mathrm{t}}} = \left(\frac{\lambda}{4\pi d}\right)^2 G_{\mathrm{t}} G_{\mathrm{r}} \qquad (2-1)$$

Let d denote the distance between the transmitting and receiving antennas, G_{t} and G_{r} represent the power gains of the transmitting and receiving antennas, respectively, and λ denote the wavelength. Specifically, when $G_{\mathrm{t}} = G_{\mathrm{r}} = 1$, the gain G is referred to as the free-space propagation gain G_{f}, which is expressed by Equation (2-2).

$$G_{\mathrm{f}} = \left(\frac{\lambda}{4\pi d}\right)^2 \qquad (2-2)$$

Typically, this gain is represented in terms of loss, and the free-space propagation loss is expressed by Equation (2-3)[(2)].

$$L_{\mathrm{f}} = \frac{1}{G_{\mathrm{f}}} \qquad (2-3)$$

From Equations (2-2) and (2-3), it is evident that free-space propagation loss is proportional to the

square of the distance and inversely proportional to the square of the wavelength, or equivalently, proportional to the square of the frequency. However, this relationship applies only to free space without obstacles. In urban environments with obstacles such as buildings, empirical rules based on experiments indicate that propagation loss is proportional to the cube or fourth power of the distance[3].

Concrete, a material widely used in construction, is a lossy medium composed of dielectric, resistive, and conductive components, including cement hydrates, aggregates, and water, randomly mixed together. A lossy medium is a material that dissipates the energy of electromagnetic waves, primarily as heat, causing the wave intensity to decay exponentially as it propagates. There are three types of lossy media: conductive loss media, dielectric loss media, and magnetic loss media. The constants that determine the loss for each type are electrical conductivity κ, permittivity ϵ, and permeability μ, respectively. In a uniform dielectric medium, both the permittivity and permeability are represented as complex numbers, referred to as the complex permittivity $\dot{\epsilon}$ and the complex permeability $\dot{\mu}$. The ratios of these values to the permittivity ϵ_0 and permeability μ_0 in a vacuum are also complex numbers, called the complex relative permittivity $\dot{\varepsilon}_r$ and the complex relative permeability $\dot{\mu}_r$, expressed by Equations (2-4) and (2-5)[4].

$$\dot{\epsilon}_r = \epsilon_r' - j\epsilon_r'' \qquad (2-4)$$

$$\dot{\mu}_r = \mu_r' - j\mu_r'' \qquad (2-5)$$

It is known that for both conductive and dielectric loss media, $\mu_r' = 1$, $\mu_r'' = 0$[4].

For conductive loss media that carry only conduction current even at high frequencies, the imaginary part of the complex relative permittivity ϵ_r'' for electromagnetic waves with angular frequency ω can be expressed in terms of the conductivity κ using Equation (2-6)[4].

$$\epsilon_r'' = \frac{\kappa}{\omega\epsilon_0} \qquad (2-6)$$

In contrast, for composite media such as concrete, Equation (2-6) cannot be applied. This is because, in an electrical circuit model, composite media consist of resistive and conductive components dispersed within a dielectric, leading to highly complex equivalent circuits. Such complexity makes it impossible to represent the medium using a single element.

2.1.2. Attenuation equations and fluctuation factors of radio wave

When an electromagnetic wave oscillates sinusoidally at a single angular frequency ω, assuming it satisfies a one-dimensional wave equation, Equations (2-7) and (2-8) can be derived using the vector wave equation[5].

$$\nabla^2 E + k^2 E = 0 \tag{2-7}$$

$$\nabla^2 H + k^2 H = 0 \tag{2-8}$$

Here, E represents the electric field $(\mathrm{V/m})$, H represents the magnetic field $(\mathrm{A/m})$, and k is referred to as the propagation constant. The propagation constant $k\,(1/\mathrm{m})$ for an electromagnetic wave with angular frequency ω is expressed by Equation (2-9) in terms of the permittivity $\epsilon\,(\mathrm{F/m})$, permeability $\mu\,(\mathrm{H/m})$, and conductivity $\kappa\,(\mathrm{S/m})$.

$$k^2 = \omega^2 \epsilon\mu - j\omega\mu\kappa \tag{2-9}$$

When the propagation constant k is a complex number, it can generally be separated into its real and imaginary parts, as shown in Equation (2-10). The parameters α and β are defined by Equations (2-11) and (2-12), respectively.

$$k = \sqrt{\omega^2 \epsilon\mu - j\omega\mu\kappa} = \beta - j\alpha \;(\alpha > 0, \beta > 0) \tag{2-10}$$

$$\alpha = \omega\sqrt{\frac{\epsilon\mu}{2}}\left\{\sqrt{1 + \frac{\kappa^2}{\omega^2\epsilon^2}} - 1\right\}^{1/2} \tag{2-11}$$

$$\beta = \omega\sqrt{\frac{\epsilon\mu}{2}}\left\{\sqrt{1 + \frac{\kappa^2}{\omega^2\epsilon^2}} + 1\right\}^{1/2} \tag{2-12}$$

The real part $\beta\,(\mathrm{rad/m})$ of the propagation constant k, referred to as the phase constant, indicates the phase change accompanying electromagnetic wave propagation. On the other hand, the imaginary part $\alpha\,(\mathrm{dB/m})$, known as the attenuation constant, represents the magnitude of attenuation during electromagnetic wave propagation[5]. When a plane wave polarized in the x-direction propagates in the z-direction, it can be expressed using the terms α and β, resulting in Equation (2-13).

$$E = \hat{x}E_0 \exp(-jkz) = \hat{x}E_0 \exp(-\alpha z - j\beta z) \tag{2-13}$$

Consequently, the magnitude of the electric field $|E|$ is described by the attenuation equation shown in Equation (2-14), indicating that the electric field diminishes as the wave travels in the z-direction.

$$|E| = |E_0| \exp(-\alpha z) \quad (2-14)$$

Therefore, the degree of attenuation of the electromagnetic wave is determined by the attenuation constant α and the propagation distance z. The greater the attenuation constant α or the propagation distance z, the larger the attenuation. For concrete members, the attenuation constant α is an intrinsic property of the material, while the propagation distance z corresponds to the thickness of the member. Thus, to improve the radio wave transparency of concrete members, it is effective to reduce the attenuation constant α of the material itself and minimize the member thickness.

Conductive loss media and dielectric loss media are classified based on the ratio of conduction current to displacement current, expressed as $\kappa/\omega\epsilon$. The attenuation constant and phase constant for these media are represented by Equations (2-15) and (2-16), respectively[5].

$\kappa/\omega\epsilon \gg 1$ (Conduction loss medium)

$$\alpha \cong \sqrt{\frac{\omega\kappa\mu}{2}}, \beta \cong \sqrt{\frac{\omega\kappa\mu}{2}} \quad (2-15)$$

$\kappa/\omega\epsilon \ll 1$ (Dielectric loss medium)

$$\alpha \cong \left(\frac{\kappa}{2}\right)\sqrt{\frac{\mu}{\epsilon}}, \beta \cong \omega\sqrt{\mu\epsilon} \quad (2-16)$$

Since concrete is a composite medium, applying either Equation (2-15) or Equation (2-16) exclusively is considered challenging. However, because concrete is a nonmagnetic material with $\mu_r = 1$ under normal conditions, the electromagnetic wave attenuation characteristics, or radio wave attenuation characteristics, of concrete are determined by its conductivity κ and relative permittivity ϵ_r. Regardless of the medium, since the conductivity κ appears in the numerator of the attenuation constant α, it follows that a lower conductivity κ results in a smaller attenuation constant α and consequently less electromagnetic wave attenuation.

2.1.3. Effect of moisture on radio wave transparency

As discussed in Sub-section 2.1.2, the radio wave transparency of concrete, particularly the attenuation constant, is closely related to its electrical properties, especially its conductivity and permittivity. Research on the electrical properties of concrete has been conducted for various purposes, including improving electromagnetic shielding performance and advancing non-destructive testing methods.

Chino et al.[6] investigated changes in the complex permittivity of lightweight concrete combined with ferrite electromagnetic wave absorbers during water absorption (**Figure 2-1**). In this study, the water absorption rate X was defined as $X = 0$ (0% absorption rate) when the sample was dried at

105°C for 24 hours, and $X = 1.0$ (100% absorption rate) when the sample was submerged in water at 20°C for 24 hours. The water absorption rate X was calculated using Equation (2-17) based on the weight of the sample during absorption. Additionally, the real part ϵ_r' and the imaginary part ϵ_r'' of the complex permittivity $\epsilon_r = \epsilon_r' - j\epsilon_r''$ at X were determined using Equations (2-18) and (2-19), respectively.

$$X = \frac{(\text{Sample weight}) - (\text{Sample weight at } 0\%)}{(\text{Sample weight at } 100\%) - (\text{Sample weight at } 0\%)} \quad (2-17)$$

$$\epsilon_r' = \epsilon_r' \text{ at } 0\% + X(\epsilon_r' \text{ at } 100\% - \epsilon_r' \text{ at } 0\%) \quad (2-18)$$

$$\epsilon_r'' = \epsilon_r'' \text{ at } 0\% + X(\epsilon_r'' \text{ at } 100\% - \epsilon_r'' \text{ at } 0\%) \quad (2-19)$$

From **Figure 2-1**, it can be seen that both the real and imaginary parts of the complex permittivity increase with the water absorption rate. When comparing the absorption rates of 0% and 36.8%, the imaginary part increases approximately fivefold, whereas the real part increases 10 to 60 times, indicating that the real part changes more significantly. Furthermore, while the imaginary part remains unaffected by frequency, the real part decreases with increasing frequency for any absorption rate other than 0%.

Hayashi et al.[7] investigated the effect of moisture content on the complex relative permittivity of mortar specimens with added carbon powder, aimed at developing electromagnetic wave absorbers using mortar. Their findings revealed that both the real and imaginary parts of the complex relative permittivity were lower in air-dried specimens compared to wet specimens, and even lower in oven-dried specimens.

Noda et al.[8] examined the electrical properties of concrete under alternating current and their influencing factors to explore the potential of evaluating concrete quality using relative permittivity. They clarified the relationships between relative permittivity and relative moisture content and between relative permittivity and the cement-to-water ratio (C/W) (**Figure 2-2**, **Figure 2-3**). The results shown in **Figure 2-2** were obtained for concrete with water-to-cement ratio (W/C) of 55% and a curing age of approximately four months under an alternating current frequency of 1 mHz. **Figure 2-3** presents results for concrete with a curing age of 28 days. The relative moisture content was calculated using Equation (2-20), with W_i, W_0, and W_d representing the mass of the specimen at the time of measurement, the saturated mass, and the oven-dry mass, respectively.

$$\text{Relative moisture content}(\%) = \left(\frac{W_i - W_d}{W_0 - W_d}\right) \times 100 \quad (2-20)$$

From **Figure 2-2**, the relative permittivity increases with increasing relative moisture content,

with particularly large changes observed below 50% relative moisture content. From **Figure 2-3**, the relative permittivity decreases as C/W increases, and the impact of C/W becomes more pronounced at lower frequencies. Noda et al. inferred that higher C/W results in a denser structure, reducing the water content in concrete and increasing its resistance. Consequently, dielectric phenomena are less likely to occur, and charge generation is suppressed, leading to lower relative permittivity.

Guihard et al.[9] proposed an electromagnetic model for estimating the moisture content of concrete based on its permittivity. To validate the model, they clarified the relationship between permittivity and moisture content for concrete with varying W/C. Their results confirmed that permittivity increases with moisture content and that the effect of moisture content on permittivity is more pronounced for concrete with higher W/C.

Dinh et al.[10] investigated the dielectric properties of concrete for electromagnetic wave propagation in the GHz range, specifically from 1 GHz to 10 GHz. Their study demonstrated that the dielectric properties of concrete are strongly dependent on moisture content, pore volume, and pore size distribution, with higher moisture content leading to increased dielectric constant and dielectric loss. Additionally, they revealed that over time, moisture evaporates and is consumed by hydration reactions, resulting in a decrease in the dielectric constant and dielectric loss, thereby reducing the attenuation of electromagnetic waves.

Ikuta et al.[11] investigated the impact of various factors on the resistivity of concrete. They clarified the relationship between the resistivity of concrete with a W/C of 70% under direct current and its mass moisture content (**Figure 2-4**). From **Figure 2-4**, it was observed that resistivity decreases linearly with increasing moisture content between 5.5% and 7.5%, becomes nearly constant above 7.5%, and exhibits significant variation at moisture contents below 5.5%. Similar trends were reported by Makita[12], who demonstrated that as moisture content decreases, i.e., as drying progresses, resistivity or resistivity values increase substantially, and the conductivity, which is the reciprocal of resistivity, decreases significantly. Ikuta et al. hypothesized that the influence of water on resistivity is dominant between 5.5% and 7.5% moisture content. Beyond 7.5%, the pores within concrete are sufficiently filled with water, making water quantity less influential on resistivity. Conversely, below 5.5%, the continuity of water within the pores becomes more critical than the amount of water itself[11].

Soutsos et al.[13] investigated the electrical properties of concrete to improve the accuracy of non-destructive testing of concrete structures using radar. They clarified the relationship between relative permittivity, conductivity, and moisture content in concrete (**Figure 2-5**). Moisture content was calculated using Equation (2-21) based on the specimen's weight immediately after measurement, its weight after oven drying, and its volume. These results were obtained at a frequency of 500 MHz.

$$\text{Moisture content}[\%] = \frac{\begin{pmatrix}\text{Specimen weight immediately after measurement} \\ -\text{Specimen weight after oven drying}\end{pmatrix}}{\text{Specimen volume}} \times 100 \quad (2-21)$$

From **Figure 2-5**, both relative permittivity and conductivity increase with increasing moisture content. Particularly, conductivity changes by 30 to 60 times between moisture content levels of approximately 0% and 17%. When moisture content is extremely low, conductivity is significantly lower compared to high moisture content, consistent with the findings of Ikuta et al.[11] and Makita[12].

Thus, the moisture state within concrete significantly affects its electrical properties, such as relative permittivity and conductivity, which are critical factors determining its radio wave transparency. Furthermore, lower moisture content in concrete tends to result in lower relative permittivity and conductivity. Based on Equation (2-15), lower moisture content leads to a smaller attenuation constant α, resulting in reduced electromagnetic wave attenuation. According to Soutsos et al.[13], as conductivity changes significantly with moisture content, the ratio $\kappa/\sqrt{\epsilon_r}$ decreases with lower moisture content. Therefore, based on Equation (2-16), lower moisture content also leads to a smaller attenuation constant α, reducing electromagnetic wave attenuation. Consequently, reducing the moisture content within concrete is an effective approach to improving its radio wave transparency.

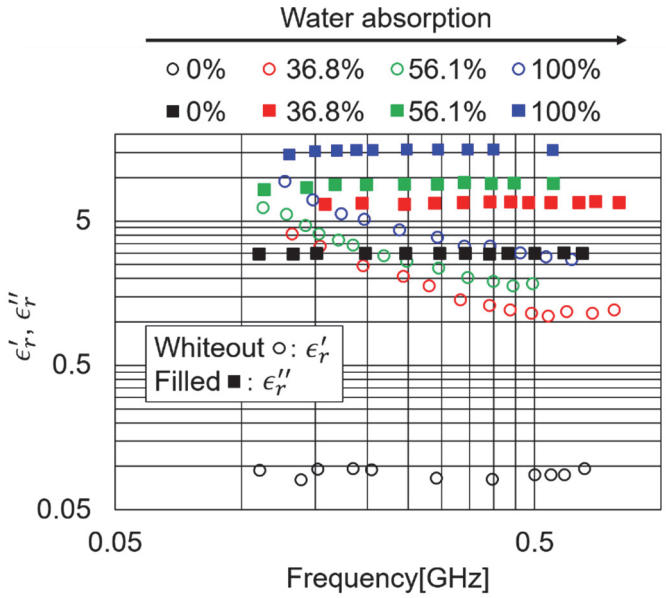

Figure 2-1 Variation of dielectric properties of lightweight concrete as a function of water absorption[6]

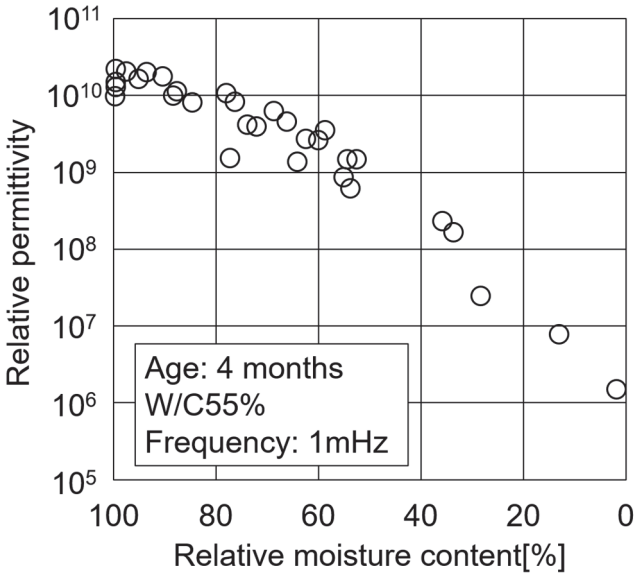

Figure 2-2 Relation between relative permittivity and relative moisture content[8]

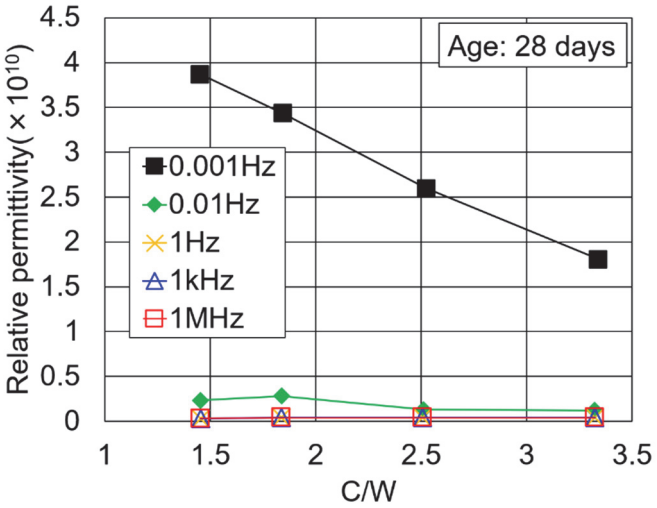

Figure 2-3 Relation between relative permittivity and C/W[8]

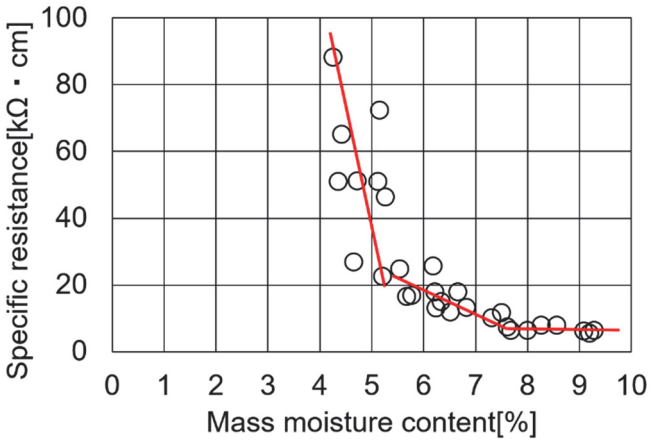

Figure 2-4 Relation between specific resistance and mass moisture content[11]

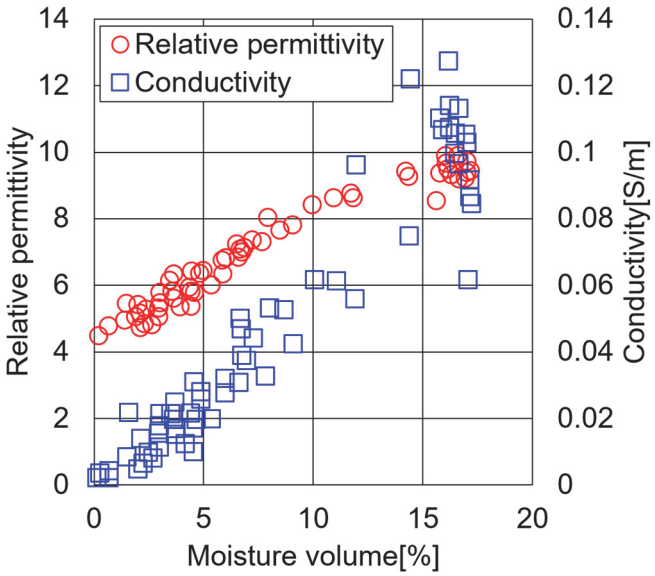

Figure 2-5 Relation between relative permittivity, conductivity and moisture volume[13]

2.1.4. Moisture in concrete

Within concrete, particularly within hardened cement paste, a wide range of pores exists, spanning from a few nanometers to several millimeters in size. These pores consist of air bubbles introduced during mixing and water pores left by the spaces previously occupied by water. Generally, water pores account for the majority of total porosity[14]. **Table 2-1** presents a classification of pores in hardened cement paste[15]. Air bubbles introduced during mixing are classified into entrapped air and entrained air. Entrapped air consists of unintended large bubbles with diameters exceeding 1 mm, which negatively affect the strength and durability of concrete. Conversely, entrained air refers to intentionally induced bubbles of 50-200 μm in size, achieved using air-entraining agents (AE agents),

which are essential for freeze-thaw resistance and workability. Water pores are further categorized into capillary pores, gel pores, and interlayer pores. Capillary pores represent the spaces left by water in fresh cement paste and interfacial zones between cement paste and aggregates. Their size ranges from 3 nm to 30 μm, making them critical for the durability of concrete. Gel pores, on the other hand, are extremely small pores (1-3 nm) left unfilled within the hydrated cement paste's gel (mainly C-S-H gel) during hydration. Interlayer pores, measuring a few Å, exist within the layers of calcium silicate hydrate. While gel pores and interlayer pores generally do not adversely affect strength and durability, they may influence shrinkage and creep behaviors[16]. The moisture within these pores can be categorized based on its location: water within entrapped or entrained air pores is “interstitial water,” water within capillary pores is “capillary water,” condensed liquid water or physically adsorbed water on the surfaces of gel pores is “gel water” (○ in **Figure 2-6**), and water in intracrystallite pores is “intracrystallite water” (× in **Figure 2-6**).

The moisture within these pores exists due to physical or chemical adsorption or capillary condensation, and its amount and characteristics vary with factors such as mix proportion, curing conditions, temperature, and humidity. Separately from this pore-based moisture, cement hydration products, such as C-S-H gel, calcium hydroxide, ettringite, and monosulfate, also retain chemically bound water. Powers et al.[17, 18] classified water in hardened cement paste, as illustrated in **Figure 2-7**. They defined the moisture in pores (gel water and capillary water) as "evaporable water" and the chemically bound water as "non-evaporable water." The total volume of evaporable water was equated to the volume of pores in the hardened cement paste. Moreover, evaporable water was defined as the water that evaporates under conditions such as D-dry (drying at the equilibrium vapor pressure of ice at -79°C) or oven drying at 105±5°C. Non-evaporable water was defined as the weight loss upon ignition of the specimen at approximately 1000°C after D-dry or oven drying. In summary, water that easily evaporates upon drying is classified as evaporable water, whereas water that remains despite drying is classified as non-evaporable water.

As noted in Sub-section 2.1.3, previous research indicates that reducing the moisture content in concrete is effective for improving its electromagnetic wave transparency. However, existing studies primarily focus on the effects of evaporable water, with little attention paid to the influence of non-evaporable water. This study addresses the effects of both evaporable and non-evaporable water on electromagnetic wave transparency. To eliminate the influence of aggregate properties and the water content within aggregates, the scope of the study was limited to the hardened cement paste within concrete.

Following the classification proposed by Powers et al., this study categorized water in hardened cement paste into evaporable and non-evaporable water and investigated the effects of these water types on electromagnetic wave transparency, as well as the improvement in transparency achieved by reducing them. The detailed classification is presented in **Figure 2-8**. While Powers et al. did not

include water in air voids or intracrystallite water in their classification, this study incorporated these into the category of evaporable water. Consequently, evaporable water was considered present in all voids within the hardened cement paste, correlating with total porosity. Although it is challenging to clearly differentiate between evaporable and non-evaporable water or to precisely quantify their respective amounts due to the inclusion of unstable non-evaporable water, this classification was deemed sufficient for the relative evaluation of their effects on electromagnetic wave transparency and the enhancement of transparency through their reduction.

Table 2-1 Classification of pores in hardened cement paste[15]

Broad category	Type	Pore diameter	Location
Air bubble	Entrapped air	1mm～	Between aggregates
	Entrained air	10～100μm	In cement paste
Pores occupied by water	Capillary pore	3nm～30μm	In cement paste and between cement paste and aggregate
	Gel pore	1～3nm	Between gels
	Intracrystallite pore	～1.2nm	In gels

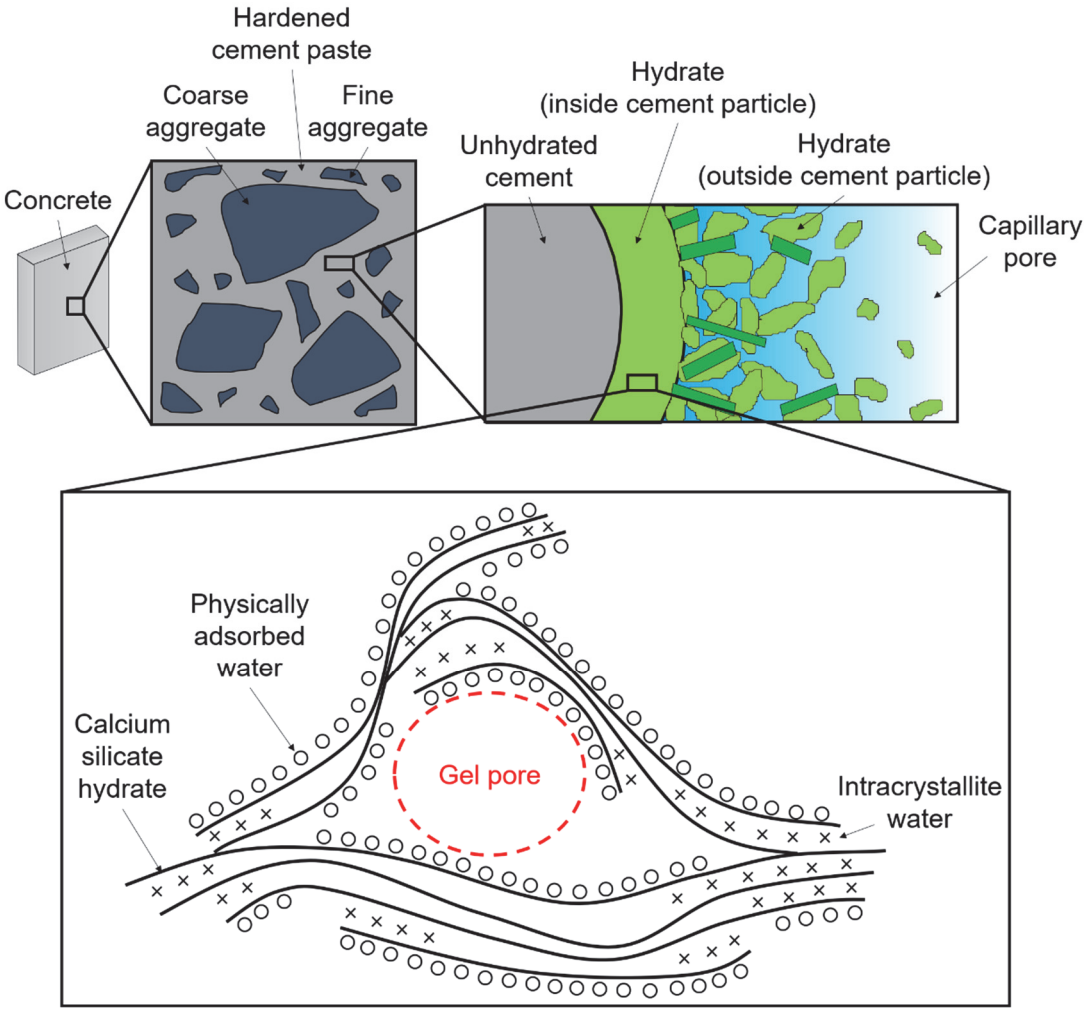

Figure 2-6 Schematic diagram of the structure around gel pore

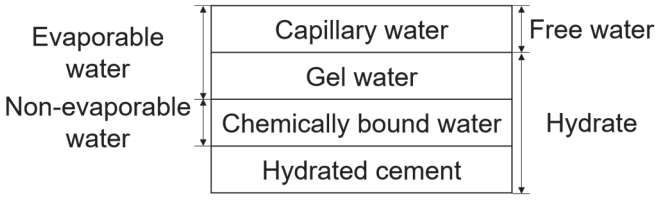

Figure 2-7 Classification of water in hardened cement paste by Powers et al.[17, 18]

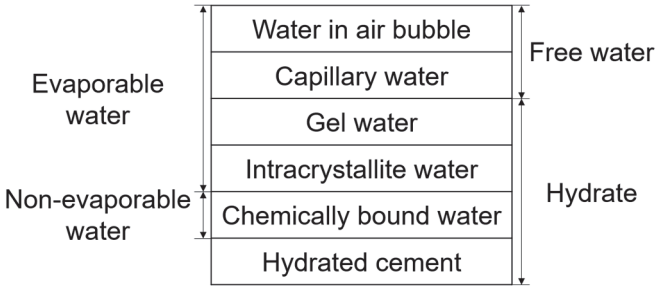

Figure 2-8 Classification of water in hardened cement paste in this study

2.1.5. Member thickness

As discussed in Sub-section 2.1.2, improving the radio wave transparency of concrete members requires not only reducing the attenuation constant of the material itself but also decreasing the thickness of the member. This section focuses on concrete wall members, particularly shear walls, which serve as the wall panels of seismic walls, and outlines methods for calculating wall thickness and the factors influencing it.

The thickness of concrete shear walls is specified to be at least 120 mm according to building regulations, and in the case of reinforced concrete structures, it must also be no less than one-thirtieth of the clear height of the wall panel[19]. For reinforced concrete walls, additional detailed regulations are provided, as shown in **Table 2-2** and **Table 2-3**[20].

The aforementioned specifications serve as prescriptive regulations; the actual wall thickness is determined through structural calculations. Below, the method for calculating wall thickness based on allowable shear force using the allowable stress design method is presented. For simplicity, a wall panel without openings or columns is assumed.

The long-term allowable shear force Q_{AL}, used to evaluate the usability of wall members, can be calculated using Equation (2-22).

$$Q_{AL} = tlf_s \qquad (2-22)$$

where:

t: Thickness of the wall panel

l: Total height of the wall member, including columns or beams

f_s: Allowable shear stress of the concrete

From this, the wall thickness can be determined using Equation (2-23). For wall panels with the same height and long-term allowable shear force, the thickness is determined by the allowable shear stress of the concrete.

$$t = \frac{Q_{AL}}{lf_s} \quad (2-23)$$

The short-term allowable shear force Q_A, used to evaluate damage prevention, can be calculated using Equation (2-23), which considers the larger value between Q_1 and Q_2 from Equations (2-24) and (2-25).

$$Q_A = \max(Q_1, Q_2) \quad (2-24)$$

$$Q_1 = tlf_s \quad (2-25)$$

$$Q_2 = \sum Q_w + \sum Q_c \quad (2-26)$$

where:

Q_w: Allowable shear force of a single wall panel

Q_c: Allowable shear force of a single column or beam

Q_w and Q_c can be calculated using Equations (2-26) and (2-27), respectively.

$$Q_w = p_s t l_e f_t \quad (2-27)$$

$$Q_c = bj\{\alpha f_s + 0.5_w f_t(p_w - 0.002)\} \quad (2-28)$$

where:

l_e: Effective length of the wall panel

$l_e = l'$ when columns are present on both sides

$l_e = 0.9l'$ when a column is present on one side

$l_e = 0.8l'$ when no columns are present

l': Clear length of the wall panel

b: Width of the column or beam

j: Distance between the centroids of stress in the column or beam ($= (7/8)d$ or $0.8D$)

D: Total height of the column or beam

d: Effective height of the column or beam

f_t: Short-term allowable tensile stress of shear reinforcement in the wall panel (limited to 390 N/mm² if it exceeds this value)

${}_w f_t$: Short-term allowable tensile stress of stirrup reinforcement in columns or beams (limited to 390 N/mm² if it exceeds this value)

p_s: The shear reinforcement ratio for wall panels defined by Equation (2-29)

$$p_s = \frac{a_w}{ts} \qquad (2-29)$$

where:

a_w : Cross-sectional area of one set of shear reinforcements in the wall panel

s : Spacing of shear reinforcements

Additional conditions for calculating p_s:

1. For wall panels with columns on both sides and $p_s \geq 0.012$, $p_s = 0.012$
2. For other wall panels with $p_s \geq 0.006$, $p_s = 0.006$
3. When $p_s \geq p_w b/t$, $p_s = p_w b/t$
4. For wall panels with different horizontal and vertical reinforcement ratios, the horizontal reinforcement ratio is used for p_s, with an upper limit of twice the vertical reinforcement ratio
5. For floors, p_s is the ratio of slab reinforcement effectively anchored to beams relative to slab thickness

p_w : Column stirrup ratio (limited to a maximum value of 0.012)

α : Confinement coefficient

$\alpha = 1.5$ for walls with columns on both sides

$\alpha = 1.0$ for pilasters, spandrel beams, and floors

For a single unreinforced wall panel without columns, $Q_2 = 0$, and therefore, Q_A can be expressed by Equation (2-30).

$$Q_A = \max(Q_1, 0) = Q_1 = tlf_s \qquad (2-30)$$

Consequently, even for wall panels with the same height and long-term allowable shear force, the thickness of the wall panel is determined by the allowable shear stress of the concrete, as in the case of the short-term allowable shear force.

Table 2-2 Minimum thickness of cast-in-place reinforced concrete load bearing walls[20]

Floor			Minimum wall thickness t_0 (mm)	Remarks
Ground floor	1-story building (excluding basement)		120 and $h_s/25$	h_s: Distance between vertical supports which are major in terms of structural capacity
	Each floor of a 2-story building (excluding basement)		150 and $h_s/22$	
	Buildings of 3 to 5 stories (excluding basement)	Top floor	150 and $h_s/22$	
		Other floors	180 and $h_s/22$	
Basement			180 and $h_s/18$	

Table 2-3 Minimum thickness of precast reinforced concrete load bearing walls[20]

Floor		Minimum wall thickness t_0 (mm)	Remarks
Ground floor	Top floor and the second floor counting from the top floor	120 and $h_s/25$	h_s: Distance between vertical supports which are major in terms of structural capacity
	Other floors	150 and $h_s/22$	
Basement		180 and $h_s/18$	

2.2. Study flow

As described in Section 2.1, improving the radio wave transparency of concrete members can be effectively achieved by reducing both evaporative and non-evaporative moisture content to lower the material's attenuation coefficient and by increasing the strength of concrete to reduce the member thickness.

In this study, first, as a method for reducing evaporative moisture, a drying treatment was applied to the concrete members to forcibly dissipate evaporative moisture to the external environment, and its effect on improving radio wave transparency was examined. Next, as a method for enhancing strength, the water-to-powder ratio (W/P) was set to an extremely low level to reduce the pore volume, and its impact on radio wave transparency improvement was investigated. Notably, high-strength concrete is expected to suppress drying-induced cracking and further reduce the amount of evaporative moisture through pore volume reduction. Finally, as a method for reducing non-evaporative moisture, geopolymer (GP) was applied, and the effect of high-strength, low-W/P GP on enhancing radio wave transparency was evaluated. Detailed examinations of each condition will be discussed in the following sections.

2.3. Radio wave transparency evaluation method

In this study, the primary evaluation criterion is the radio wave transparency of a structural member that exhibits the same mechanical performance. The calculation method and the measurement methods for the parameters required for this calculation are described below.

2.3.1. Radio wave transparency as a member

Radio wave transparency in this study is expressed in terms of transmission loss. First, transmission loss is defined by Equation (2-31). Throughout this paper, transmission loss is expressed in decibels (dB).

$$L = 10\log_{10}\left(\frac{|E_0|}{|E|}\right) \tag{2-31}$$

Where:

L: Transmission loss (dB)

$|E_0|$: Magnitude of the electric field of the radio wave before passing through the medium

$|E|$: Magnitude of the electric field of the radio wave after passing through the medium

The primary evaluation index in this study is the transmission loss of a structural member when a wall panel is fabricated to exhibit the same allowable shear strength under each condition. This can be calculated using Equation (2-32), which is derived from Equations (2-14) and (2-31).

$$L_c = 10\log_{10}[\exp(\alpha z_c)] \tag{2-32}$$

Where:

L_c: Transmission loss of a structural member when a wall panel is fabricated to exhibit the same allowable shear strength (dB)

α: Attenuation coefficient of the material, calculated using Equation (2-33)

$$\alpha = \frac{1}{z_s}\ln\left(10^{\frac{L_s}{10}}\right) \tag{2-33}$$

Where:

z_s: Thickness of the test specimen (mm), set as $z_s = 24\text{mm}$ in this study

L_s: Transmission loss of the test specimen (dB), with the measurement method described in Sub-section 2.3.2

z_c: Thickness of the structural member when a wall panel is fabricated to exhibit the same allowable shear strength (mm)

The thickness z_c of the wall panel fabricated to exhibit the same allowable shear strength under each condition was calculated based on the compressive strength for each condition using Equations (2-22) to (2-30). To exclude the effects of reinforcement, calculations were conducted assuming non-reinforced conditions, and the wall height $l(=l')$ was set uniformly to 1000 mm for all cases. The allowable shear stress of concrete was calculated using Equations (2-34) and (2-35)[19].

$$f_{s,\mathrm{long}} = \min\left(\frac{1}{30}F_c, 0.49 + \frac{1}{100}F_c\right) \quad (2-34)$$

$$f_{s,\mathrm{short}} = 1.5 f_{s,\mathrm{long}} \quad (2-35)$$

where:

$f_{s,\mathrm{long}}$: Long-term allowable shear stress of concrete (N/mm^2)

F_c: Design compressive strength of concrete (N/mm^2), defined here as the measured compressive strength

$f_{s,\mathrm{short}}$: Short-term allowable shear stress of concrete (N/mm^2)

Additionally, in compliance with the specifications, the minimum wall thickness was set at 120 mm. If the required wall thickness to satisfy long-term allowable shear forces differed from that for short-term allowable shear forces, the larger value was adopted.

2.3.2. Radio wave transparency measurement method

A 24 mm thick plate-shaped specimen was fabricated, and its transmission loss was measured using the free-space method with a vector network analyzer. To ensure the fabrication of specimens with as uniform a thickness as possible, the specimen thickness was set to match the dimensions of standard lumber. The measurement system's setup is shown in Figure 2-9, and the measurement parameters are listed in **Table 2-4**. During the measurement, dielectric lens antennas were connected to the transmitting and receiving ports, and the antennas were precisely aligned using a dedicated jig. The impulse response between the transmitting and receiving ports was recorded, and the power P of the peak transmitted radio waves was measured. The transmission loss L_s was defined according to Equation (2-36) as the difference between the received power P_{ref} in the absence of the specimen and the measured transmitted power. Transmission loss is expressed in decibels (dB) in this study.

$$L_s = 10\log_{10}\left(\frac{P_{\mathrm{ref}}}{P}\right) \qquad (2-36)$$

For instance, a transmission loss of 10 dB indicates that the radio wave intensity after passing through the specimen is reduced to one-tenth of the intensity before transmission. A smaller transmission loss value corresponds to higher radio wave transparency of the specimen.

To measure the transmitted wave power P, the specimens were wrapped in plastic film to prevent moisture absorption or drying, which could alter the internal moisture content during the measurement. Measurements were performed five times at different positions on the specimens, and the average value was used as the representative result. It was confirmed beforehand that the plastic wrapping did not affect the measurement results.

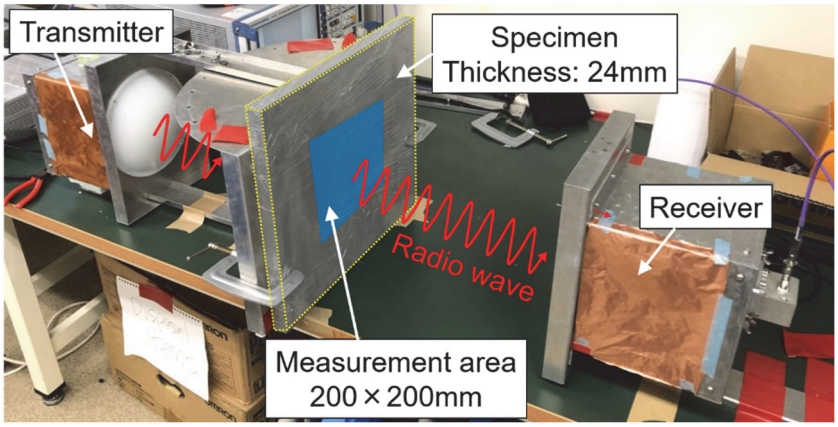

Figure 2-9 Radio wave transmission testing system

Table 2-4 Measurement parameter

Central frequency	33 GHz
Signal band	6 GHz
Frequency measurement point	601 points
IF band	1 kHz
Transmission power	0 dBm
Transceiver antenna	Dielectric lens antenna

2.4. Radio wave shielding by cement paste

This section validates the appropriateness of focusing on the cement paste component for improving the radio wave transparency of concrete.

2.4.1. Specimen and experiment overview

Plate-shaped specimens with dimensions of 24 mm in thickness, 360 mm in height, and 400 mm in width were fabricated using cement paste and cement mortar. The height and width of the specimen were set sufficiently large to prevent diffraction of the electromagnetic waves in the testing apparatus. The materials used are listed in **Table 2-5**, the mix proportions in **Table 2-6**, and the appearance of the specimens is shown in **Figure 2-10** and **Figure 2-11**. The water-to-powder ratio (W/P) was set at 55%, a commonly used value. To ensure workability and prevent material segregation, a thickener was added to the cement paste. The density of the thickener was 1 g/cm³ and was included in the unit volume. A mortar mixer was employed for mixing, and the specimens were cast in layers following the directions shown in **Figure 2-10** and **Figure 2-11**. The specimens were demolded 24 hours after casting and then cured in water for one week. Additionally, it was confirmed that there were no defects such as cracks in the areas of the specimens through which radio waves were transmitted.

The transmission loss of the specimen was measured using the testing method described in Sub-section 2.3.2. The test was conducted after the specimen had been cured in water and subsequently placed in a temperature- and humidity-controlled chamber set at 20°C and 40% relative humidity (RH) for at least two weeks, until no further weight change was observed. In the chamber, the specimen was positioned such that the surfaces through which the electromagnetic waves would pass were oriented as the top and bottom faces, as shown in **Figure 2-12**.

Table 2-5 Materials of cement paste specimen and cement mortar specimen

Type	Name	Mark	Ingredients / Physical properties
Powder(P)	Ordinary Portland Cement (OPC)	C	Specific surface area: 3110 cm^2/g Specific gravity: 3.16 g/cm^3
Admixture	Thickener	-	Cellulose-based
Fine aggregate	Crushed sand	S	Hard Sandstone from Hachioji, Tokyo Surface dry density: 2.65 g/cm^3 Water absorption rate: 1.30%

Table 2-6 Mix proportions of cement paste specimen and cement mortar specimen

	Unit weight (kg/m^3)			
	W	P(C)	S	Thickener
Cement paste	631	1148	0	C×0.5%
Cement mortar	297	539	1412	0

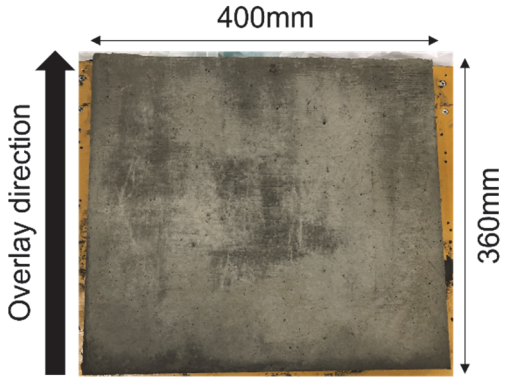

Figure 2-10 W/P55% cement mortar specimen

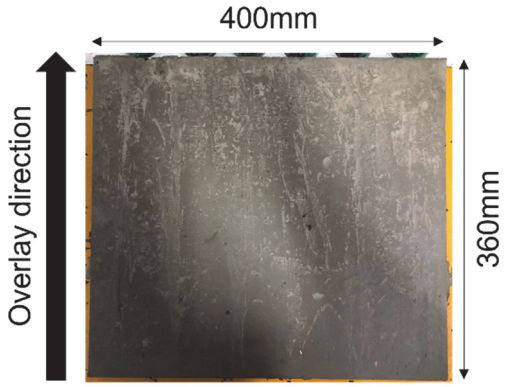

Figure 2-11 W/P55% cement paste specimen

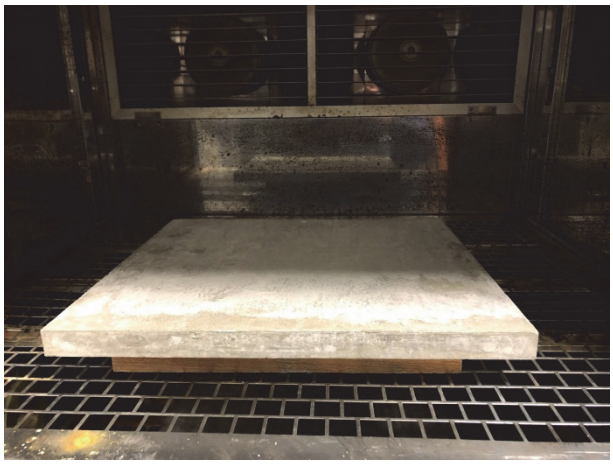

Figure 2-12 Specimen under static condition in a constant temperature and humidity chamber

2.4.2. Results and discussion

The transmission loss measured for each specimen during the radio wave transmission test is

shown in **Figure 2-13**. From **Figure 2-13**, it is evident that the transmission loss of the cement paste specimen is greater than that of the cement mortar specimen, indicating lower radio wave transparency in the cement paste specimen. This result suggests that, in concrete, the hardened cement matrix has a more dominant influence on radio wave shielding compared to the aggregates. Therefore, it is considered that improving the radio wave transparency of the hardened cement matrix can fundamentally enhance the overall radio wave transparency of concrete.

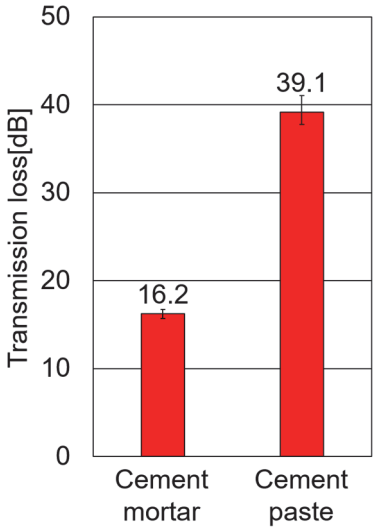

Figure 2-13 Transmission loss of W/P55% cement mortar and W/P55% cement paste

2.5. Effects of radio wave frequency

This section presents the results of an investigation into the effects of radio wave frequency on the radio wave transparency of hardened cement paste.

2.5.1. Specimen and experiment overview

Using the specimens and measurement system described in Section 2.4, similar tests were conducted at different central frequencies (6 GHz, 10 GHz). Since these tests were performed concurrently with those in Section 2.4, the internal moisture conditions of the specimens are assumed to be identical under all conditions.

2.5.2. Results and discussion

The relationship between transmission loss and frequency is shown in **Figure 2-14**. From **Figure 2-14**, it can be observed that transmission loss generally increases linearly with higher frequencies, resulting in a decline in radio wave transparency. Therefore, improving the radio wave transparency for frequencies around 33 GHz is expected to also enhance transparency for lower frequencies.

Additionally, the change in transmission loss with frequency was more pronounced for cement paste specimens than for cement mortar specimens, confirming that hardened cement paste is more sensitive to frequency effects. Consequently, it can be concluded that the higher the frequency of the radio wave, the greater the improvement in radio wave transparency for hardened cement paste.

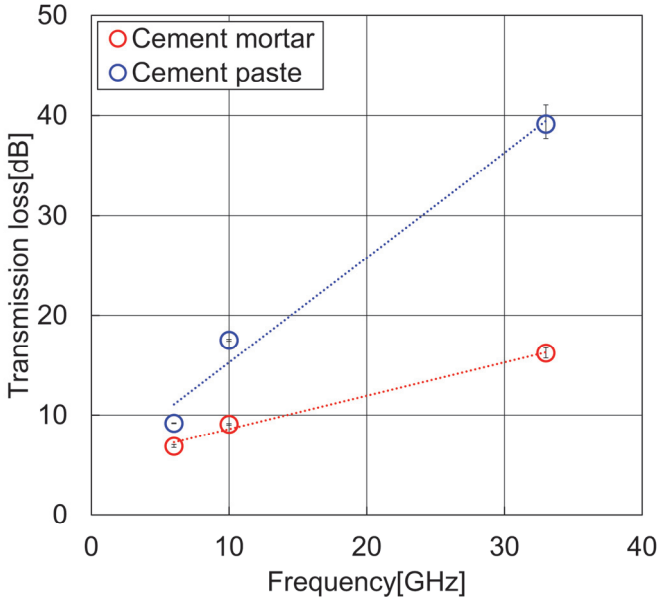

Figure 2-14 Relation between transmission loss and radio wave frequency

2.6. Evaporable water reduction

This section presents the results of an investigation into the improvement of radio wave transparency in hardened cement matrices through the reduction of evaporable water.

2.6.1. Specimen and experiment overview

To examine the influence of evaporable water on the intrinsic radio wave transparency of the material and the effect of drying on improving radio wave transparency, tests were conducted using the cement paste specimens and measurement system described in Section 2.4. By varying the relative humidity (RH), transmission loss was compared between specimens containing evaporable water and those from which evaporable water had been removed. The transmission loss under RH 40% conditions, measured during the tests in Section 2.4, was considered as representing the state with evaporable water present and was used as an indicator of the radio wave transparency of concrete under general usage conditions. The relationship between moisture loss in concrete and relative humidity is shown in **Figure 2-15**[21]. Since evaporable water diminishes in low-humidity environments, specimens were placed in a temperature- and humidity-controlled chamber set at 40°C and RH 0% for at least two weeks after completing the tests under RH 40% conditions, until no further

weight change was observed. Tests were then repeated under the same conditions to evaluate the state where evaporable water had been removed. During this process, specimens were positioned in the chamber such that the surfaces through which the radio waves would pass were oriented as top and bottom surfaces.

Additionally, to evaluate the radio wave transparency of the specimens as structural elements, compressive strength measurements were conducted under each condition to assess the influence of specimen thickness. Specifically, compressive tests on cylindrical specimens were performed the day after the radio wave transmission tests, in accordance with JIS A 1108 standards.

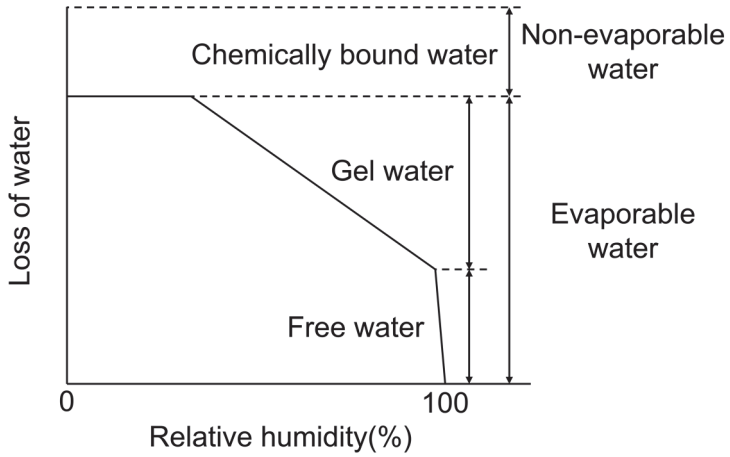

Figure 2-15 Relation between loss of water and relative humidity[21]

2.6.2. Results and discussion

The transmission losses under RH 40% and RH 0% conditions are presented in **Figure 2-16**. As shown in **Figure 2-16**, the transmission loss under RH 0% conditions is approximately 35 dB smaller than that under RH 40% conditions. According to Equation (2-31), this corresponds to a radio wave intensity approximately 3,500 times greater under RH 0% conditions than under RH 40% conditions. Furthermore, based on Equation (2-33), the attenuation constant α is calculated as 3.75×10^{-1} under RH 40% conditions and 3.54×10^{-2} under RH 0% conditions, indicating that α is reduced by about one-tenth under RH 0% conditions. Since a decrease in RH leads to the disappearance of evaporable water, the change in radio wave transparency between RH 40% and RH 0% conditions reflects the degree of shielding caused by evaporable water. It can thus be concluded that, in conventional cement concrete, shielding due to evaporable water predominantly affects radio wave transparency, and its elimination through drying significantly enhances radio wave transparency.

To further analyze the impact of evaporable water on radio wave transparency, conceptual models of the internal structure of the specimens are shown in **Figure 2-17** and **Figure 2-18**. These models are intended to illustrate the factors contributing to shielding within the hardened cement matrix, and

the sizes of particles and voids are not representative of actual dimensions. Additionally, given the 33 GHz frequency used in this study, the wavelength of the radio waves is approximately 9 mm, which is much larger than the scale of the models, and radio wave propagation is simplified as linear.

Under RH 40% conditions, evaporable water—i.e., pore water—is rich in ions dissolved from cement particles, resulting in high electrical conductivity, which is thought to absorb radio waves. Although non-evaporable water, such as chemically bound water, may also contribute to absorption, its impact is considered relatively minor compared to evaporable water. Furthermore, the presence of a continuous medium comprising pore water, cement hydration products, and unhydrated cement particles may obstruct radio wave propagation and influence transparency (Figure 2-17). While hydration products anchored by unhydrated cement particles typically have sizes on the order of several hundred micrometers, this continuous medium, comprising pore water, hydration products, and unhydrated cement, can act as a large obstacle, up to the thickness of the specimen, with high electrical conductivity. The wavelength of the 33 GHz radio waves is approximately 9 mm, compared to the specimen thickness of 24 mm. When the size of an object exceeds the wavelength, it acts as an obstacle to propagation; therefore, this continuous medium likely forms a significant barrier to radio waves. In contrast, under RH 0% conditions, the disappearance of pore water eliminates its absorptive effect. The remaining components of the continuous medium consist solely of hydration products and unhydrated cement, whose sizes, being several hundred micrometers at most, are much smaller than the wavelength of the radio waves. Consequently, the obstructive effect of the continuous medium on radio wave propagation is minimal. Thus, although some absorption by chemically bound water (non-evaporable water) occurs, the majority of the radio waves are presumed to pass through (**Figure 2-18**).

Next, the compressive strengths under RH 40% and RH 0% conditions are shown in **Figure 2-19**. From **Figure 2-19**, it is evident that there is little difference in compressive strength between the two conditions, indicating negligible strength degradation due to drying. However, considering that the compressive strength of cement paste with a water-to-cement ratio (W/C) of approximately 50% at 28 days of age is typically 25-30 N/mm², the observed strength is relatively low, suggesting that a larger component thickness might be required. Furthermore, the low strength may lead to shrinkage cracks during drying, potentially reducing mechanical properties and durability, as well as negatively impacting radio wave transparency. Therefore, enhancing the strength of concrete is considered effective for improving its radio wave transparency as a structural component, while simultaneously maintaining its structural performance and ensuring their long-term stability.

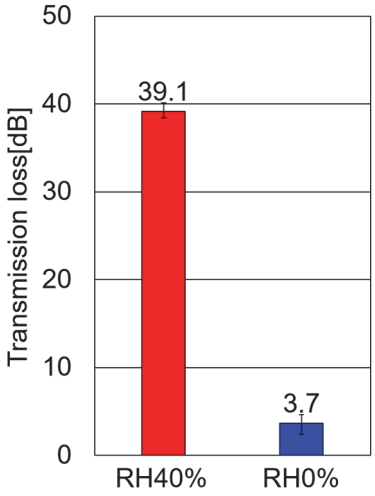

Figure 2-16 Transmission loss of W/P55% cement paste specimen at RH40% condition and at RH0% condition

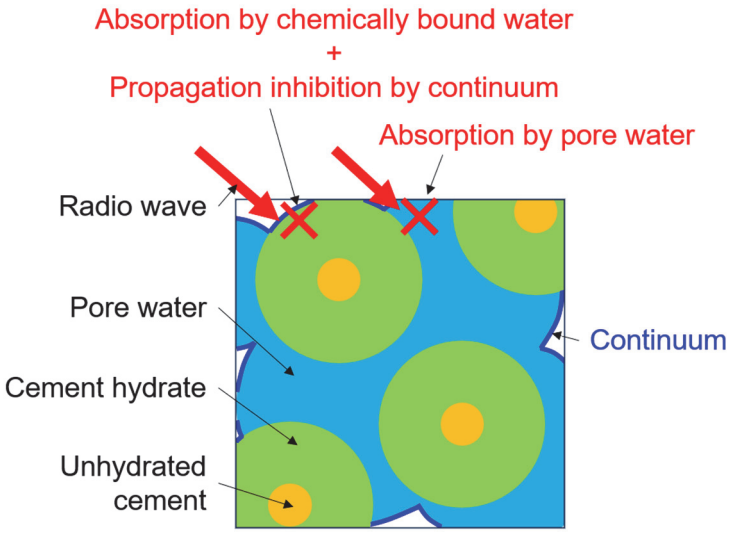

Figure 2-17 Schematic diagram of internal model of W/P55% cement paste specimen at RH40% condition

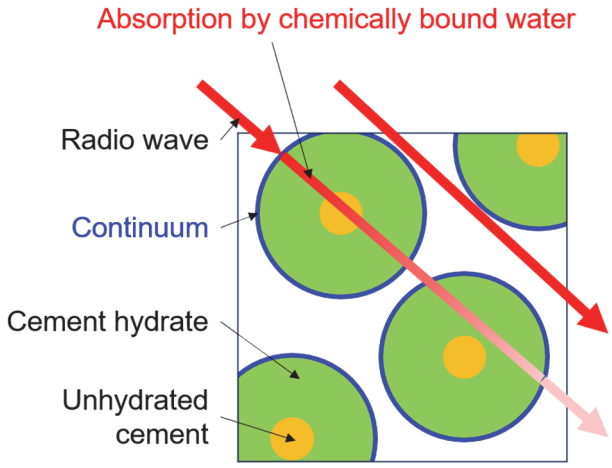

Figure 2-18 Schematic diagram of internal model of W/P55% cement paste specimen at RH0% condition

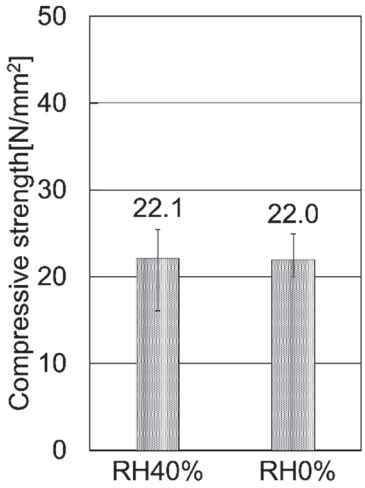

Figure 2-19 Compressive strength of W/P55% cement paste specimen at RH40% condition and at RH0% condition

2.7. Increase in strength

This section presents the results of an investigation into the improvement of radio wave transparency as a structural member through the enhancement of concrete strength.

2.7.1. Specimen and experiment overview

In this study, to increase the strength of the concrete, the water-to-powder ratio (W/P) was set to an extremely low level, thereby reducing the void content. By decreasing the void content, it is expected that not only strength enhancement but also a reduction in pore water, i.e., evaporable water, can be achieved. Furthermore, with a low W/P, self-desiccation is expected to become significant,

potentially leading to an inherently dry internal state without requiring additional drying treatments.

Plate-shaped specimens with dimensions of 24 mm thickness, 360 mm height, and 400 mm width were fabricated using cement paste. The materials used are listed in **Table 2-7** the mix proportions are shown in **Table 2-8**, and the specimen appearance is illustrated in **Figure 2-20**. The W/P was set to 15%, an exceptionally low level, and silica fume, a microfiller, was used to enhance packing density. A mortar mixer was employed for mixing, and the material was placed by layering in the direction shown in **Figure 2-20**. The specimens were demolded 24 hours after casting, subjected to a 30-minute boiling water curing process, and then cured in water for one week. The mix proportion and fabrication procedures were based on the ultra-low water-to-cement ratio concrete fabrication method by Teramoto et al.[22] and the non-porous concrete fabrication method by Kawano et al.[23].

To evaluate the effect of low W/P strength enhancement on material-level radio wave transparency, the same procedure as in Section 2.6 was followed. After the completion of water curing, the specimens were placed in a constant temperature and humidity chamber set at 20°C and RH 40% until their weight stabilized (for more than two weeks). The first radio wave transmission test was then conducted. Subsequently, the specimens were placed in another constant temperature and humidity chamber set at 40°C and RH 0% until their weight stabilized (for more than two weeks), followed by a second radio wave transmission test.

Additionally, to confirm the effect of strength enhancement achieved through the low W/P, a compression test was conducted on cylindrical specimens in accordance with JIS A 1108. However, due to an issue with the test conducted the day after the radio wave transmission test, the results of a compression test performed on a different day using cylindrical specimens prepared with the same mix proportions and subjected to similar temperature and humidity histories were used as the final compressive strength results.

Table 2-7 Materials of W/P15% cement paste specimen

Type	Name	Mark	Ingredients / Physical properties
Powder(P)	Low-Heat Portland Cement (LHC)	C	Specific surface area: 3250 cm^2/g Specific gravity: 3.22 g/cm^3
	Silica fume	SF	Specific surface area: 15-30 m^2/g Specific gravity: 2.20 g/cm^3
Chemical admixture	Superplasticizer	SP	Polycarboxylic acid ether-based
	Deformer	DF	Polyglycol-based

Table 2-8 Mix proportions of W/P15% cement paste specimen

Unit weight (kg/m^3)				
W	P		SP	DF
	C	SF		
316	1895	211	P×1.0%	P×0.2%

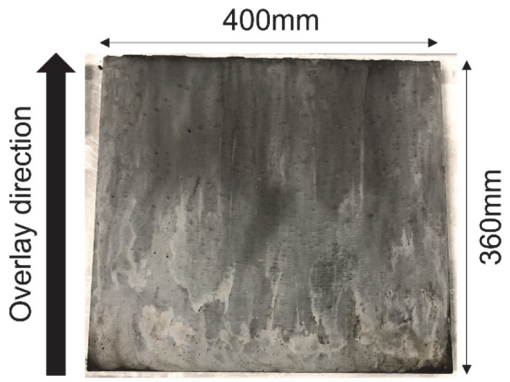

Figure 2-20 W/P15% cement paste specimen

2.7.2. Results and discussion

The compressive strengths under RH40% and RH0% conditions are shown in **Figure 2-21**. From **Figure 2-21**, it is evident that the compressive strength has significantly increased compared to the W/P 55% cement paste specimen, demonstrating that high strength can be achieved through a low W/P ratio. The calculated thickness of wall panels designed to exhibit the same allowable shear strength, based on compressive strength, is presented in **Figure 2-22**. **Figure 2-22** shows that the wall thickness for the W/P 15% cement paste is less than half of that for the W/P 55% cement paste, suggesting that high strength achieved through a low W/P ratio significantly reduces the member thickness, potentially enhancing the radio wave transparency of the structural member.

Next, the transmission losses under RH40% and RH0% conditions are shown in **Figure 2-23**. Comparing the transmission losses of the W/P 55% and W/P 15% cement paste specimens in **Figure 2-16** and **Figure 2-23** reveals that the transmission loss under RH40% conditions is nearly the same. However, under RH0% conditions, there is a notable difference. While the W/P 55% specimen shows significantly reduced transmission loss upon drying, the W/P 15% specimen does not exhibit such a marked improvement in radio wave transparency. Based on Equation (2-36), the ratio of transmitted wave power after passing through the specimens indicates that for the W/P 55% specimen, the transmitted power under RH0% conditions is approximately 3500 times greater than that under RH40%. In contrast, for the W/P 15% specimen, the increase is only about fivefold.

Since the change in radio wave transparency from RH40% to RH0% conditions reflects the extent of shielding due to evaporable water, it can be concluded that the low W/P ratio reduces the shielding

effect of evaporable water. On the other hand, the transparency under RH0% conditions suggests that the shielding due to non-evaporable water, unhydrated cement, and silica fume becomes dominant in the absence of evaporable water. As shown in **Table 2-6** and **Table 2-8**, the volumetric fraction of solid particles in the specimens is approximately 36.3% for the W/P 55% specimen and 68.4% for the W/P 15% specimen, nearly double for the low W/P specimen. A larger solid fraction and lower porosity increase the medium's conductivity[24], likely causing the higher transmission loss. Additionally, the dense microstructure formed by the hydration of unhydrated cement filling the voids, especially in boiled and water-cured low W/P specimens[23], is expected to contain more hydration products. Increased hydration product content raises the amount of chemically bound water, i.e., non-evaporable water, resulting in higher conductivity and transmission loss.

To analyze the effect of a low W/P ratio on radio wave transparency, schematic models of the specimen interiors are shown in **Figure 2-24** and **Figure 2-25**. Under RH40% conditions, radio wave absorption by evaporable water (pore water) and chemically bound water (non-evaporable water), along with propagation obstruction by a continuum composed of pore water, hydration products, unhydrated cement, and silica fume, influences transparency. The increased hydration products amplify absorption by chemically bound water compared to W/P 55% specimens (Figure 2-24). Under RH0% conditions, while pore water absorption disappears, absorption by chemically bound water remains significant. Furthermore, the reduced porosity maintains the continuum size, still obstructing wave propagation (**Figure 2-25**).

The calculated transmission loss of wall panels designed to exhibit the same allowable shear strength, based on the measured transmission loss and compressive strength, is presented in **Figure 2-26**. From **Figure 2-26**, it can be observed that the transmission loss as a structural member for W/P 15% cement paste wall panels is smaller under both RH40% and RH0% conditions compared to the RH40% condition for W/P 55% cement paste wall panels. This indicates that reducing member thickness through high-strength development achieved via a low W/P ratio can improve the radio wave transparency of the member without the need for drying treatment. However, the transmission loss as a structural member under RH0% conditions for W/P 55% cement paste wall panels is even smaller than that for W/P 15% cement paste wall panels. This suggests that, in the current study, improving the material-level radio wave transparency through drying has a greater effect on enhancing the radio wave transparency of the member than reducing the member thickness. Nevertheless, thoroughly drying large and thick members is challenging, and as discussed in 2.5.2, cracks caused by drying are likely to have adverse effects. On the other hand, with a low W/P ratio, the smaller member thickness facilitates internal drying, and the higher strength reduces the likelihood of cracks due to drying. Therefore, considering actual structural scales, this approach appears to be a more practical method. Additionally, given the difficulty of applying drying treatments to large structural members, high-strength development through a low W/P ratio is a highly feasible method.

However, simply reducing the W/P ratio does not improve the material-level radio wave transparency, and even with drying, the improvement is limited. To achieve further enhancement of radio wave transparency, it is necessary to improve the material-level radio wave transparency while maintaining high strength with a low W/P ratio. As discussed earlier, in low W/P cementitious materials, shielding effects caused by unreacted powders and non-evaporable water are expected to dominate radio wave transparency. Since reducing the powder content to alleviate shielding due to unreacted powders is challenging while maintaining high strength with a low W/P ratio, reducing non-evaporable water is expected to be essential for improving radio wave transparency.

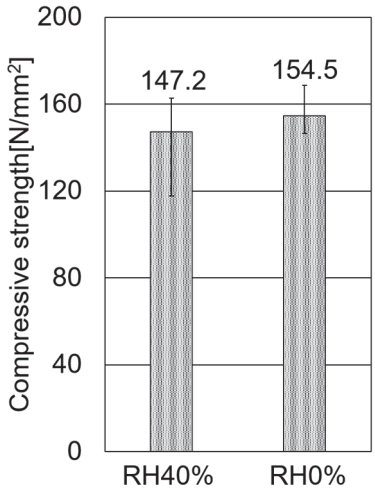

Figure 2-21 Compressive strength of W/P15% cement paste specimen at RH40% condition and at RH0% condition

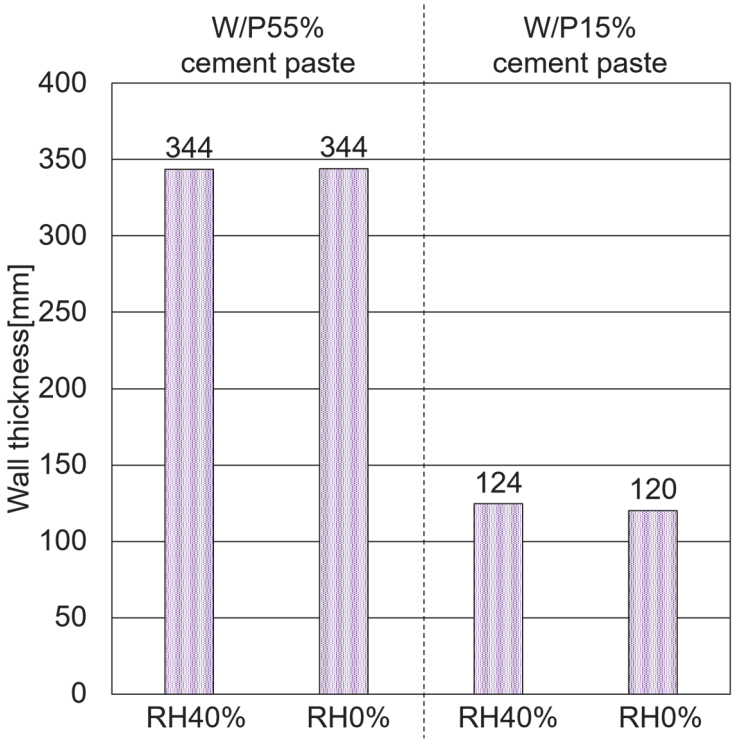

Figure 2-22 Calculated wall thickness of W/P55% cement paste specimen and W/P15% cement paste specimen at RH40% condition and at RH0% condition

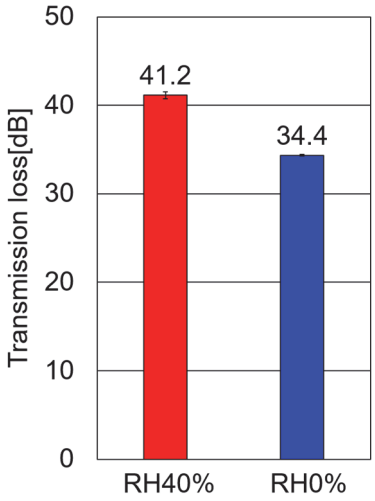

Figure 2-23 Transmission loss of W/P15% cement paste specimen at RH40% condition and at RH0% condition

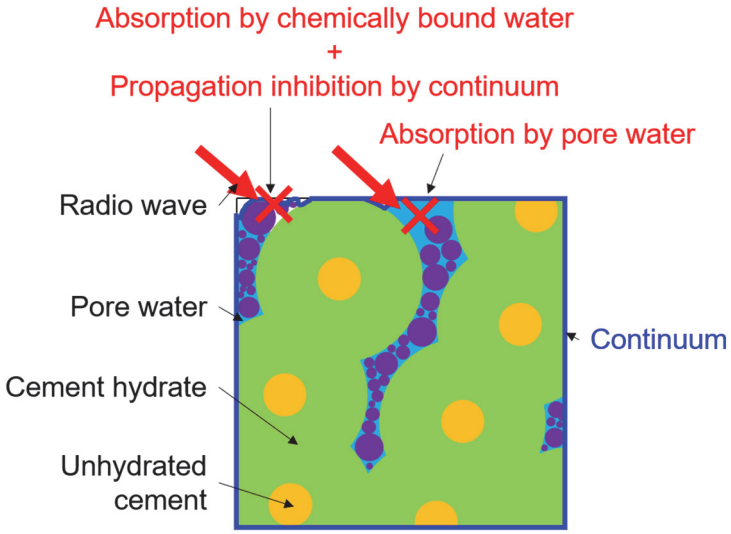

Figure 2-24 Schematic diagram of internal model of W/P15% cement paste specimen at RH40% condition

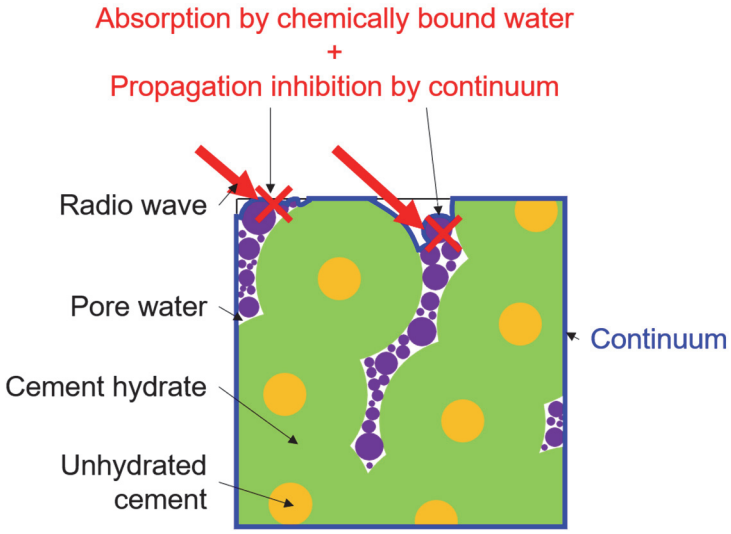

Figure 2-25 Schematic diagram of internal model of W/P15% cement paste specimen at RH0% condition

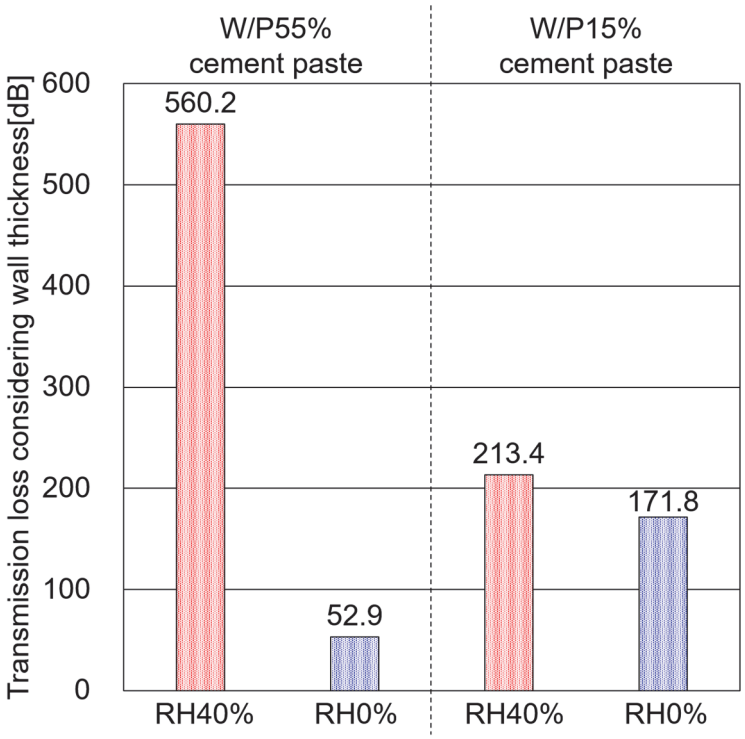

Figure 2-26 Transmission loss considering wall thickness of W/P55% cement paste specimen and W/P15% cement paste specimen at RH40% condition and at RH0% condition

2.8. Non-evaporable water reduction

This section presents the results of the study on improving the radio wave transparency of cementitious materials by reducing non-evaporable water.

2.8.1. Geopolymer overview

Non-evaporable water exists as chemically bound water within cement hydration products. Therefore, to reduce non-evaporable water, it is considered effective to use a solidified material without hydration products as a binder instead of a cementitious material. In this study, geopolymer (GP) was selected as a solidified material without internal hydration products.

As described in Section 1.3, GP is a solidified material formed through the polycondensation reaction of aluminosilicate powders (active fillers) such as fly ash (FA) and ground granulated blast furnace slag (BS) with alkaline silica solutions (alkaline activators) such as sodium silicate solution and sodium hydroxide.

This study focused on the unique solidification mechanism of GP, which involves dehydration-induced polycondensation. Since GP solidifies through a dehydration polycondensation reaction, no hydration products are present in the solidified material, theoretically allowing the complete elimination of non-evaporable water. Unlike hydration reactions, which continue over long periods,

GP is expected to exhibit minimal internal structural changes over time, resulting in stable radio wave transparency and the ability to maintain its initial transmission characteristics for an extended duration.

Additionally, GP forms an amorphous silicate polymer upon solidification, suggesting that its internal structure is similar to that of silicate glass. Silicate glass constitutes the majority of commercial glass products and is generally known for its excellent radio wave transparency. Given this structural similarity, GP is also expected to exhibit superior radio wave transparency.

2.8.2. Specimen and experiment overview

Flat specimens with a thickness of 24 mm, height of 120 mm, and width of 120 mm (**Figure 2-27**) were prepared using the materials listed in Table 2-9 and **Table 2-10** and the mix proportions shown in **Table 2-11**. The ratios of the components in **Table 2-10** are expressed as mass ratios. While GP typically uses a combination of FA and BS as reactive fillers, this study employed only FA as the reactive filler to prevent the formation of hydration products and achieve an amorphous three-dimensional structure similar to glass. Additionally, to enhance strength, the water-to-powder ratio (W/P) was set to an extremely low level of 15%, and the mix proportions of the alkaline solution were adjusted to minimize the water content. Here, W refers to the total water content in the alkaline solution, equivalent to the water content per cubic meter of GP. For this mix, W was 219.5 kg/m³, with an alkali-to-water molar ratio (A/W) of 0.365 and a silica-to-alkali molar ratio (Si/A) of 0.332.

The preparation of the specimens began with the preparation of the alkaline solution, followed immediately by mixing. The solution was prepared in a 60°C water bath, starting with the stirring of sodium silicate solution in a beaker, followed by the addition and further stirring of sodium hydroxide solution. Mixing began immediately while the solution temperature remained elevated. A mortar mixer was used for mixing, and the material was placed in layers as shown in **Figure 2-27**. After placement, the specimens were subjected to sealed heating curing in a 60°C constant temperature and humidity chamber for seven days, followed by demolding. Since the W/P was extremely low and the A/W was high compared to typical GP, there were concerns about unreacted FA and residual alkali components with conventional curing durations. Therefore, the curing period was extended to seven days (from the usual 12 hours) to maximize the reaction between FA and the alkali components and fill voids. It was confirmed that there were no defects such as cracks in the radio wave transmission areas of the specimens.

The transmission loss of the specimens was measured using the same method as in Sections 2.4, 2.6, and 2.7. The measurement system is shown in **Figure 2-28**. The jig used in this test had higher alignment precision than that shown in **Figure 2-9**, with reduced variations in the distance between antennas and between the antennas and specimens. The reduction in specimen size was due to the increased measurement accuracy, which minimized the need to consider radio wave diffraction. It was verified that the differences in jigs did not affect the transmission loss.

As in Sections 2.6 and 2.7, the tests were conducted twice under different relative humidity (RH) conditions. Specifically, after demolding, the specimens were placed in a 20°C, RH40% constant temperature and humidity chamber for more than two weeks until no weight changes were observed, followed by the first radio wave transmission test. Subsequently, the specimens were placed in a 40°C, RH0% constant temperature and humidity chamber for more than two weeks until no weight changes were observed, followed by the second radio wave transmission test. The specimens were placed in the chambers such that the radio wave transmission surface faced upwards and downwards.

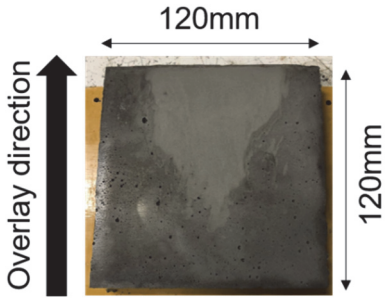

Figure 2-27 W/P15% geopolymer specimen

Table 2-9 Materials of W/P15% geopolymer specimen

Type	Name	Mark	Ingredients / Physical properties
Active Filler (P)	Fly ash	FA	JIS Type II Specific surface area: 3690 cm^2/g Specific gravity: 2.29 g/cm^3
Alkaline solution (L)	Sodium silicate solution	SS	Listed in **Table 2-10**
	Sodium hydroxide	SH	Granular, Purity: 98.0% or higher
	Water	LW	Deionized water
Chemical admixture	Superplasticizer	SP	Polycarboxylic acid ether-based
	Deformer	DF	Polyglycol-based

Table 2-10 Ingredients and physical properties of sodium silicate solution manufactured by FUJIFILM Wako Pure Chemical Corporation

Test case	Specified value
Iron (Fe)	～0.03%
Sodium oxide (Na_2O)	17.0～19.0%
Silicon dioxide (SiO_2)	35.0～38.0%
Molar concentration (SiO_2/Na_2O)	2.06～2.31
Concentration	52.0～57.0%

Table 2-11 Mix proportions of W/P15% geopolymer specimen

Unit weight (kg/m^3)					
P	L			SP	DF
FA	SS	SH	LW		
1463	243	122	122	P×2.0%	P×0.2%

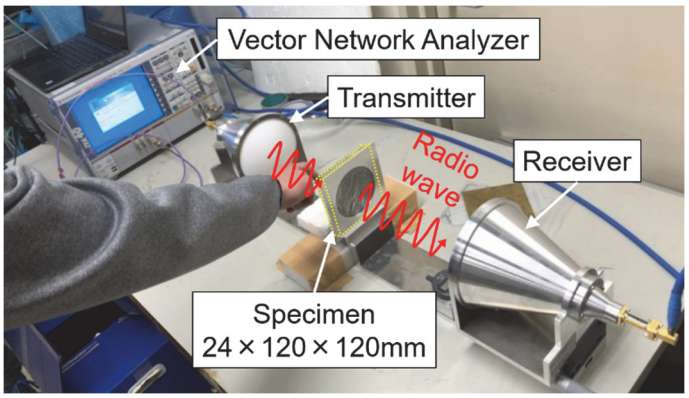

Figure 2-28 Radio wave transparency tenting system for W/P15% geopolymer specimen

2.8.3. Results and discussion

The compressive strength under RH40% and RH0% conditions is shown in **Figure 2-29**. From **Figure 2-29**, it is evident that the compressive strength of the W/P15% geopolymer (GP) specimens is comparable to that of W/P15% cement paste specimens, demonstrating that high strength can be achieved with GP as the binder at a low W/P ratio.

Based on the measured compressive strength, the thicknesses of wall panels made from W/P55% cement paste, W/P15% cement paste, and W/P15% GP, designed to exhibit the same allowable shear strength, were calculated using the procedure described in Sun-section 2.7.2. The results are shown in **Figure 2-30**. From **Figure 2-30**, it is clear that the thickness of W/P15% GP wall panels is approximately equal to that of W/P15% cement paste wall panels. This indicates that low W/P GP, like

low W/P cement paste, can significantly reduce the thickness of structural components, thereby potentially enhancing radio wave transparency as a structural member.

The transmission loss under RH40% and RH0% conditions is shown in **Figure 2-31**. Comparing **Figure 2-16**, **Figure 2-23**, and **Figure 2-31**, the transmission loss of the W/P15% GP specimens is lower under RH40% conditions than that of the W/P55% and W/P15% cement paste specimens. Under RH0% conditions, while the W/P55% cement paste specimen exhibit the lowest transmission loss, the W/P15% GP specimen approach that value. According to Equation (2-36), the radio wave transparency of W/P15% GP specimens under RH40% is approximately 27 times higher, and under RH0% is approximately 331 times higher than that of the W/P55% cement paste specimens under RH40%. In the W/P15% GP specimens, the difference in transmission loss between RH40% and RH0% conditions is approximately 11 dB, similar to that observed for W/P15% cement paste specimens. From Equation (2-36), the radio wave transparency of the W/P15% GP specimens under RH0% is about 13 times greater than under RH40%.

To further investigate the relationship between evaporable water and radio wave transparency, the difference in transmission loss between RH40% and RH0% conditions and the unit volume weight change from the first to the second test are shown in **Figure 2-32**. Weight change due to reduced RH is attributed to the evaporation of evaporable water, linking weight change to evaporable water content. From **Figure 2-32**, a linear relationship between transmission loss difference and weight change is evident, suggesting that the shielding effect due to evaporable water increases linearly with the amount of evaporable water.

To clarify the relationship between non-evaporable water and radio wave transparency, the relationship between transmission loss under RH0% conditions and the volume fraction of powder is shown in **Figure 2-33**, while the relationship between transmission loss under RH0% conditions and the volumetric filling ratio of the specimens is presented in **Figure 2-34**. The volumetric filling ratio of the specimens was calculated based on the weight change of the specimens, from the end of water curing to post-drying for cement paste specimens, and from demolding to post-drying for the GP specimen. A comparison between W/P15% cement paste specimen and W/P15% GP specimen indicates that the difference in transmission loss is significantly larger than the difference in powder volume fraction. Additionally, despite the volumetric filling ratio of W/P15% GP specimen being approximately equal to or slightly larger than that of W/P15% cement paste specimen, the transmission loss of W/P15% GP specimen is lower. Under RH0% conditions, the shielding effect in W/P15% cement paste specimens is attributed to the filled powder and non-evaporable water. However, since GP reaction products contain no non-evaporable water, the shielding effect in W/P15% GP specimens is solely due to the filled powder. Therefore, the difference in transmission loss between these specimens represents the magnitude of shielding caused by non-evaporable water. It is suggested that approximately half of the transmission loss in W/P15% cement paste specimens may be due to non-

evaporable water, which is absent in W/P15% GP specimens.

Based on these considerations, models of the internal structure of W/P15% GP specimens are shown in **Figure 2-35** and **Figure 2-36**. Within the solidified body of GP, it is hypothesized that gel-like reaction products surround unreacted FA particles, with voids scattered throughout. In these models, the size of the powder and voids differs from reality, and the propagation of radio waves is simplified as linear.

Under RH40% conditions, the shielding effects on radio waves are expected to result from the absorption by void water (evaporable water) and the obstruction to propagation caused by a continuum composed of void water, geopolymer reaction products, and unreacted FA particles. The absence of chemically bound water (non-evaporable water) likely makes radio wave transmission easier compared to low W/P cement paste specimens. Despite the small void fraction and large continuum size relative to the wavelength, the continuum's electrical conductivity is hypothesized to be lower than that of cementitious materials due to differences in internal structure, resulting in less obstruction and easier radio wave propagation (**Figure 2-35**). Under RH0% conditions, the absence of void water eliminates absorption by evaporable water, and the continuum, composed only of reaction products and unreacted FA particles, further reduces conductivity, leading to minimal obstruction and improved propagation (**Figure 2-36**).

Using the calculated wall panel thicknesses and measured transmission losses, the transmission loss as a structural component for W/P55% cement paste, W/P15% cement paste, and W/P15% GP panels designed to achieve the same allowable shear strength was calculated following the procedure in Sub-section 2.7.2. The results are shown in **Figure 2-37**. From **Figure 2-37**, the structural transmission loss of W/P15% GP wall panels is smaller than that of W/P15% cement paste panels under both RH40% and RH0% conditions. Notably, under RH0% conditions, the transmission loss approaches that of W/P55% cement paste panels under RH0%. Low W/P GP significantly improves the radio wave transparency of structural members even without drying treatments. Thus, the combination of non-evaporable water reduction through the application of GP and high strength achieved by a low W/P ratio is an effective and feasible method for enhancing the radio wave transparency of concrete components. Additionally, like low W/P cement paste, low W/P GP allows for reduced component thickness, making it easier to dry internally. Its high strength also reduces the likelihood of cracks caused by drying. Therefore, combining evaporable water reduction through drying, non-evaporable water reduction through GP application, and high strength via a low W/P ratio is an effective approach to maximize radio wave transparency, enhance structural performance, and maintain these properties over an extended period.

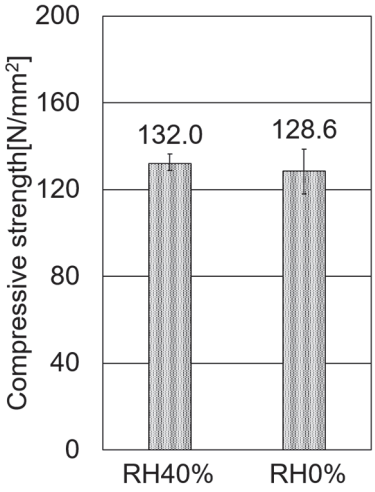

Figure 2-29 Compressive strength of W/P15% geopolymer specimen at RH40% condition and at RH0% condition

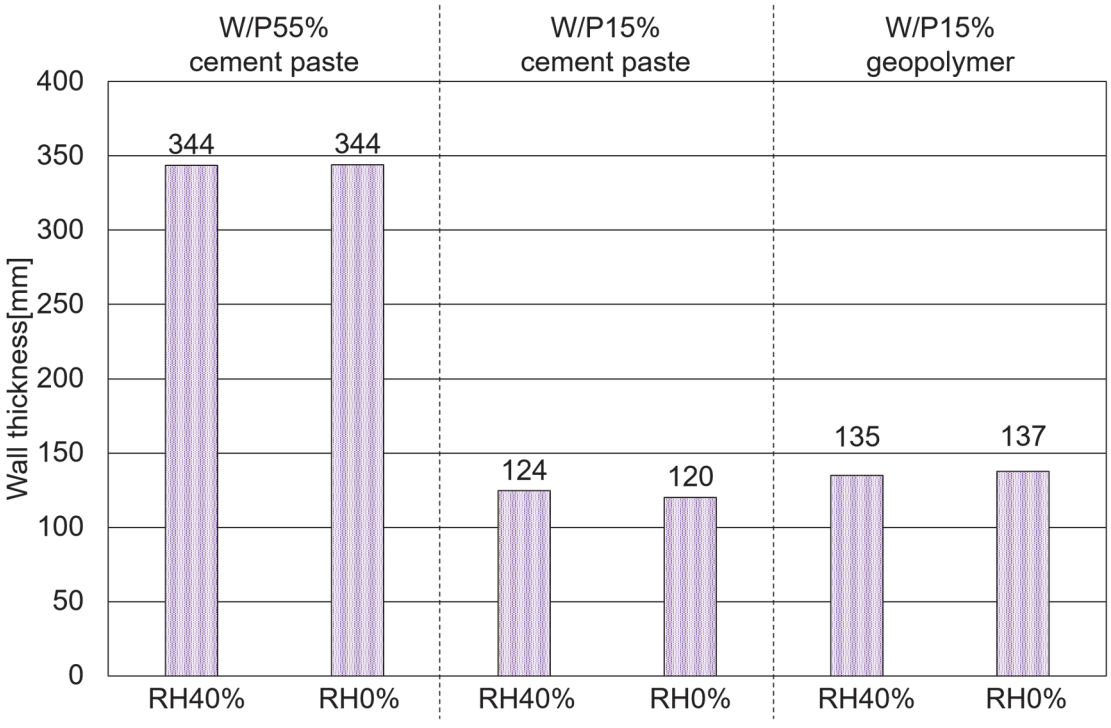

Figure 2-30 Calculated wall thickness of W/P55% cement paste specimen, W/P15% cement paste specimen and W/P15% geopolymer specimen at RH40% condition and at RH0% condition

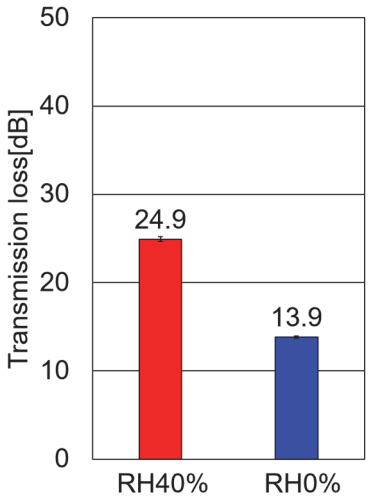

Figure 2-31 Transmission loss of W/P15% geopolymer specimen at RH40% condition and at RH0% condition

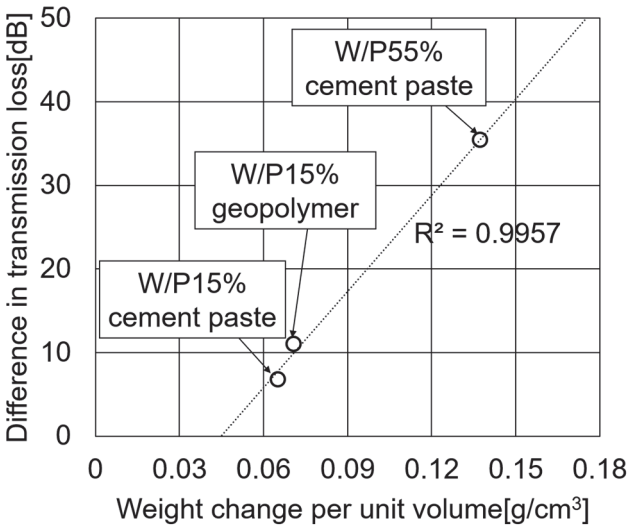

Figure 2-32 Relation between the difference in transmission and the weight change per unit volume

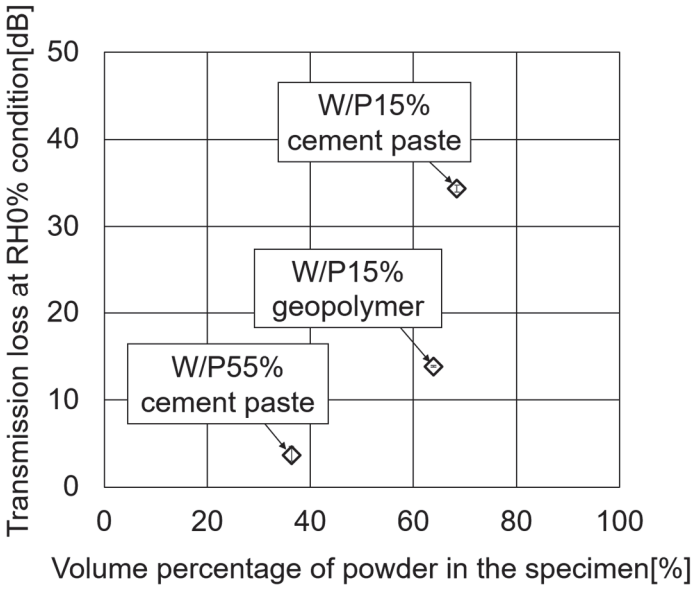

Figure 2-33 Relation between the transmission loss at RH0% condition and the volume percentage of powder in the specimen

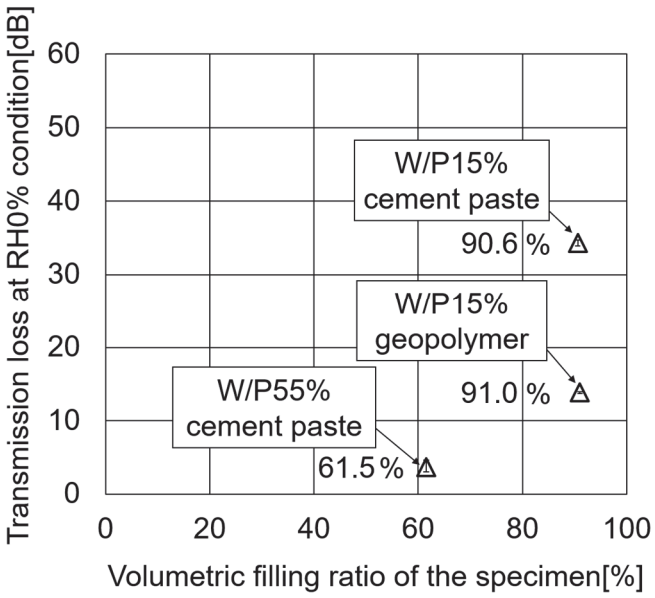

Figure 2-34 Relation between the transmission loss at RH0% condition and the volumetric filling ratio of the specimen

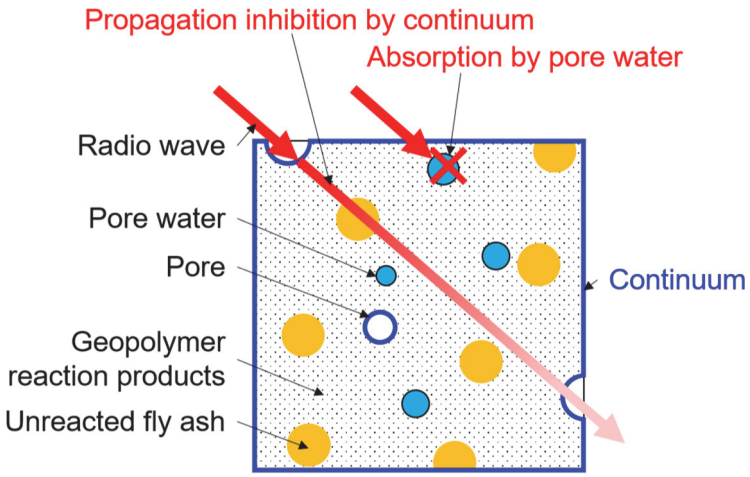

Figure 2-35 Schematic diagram of internal model of W/P15% geopolymer specimen at RH40% condition

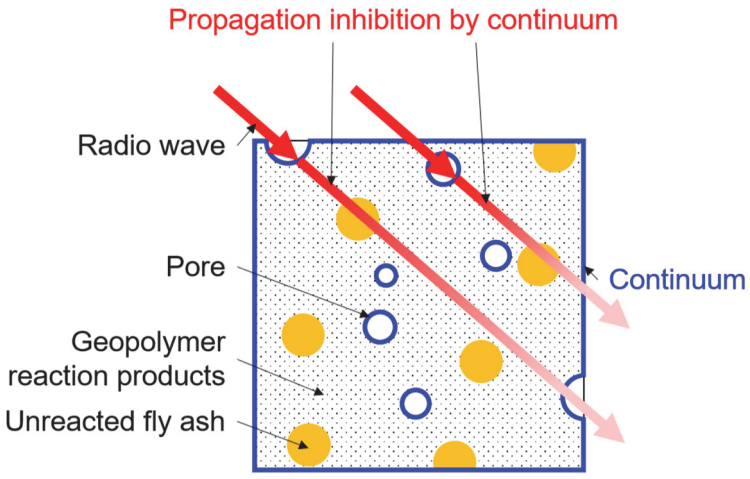

Figure 2-36 Schematic diagram of internal model of W/P15% geopolymer specimen at RH0% condition

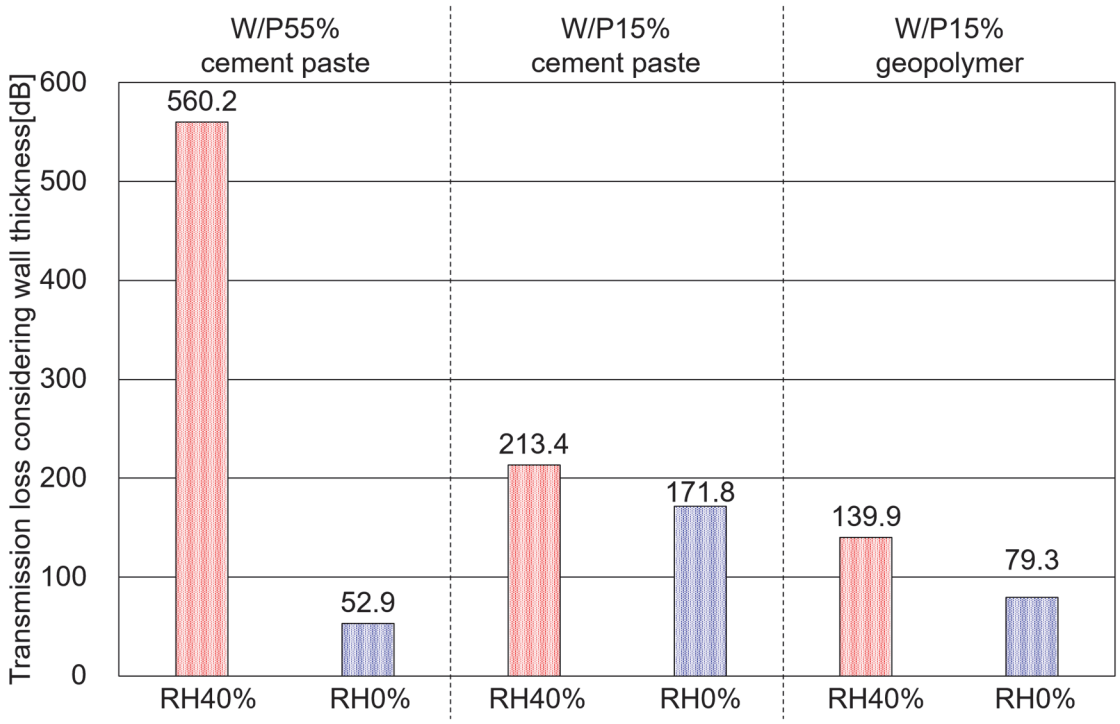

Figure 2-37 Transmission loss considering wall thickness of W/P55% cement paste specimen, W/P15% cement paste specimen and W/P15% geopolymer specimen at RH40% condition and at RH0% condition

2.9. Future prospects

The relationship between evaporable water, non-evaporable water, and radio wave transparency obtained in this study is based on a relative evaluation. The mechanisms by which water content, powder, and reaction products contribute to radio wave shielding, as well as the mechanisms by which the proposed method improves radio wave transparency, remain speculative. To establish a method for enhancing the radio wave transparency of concrete, it is essential to quantitatively clarify the relationship between water content and radio wave transparency and to elucidate the mechanisms of both radio wave shielding and transparency enhancement. For this purpose, future studies should focus on collecting and accumulating various data related to internal structure, water content, and radio wave transparency. This includes measuring total porosity using multiple methods such as mercury intrusion porosimetry, observing the microstructure using SEM, determining evaporable water content through drying at 105°C and moisture meters, measuring non-evaporable water content through ignition loss, and evaluating the electrical conductivity and dielectric properties of specimens and reaction products. Furthermore, when considering drying treatment, there may exist an optimal condition that balances high radio wave transparency and sufficient mechanical properties. Identifying this optimal condition requires further investigations under various conditions.

Additionally, the low W/P geopolymer (GP) used in this study exhibits low fluidity and a short setting time, making it essential to improve workability for practical manufacturing applications.

Furthermore, this study primarily aimed to enhance the radio wave transparency of the cement matrix. However, for practical use as a building material, a detailed investigation that includes aggregates is necessary. While the study demonstrated significant improvements in the radio wave transparency of concrete elements, it is still not at a practical level, considering that the link budget for millimeter-wave communication ranges from 110 to 140 dB. As indicated in Section 2.4, aggregates contribute to improved radio wave transparency, suggesting that incorporating aggregates may further enhance the transparency of concrete elements. However, introducing aggregates may lead to cracking due to aggregate-induced constraints, which could negatively impact radio wave transparency. Therefore, future research should examine the influence of aggregate content and type on radio wave transparency, as well as strategies for preventing and mitigating crack formation.

Moreover, while this study evaluated radio wave transparency under the assumption of wall elements, future research should explore its applicability to other structural components. In particular, floor elements differ from walls in that they are less likely to have openings, making the intrinsic radio wave transparency of the material even more critical.

2.10. Concluding remarks

The findings obtained from the investigation into methods for improving the radio wave transparency of unreinforced concrete members are summarized as follows:

(1) The radio wave transparency of concrete is closely related to its electrical properties, particularly conductivity and relative permittivity. Lower conductivity results in reduced attenuation of radio waves.

(2) The conductivity and relative permittivity of concrete vary with its internal moisture state. Consequently, it is inferred that lower moisture content leads to reduced attenuation of electromagnetic waves, suggesting that reducing moisture content is effective for improving radio wave transparency.

(3) The radio wave transparency of concrete as a structural member significantly depends on the member thickness. Reducing the thickness through the high-strength design of concrete is considered effective for enhancing radio wave transparency.

(4) It is highly likely that the dominant factor in radio wave shielding within concrete is not the aggregate but the cementitious matrix.

(5) A primary factor reducing the radio wave transparency of cementitious matrix in conventional concrete is likely the shielding effect caused by evaporable water within the matrix.

(6) Drying the cementitious matrix to reduce evaporable water enhanced its material-level radio wave transparency by approximately 3,500 times. However, due to its low strength, drying

induced cracking, raising concerns about long-term mechanical properties, durability, and radio wave transparency.

(7) High strength was achieved by adopting an extremely low water-to-powder ratio (W/P). This approach potentially reduces member thickness, thereby improving structural radio wave transparency while also increasing resistance to adverse effects caused by drying.

(8) When the W/P ratio is extremely low, the material's inherent radio wave transparency improves little even with drying. It is hypothesized that shielding effects are dominated by unreacted powders and non-evaporable water. Therefore, further improvements in radio wave transparency require a reduction in non-evaporable water while maintaining a low W/P ratio.

(9) The use of geopolymer (GP) as a binder in place of the cementitious matrix reduced non-evaporable water. The combination of GP with high strength achieved through a low W/P ratio was shown to enhance material-level radio wave transparency without drying and further improve it with drying. This approach holds significant potential to maximize radio wave transparency as a structural member while improving structural performance and maintaining these properties over the long term.

(10) To establish methods for improving the radio wave transparency of concrete, it is essential to quantitatively clarify the relationship between water content and radio wave transparency and to elucidate the mechanisms underlying radio wave shielding and transparency enhancement. This requires the collection and accumulation of diverse data on internal structures, moisture content, and radio wave transparency. Additionally, further studies on improving the workability of low W/P GP and investigating its application to aggregates and other structural components are necessary.

(11) The study demonstrated that the use of low-W/P GP as a binder is effective for improving the radio wave transparency of unreinforced concrete members, with further improvements expected through drying. However, further investigations are necessary to establish this method as a viable approach.

References

(1) 唐澤好男. ディジタル移動通信の電波伝搬基礎. 改訂版, コロナ社, 2016, ISBN978-4-339-00883-8. https://cir.nii.ac.jp/crid/1130282268804959872.

(2) 高田潤一. 電波伝搬の基礎理論. 映像情報メディア学会誌. 2016, Vol. 70, No. 1, pp. 142‐148.

(3) Saegusa, K. Fundamentals of Electromagnetic Wave Shielding and Absorbing Technology. Journal of The Surface Finishing Society of Japan. 2019, Vol. 70, No. 11, pp. 534‐539.

(4) 伊藤繁夫, 長谷川弘治. 基礎からの電磁波工学. 日新出版, 2008, 実用理工学入門講座. https://ndlsearch.ndl.go.jp/books/R100000002-I000009321341.

(5) 清水康敬. 電磁波の吸収と遮蔽. 日経技術図書, 1989. https://ndlsearch.ndl.go.jp/books/R100000002-I000002029894.

(6) Chino, M., Nikawa, Y., Okada, F. Permittivity measurement of light-weight concrete as a function of water absorption rate at VHF and UHF frequencies using strip line reflection method. The Institute of Image Information and Television Engineers Technical Report. 1994, Vol. 18, No. 11, pp. 33–38.

(7) Hayashi, T., Takai, S. Research on Radio Wave Absorber Composed of Mortar ~Effects of Differences in Water Content Condition~. 奈良県産業振興総合センター研究報告. 2021, No. 47, pp. 11‐15.

(8) 野田一弘, 河野広隆, 久田真. 交流作用時の硬化コンクリートの電気的性質に関する基礎的研究. コンクリート工学年次論文集. 2003, Vol. 25, No. 1, pp. 575‐580.

(9) Guihard, Vincent, Patapy, Cédric, Sanahuja, Julien, Balayssac, Jean-Paul, Taillade, Frédéric, Steck, Barthélémy. Effective medium theories in electromagnetism for the prediction of water content in cement pastes. International Journal of Engineering Science. 2020, Vol. 150, pp. 103273.

(10) Dinh, Tin Trong, Hegler, Sebastian, Liebscher, Marco, Navarro de Sosa, Iñaki, Li, Huanyu, Plettemeier, Dirk, Drossel, Welf-Guntram, Mechtcherine, Viktor. Dielectric material characterization of concrete in GHz range in dependence on pore Vol.ume and water content. Construction and Building Materials. 2021, Vol. 311, pp. 125234.

(11) 生田周史, 中川元宏, 山本貴士, 服部篤史, 宮川豊章. 各種要因がコンクリートの比抵抗に与える影響に関する実験的研究. 土木学会第 59 回年次学術講演会, pp. 187-188. 2004.

(12) Makita, T. The Basic Electrical Characteristic of the Concrete. The Journal of the Institute of Electrical Installation Engineers of Japan. 2009, Vol. 29, No. 9, pp. 783‐788.

(13) Soutsos, M. N., Bungey, J. H., Millard, S. G., Shaw, M. R., Patterson, A. Dielectric properties of concrete and their influence on radar testing. NDT & E International. 2001, Vol. 34, No. 6, pp. 419–425.

(14) Hanehara, S., Sawaki, D. Pore Structure of Hardened Concrete and Its Performallce. Gypsum & Lime. 1992, Vol. 1992, No. 240, pp. 314‐323.

(15) 魚本健人. コンクリート構造物のマテリアルデザイン. オーム社, 2007, ISBN978-4-274-20420-3. https://books.google.co.jp/books?id=cd70PQAACAAJ.

(16) Koike, K. Fundamental Study on Effect of Water Movement on Chloride Ion Penetration in Concrete. Kagoshima University, 2016. https://ci.nii.ac.jp/naid/500000971670.

(17) T. C. Powers and T. L. Brownyard. Studies of the Physical Properties of Hardened Portland Cement Paste. ACI Journal Proceedings. 1946, Vol. 43, No. 9.

(18) Brouwers, H. J. H. The work of Powers and Brownyard revisited: Part 1. H. F. W. Taylor

Commemorative Issue. 2004, Vol. 34, No. 9, pp. 1697–1716.

(19) Architectural Institute of Japan. AIJ Standard for Structural Calculation of Reinforced Concrete Structures. 2018.

(20) Architectural Institute of Japan. 壁式鉄筋コンクリート造設計・計算基準・同解説. 2015.

(21) Mehta, P. Kumar, Monteiro, Paulo J. M. Concrete: Microstructure, Properties, and Materials. 4th Edition, New York, McGraw-Hill Education, 2014, ISBN978-0-07-179787-0. https://www.accessengineeringlibrary.com/content/book/9780071797870.

(22) Teramoto A., Maruyama, I. TEMPERATURE DEPENDENCY OF AUTOGENOUS SHRINKAGE OF SILICA FUME CONCRETE WITH LOW W/B RATIO. Journal of Structural and Construction Engineering (Transactions of AIJ). 2008, Vol. 73, No. 634, pp. 2069‐2076.

(23) Kono, K., Mori, K., Tada, K., Tanaka, S. Development of Concrete Developing the World's Highest Strength and Potential for Further Performance Improvement. Concrete Journal. 2016, Vol. 54, No. 7, pp. 702‐709.

(24) Takeuchi, M. Introduction to Electromagnetism and Electrostatics (II) -Electromagnetism and Electric Constants of Materials-. Journal of the Imaging Society of Japan. 2006, Vol. 45, No. 2, pp. 194‐203.

CHAPTER 3. PERFORMANCE EVALUATION OF GEOPOLYMER

3.1. Motivation

Through the investigation conducted in CHAPTER 2, it was confirmed that the use of low water-to-powder ratio (W/P) geopolymer (GP) is effective in enhancing the radio wave transparency of concrete. However, there are no prior studies on low W/P GPs, and properties other than those examined in CHAPTER 2 remain entirely unexplored. GP itself has many properties and mechanisms that are insufficiently understood and systematized compared to conventional cement concrete, limiting its application in structures.

In this chapter, to advance the application of low W/P GP in structures and expand its broader use, the investigation focuses on time-dependent deformation properties, which significantly influence the long-term radio wave transparency and mechanical performance. The results of these investigations are presented here.

3.2. Literature review

Hardened concrete is known to undergo volumetric changes over time due to internal moisture state variations and moisture migration. These volumetric changes are referred to as time-dependent deformations, with shrinkage and creep being the most prominent examples. Accurate prediction of these characteristics is essential for the application of concrete in structures. In this section, the effects of shrinkage and creep on concrete structures are discussed. Additionally, the mechanisms and influencing factors of shrinkage and creep in cement concrete are reviewed, and the current state of research on shrinkage and creep in GP is described.

3.2.1. Effects of shrinkage and creep on concrete structures

In structural elements, concrete experiences restraint due to reinforcement and other components, which induces tensile stresses in the concrete as shrinkage occurs. As a result, the apparent tensile strength of the concrete may decrease, or cracks may develop. After cracking, shrinkage may cause the crack width to increase further. Although cracks in reinforced concrete structures do not usually compromise their mechanical performance immediately, from the perspective of aesthetics and durability, cracks are undesirable and must be kept within acceptable limits[1]. Recent studies have revealed that shrinkage-induced cracks, although not significantly affecting ultimate strength, can reduce the stiffness of elements[2, 3]. Moreover, due to restraint between members, deformation can occur in non-dried members, leading to a reduction in the overall stiffness of the structure[4]. Consequently, shrinkage can influence the natural frequencies and vibration modes of structural elements and structures as a whole. It has been suggested that shrinkage must be considered when evaluating the seismic response of concrete structures[4].

Furthermore, shrinkage-induced cracks accelerate moisture absorption in concrete, potentially worsening radio wave transparency. From the perspective of radio wave transparency, it is therefore desirable to minimize the occurrence and propagation of cracks. In particular, when drying elements to achieve higher radio wave transparency, the risk of cracking increases, making it essential to control drying shrinkage.

On the other hand, creep in concrete generally acts to relax (reduce) stresses in both the concrete and reinforcement within the structure. Thus, neglecting creep and estimating indeterminate stresses based on elastic analysis can lead to an overestimation of stresses, yielding conservative results. However, when precise predictions of stress induced by temperature and shrinkage are required, the effects of concrete creep must be accurately considered. Notably, ignoring creep is dangerous when calculating deformation, as it can lead to an underestimation of time-dependent deformations such as deflection(27). Recent studies have shown that, over a timescale of decades, the impact of creep in actual structures is more significant than previously anticipated. Excessive deflections in prestressed concrete (PC) long-span bridges, as well as excessive deflections and delayed shear cracking in underground reinforced concrete (RC) structures, are likely primarily caused by shrinkage and creep in concrete[5-8].

Additionally, shrinkage and creep are known to significantly impact the performance of prestressed concrete (PC)[1]. PC is a structural system in which high-strength prestressing steel is used to apply compressive forces to concrete, reducing the likelihood of tensile stresses developing in the concrete when the structure is subjected to external loads. This mechanism helps suppress cracking, allows for a reduction in cross-sectional dimensions, enables the construction of longer spans, and minimizes deflection. As mentioned earlier, from the perspective of radio wave transparency, crack suppression is also essential. Therefore, the introduction of prestress can be considered effective in maintaining radio wave transparency. However, in PC structures, concrete shrinkage leads to a reduction in prestress. Additionally, since concrete in PC structures is continuously subjected to compressive stress due to prestressing, creep deformation progresses over time, further contributing to the loss of prestress, similar to shrinkage. Thus, in PC structures, shrinkage and creep both act as factors that reduce prestress, leading to crack formation and a decline in structural performance. Consequently, it is crucial to accurately predict the extent of shrinkage and creep to ensure the long-term durability and performance of PC structures[1].

3.2.2. Shrinkage mechanism of cement concrete

Shrinkage in cement concrete is mainly categorized into two types: drying shrinkage and autogenous shrinkage.

Drying shrinkage refers to the phenomenon where concrete loses moisture due to drying, leading to contraction of the hardened matrix. Drying shrinkage often generates significant stress due to

deformation, directly causing cracks and thus frequently posing problems. The relationship between drying shrinkage strain and mass loss in a cementitious matrix can be schematically represented as shown in **Figure 3-1**, with four distinct regions differing in gradient (except under heating conditions)[9]. Region ① occurs when the relative humidity exceeds 85%, where shrinkage is minimal relative to the degree of mass loss. Region ② occurs between 90–40% relative humidity, where shrinkage is significant relative to mass loss, making it critical in practical applications. Region ③ shows little shrinkage despite mass loss. Region ④ occurs between 20–0% relative humidity, where the greatest shrinkage occurs relative to mass loss. These phenomena are closely related to the role of water within the hardened matrix. In Region ①, water is removed from relatively large pores, where interactions between water and the solid surface are weak, thus having little influence on shrinkage. In Region ②, capillary water in capillary pores is removed, and shrinkage due to capillary tension becomes pronounced. In Region ③, capillary water has been depleted, and only adsorbed water in capillary walls is lost through drying, contributing minimally to shrinkage. In Region ④, gel water and intracrystallite water within calcium silicate hydrate (C-S-H) are lost, causing structural changes in the C-S-H and resulting in significant shrinkage.

Drying shrinkage is considered a physical behavior associated with moisture loss rather than a result of chemical or mineralogical changes in cement hydrates. The primary theories explaining the mechanism of drying shrinkage include capillary tension, disjoining pressure, surface tension, and intracrystallite water migration mechanisms.

The capillary tension mechanism attributes elastic volumetric reduction of the hardened matrix to tensile stress induced in capillary water by meniscus formation during drying (**Figure 3-2**). Based on the principles of interfacial physical chemistry, water with a concave surface has a lower vapor pressure than water with a flat surface due to surface tension. When the water surface is hemispherical, the relationship between the radius of curvature of the vapor-liquid interface and vapor pressure can be expressed by Equation (3-1) (Kelvin's equation). Here, r_K, known as the Kelvin radius, represents the radius of a tube at which the relative humidity of the air equals the relative humidity of water within the tube, forming a state of equilibrium where neither evaporation nor condensation occurs.

$$\ln\frac{p}{p_0} = \frac{2\gamma M}{RT\rho}\frac{1}{r_K} \qquad (3-1)$$

Where:

p: Vapor pressure (N/m^2)

p_0: Saturation vapor pressure (N/m^2)

γ: Surface tension of the liquid (N/m)

M: Molecular weight of the liquid (kg/mol)

R: Gas constant (J/K・mol)

T: Absolute temperature (K)

ρ: Density of the liquid (kg/m^3)

r_K: Radius of the capillary (m)

At this point, the tensile stress (capillary tension) generated in the capillary water is given by Equation (3-2) (Young-Laplace Equation).

$$\Delta p = \frac{2\gamma}{r_K} \qquad (3-2)$$

Where:

Δp: Capillary tension (N/m^2)

γ: Surface tension of the liquid (N/m)

r_K: Radius of the capillary (m)

From Equations (3-1) and (3-2), Equation (3-3) is derived.

$$\Delta p = \frac{RT\rho}{M} \ln \frac{p}{p_0} \qquad (3-3)$$

From Equation (3-3), it can be observed that capillary tension increases as relative humidity decreases. This mechanism is considered to act in the medium-to-high humidity range[10].

At a given humidity, the thickness of the adsorption water layer is determined by the surrounding vapor pressure. However, when the distance between particles is relatively small, the thickness of the adsorption water layer may be determined by this distance rather than the surrounding humidity. In such regions where adsorption is hindered, disjoining pressure (swelling pressure) acts, separating the gel particles. The disjoining pressure mechanism posits that during drying, part of this pressure is released, leading to a reduction in the distance between gel particles and causing shrinkage. Powers[11] proposed a model shown in **Figure 3-3** (a), suggesting that this mechanism can explain shrinkage across the entire humidity range.

The surface tension mechanism (surface energy change mechanism) posits that changes in the surface tension of gel particles due to the desorption of adsorption water induce volumetric changes. Water adsorbed on the surface of gel particles is considered part of the solid's surface layer, relaxing the surface tension of the solid. As relative humidity decreases, adsorption water is lost, surface tension increases, and compressive stress is generated within the solid particles, leading to shrinkage (**Figure**

3-3 (b))[12]. The amount of water molecules adsorbed on the pore walls can be expressed, for example, by Equation (3-4) (BET Equation), where higher relative humidity leads to greater adsorption[10].

$$n = \frac{n^{\infty} K \frac{p}{p_0}}{\left(1 - \frac{p}{p_0}\right)\left\{1 + (K-1)\frac{p}{p_0}\right\}} \qquad (3-4)$$

Where:

n: Amount of adsorption (m^3/kg)

n^{∞}: Saturation adsorption amount for a monolayer (m^3/kg)

p: Vapor pressure (N/m^2)

p_0: Saturation vapor pressure (N/m^2)

K: Equilibrium constant

In high-humidity ranges, variations in the amount of capillary water evaporating do not influence surface tension, and this mechanism is considered effective at relative humidity levels below 40%[13].

The intracrystallite water migration mechanism postulates that the ingress and egress of water in calcium silicate hydrate (C-S-H) influence the interlayer spacing, resulting in volumetric changes. Feldman et al.[14, 15] indicated that the movement of intracrystallite water is reversible, as shown in **Figure 3-4** (a). Conversely, Ishai[16] argued that intracrystallite water is irreversible and that the volume change resulting from this mechanism only results in shrinkage. Alizadeh[17] reported that as water dissipates during drying, the silica framework of the C-S-H forms interlayer cross-links (either Si-O-Si or Si-O-Ca-O-Si bonds), leading to layer-to-layer bonding, as illustrated in **Figure 3-4** (b). Uchikawa et al.[18] explained that this mechanism occurs in extremely low-humidity conditions.

At present, no unified theory sufficiently explains the shrinkage behavior of cement-based materials, including their irreversible characteristics, across all humidity ranges. Generally, multiple mechanisms are thought to coexist, with capillary tension and disjoining pressure mechanisms prevailing in medium-to-high humidity ranges and surface tension and intracrystallite water migration mechanisms being dominant in low-humidity conditions.

In contrast to drying shrinkage, autogenous shrinkage is a macroscopic volumetric reduction caused by cement hydration, excluding volumetric changes due to water ingress or egress, temperature fluctuations, external forces, or external constraints. Autogenous shrinkage becomes more pronounced as the water-to-binder ratio decreases and the microstructure of the hardened material becomes denser[19]. In some cases, autogenous shrinkage alone can result in cracking[20].

Autogenous shrinkage is triggered by hydration shrinkage. Hydration shrinkage refers to the reduction in absolute volume during hydration caused by the solid-phase volume of the hydration

products being smaller than the combined volumes of unhydrated cement and water. Once the skeletal structure of the hardened cement paste is formed after setting, hydration shrinkage is offset by an increase in internal pores. Therefore, in the absence of an external water supply, or if the rate of water ingress cannot match the rate of pore formation even with a water supply, pores become unsaturated, creating a type of drying condition. This process generates capillary tension, leading to shrinkage via a mechanism similar to the capillary tension mechanism of drying shrinkage[21].

Drying shrinkage and autogenous shrinkage occur within the cement paste, while the aggregate constrains the shrinkage of the cement paste and mitigates the overall shrinkage of the concrete. Thus, the greater the aggregate content and the higher its elastic modulus, the smaller the shrinkage of the concrete. In terms of mix proportion, the unit water content, which correlates with aggregate content, is commonly used as an indicator of shrinkage. Concrete shrinkage is also influenced by numerous factors, such as the temperature and humidity around the structure, the shape and size of the member cross-section, the type of cement and admixtures, concrete compaction, and curing conditions. Autogenous shrinkage, in particular, is known to vary significantly depending on the type of cement. Among the mineral components of cement, the reactions of C_3A (aluminate phase) and C_4AF (ferrite phase) are significantly related to autogenous shrinkage, with higher contents of these phases resulting in greater autogenous shrinkage[22].

Numerous prediction equations and methods have been proposed for forecasting concrete shrinkage strain. In the Standard Specifications for Concrete Structures -2022 [Design Chapter], the shrinkage strain prediction formula for concrete in structural members is provided as Equation (3-5)[23].

$$\varepsilon'_{ds}(t,t_0) = \frac{\frac{1-RH/100}{1-60/100}\cdot \varepsilon'_{sh,inf}\cdot(t-t_0)}{\left(\frac{d}{100}\right)^2\cdot\beta+(t-t_0)} \quad (3-5)$$

$$d = \frac{4V}{S} \quad (3-6)$$

$$\varepsilon'_{ds}(t,7) = \frac{\varepsilon'_{sh,inf}\cdot(t-7)}{\beta+(t-7)} \quad (3-7)$$

$$\varepsilon'_{sh,inf} = \left(1+\frac{\beta}{182}\right)\cdot\varepsilon'_{sh} \quad (3-8)$$

$$\beta = \frac{30}{\rho}\left(\frac{120}{-14+21\cdot C/W}-0.70\right) \quad (3-9)$$

$$\varepsilon'_{sh} = 2.4\left(W+\frac{45}{-20+30\cdot C/W}\cdot\alpha\cdot\Delta\omega\right) \quad (3-10)$$

$$\Delta\omega = \frac{\omega_S}{100 + \omega_S} S + \frac{\omega_G}{100 + \omega_G} G \qquad (3-11)$$

Where:

$\varepsilon'_{ds}(t, t_0)$: Drying shrinkage strain of the member ($\times 10^{-6}$)

t, t_0: Age of concrete and age at the start of drying (days) ($t_0 > 3$ days)

RH: Average relative humidity of the environment where the structure is placed (%)

d: Effective thickness of the member (mm). For bar members with all surfaces exposed to drying, it can be the side length. For general cross-sections, it can be calculated using Equation (3-6).

V/S: Volume-to-surface area ratio (mm). The surface area includes only the portions exposed to external air.

$\varepsilon'_{sh,inf}$: Ultimate value of drying shrinkage strain ($\times 10^{-6}$)

β: Coefficient representing the time-dependent change in drying shrinkage strain

ε'_{sh}: Estimated value of test shrinkage ($\times 10^{-6}$)

ρ: Unit volume mass of concrete (g/cm^3)

C/W: Cement-to-water ratio

W: Unit water volume of concrete (kg/m^3) ($W \leq 175\text{kg/m}^3$)

α: Coefficient representing the influence of aggregate quality ($\alpha = 4\sim6$). For standard aggregates, $\alpha = 4$ may be used.

$\Delta\omega$: Water content in the aggregate

ω_S: Absorption rate of fine aggregate (%)

S: Unit weight of fine aggregate (kg/m^3)

ω_G: Absorption rate of coarse aggregate (%)

G: Unit weight of coarse aggregate (kg/m^3)

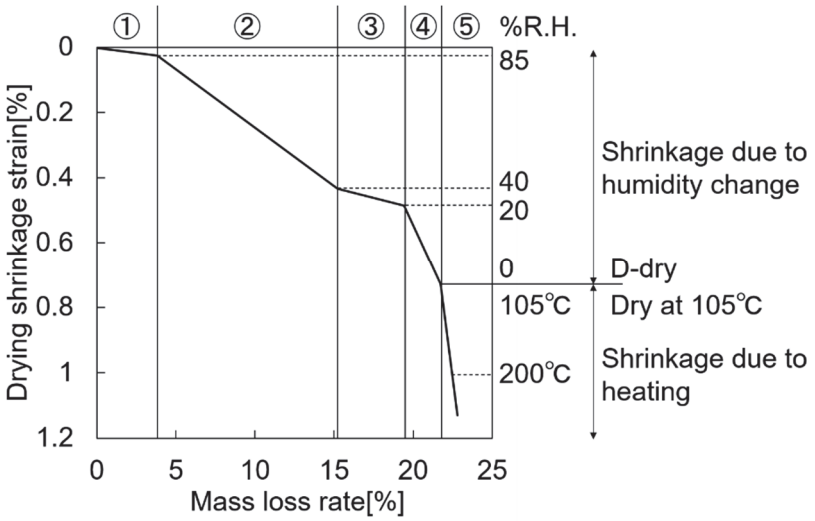

Figure 3-1 Relation between the drying shrinkage strain and the mass loss rate[9]

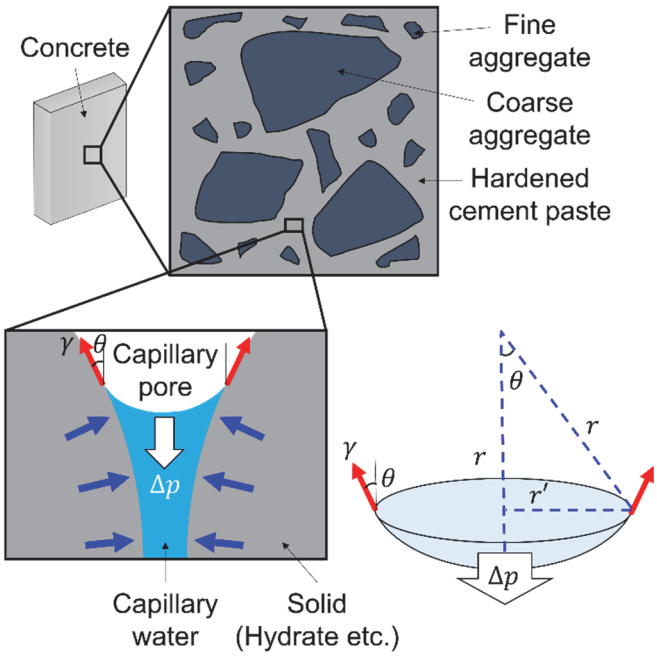

Figure 3-2 Schematic diagram of capillary tension model[10]

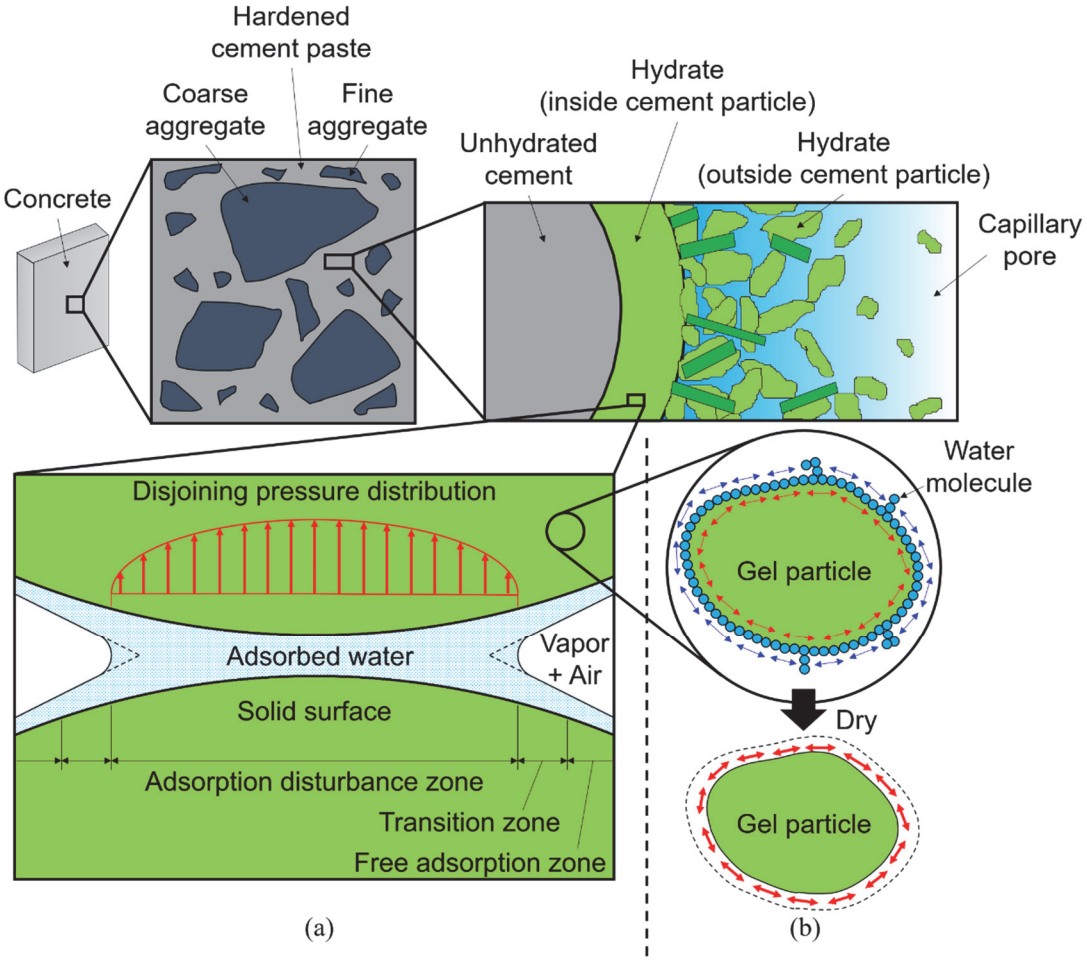

Figure 3-3 Schematic diagram of (a) disjoining pressure model[11] and (b) surface tension mechanism[12]

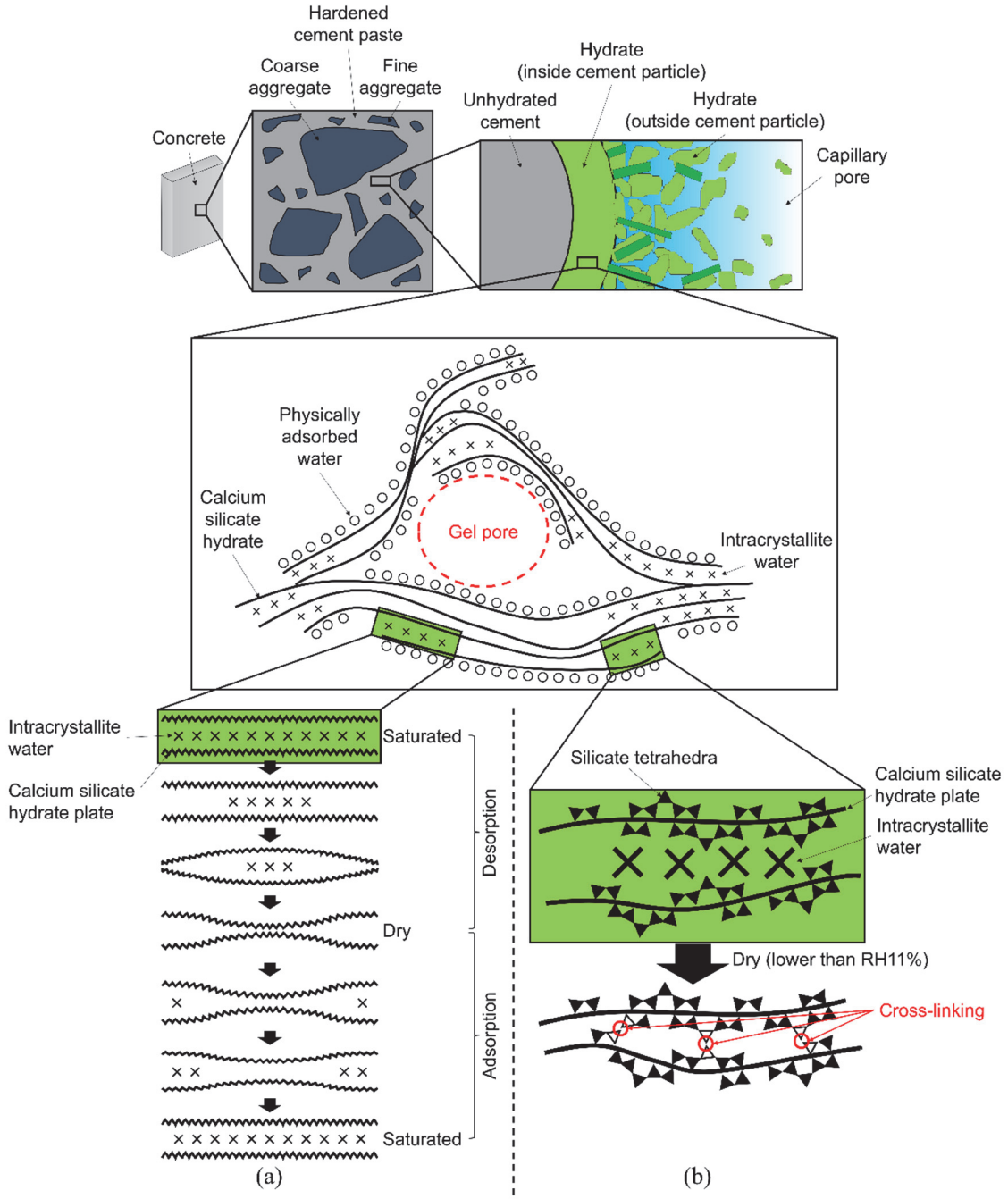

Figure 3-4 Schematic diagram of (a) the exit and entry of intracrystallite water[14, 15], and (b) the nanostructural changes occurring on the removal of intracrystallite water in C-S-H[16]

3.2.3. Creep mechanism of cement concrete

Creep refers to the phenomenon where deformation increases over time under sustained load. When stress exceeds approximately 70–90% of the material's strength, strain due to creep continues to increase, ultimately leading to failure. This type of failure is referred to as creep rupture, and the

maximum stress level below which no rupture occurs is called the creep limit. Depending on the stress state, creep can be categorized into compressive creep, tensile creep, and bond creep; however, compressive creep is generally referred to simply as "creep." In structural applications, creep is considered in contexts such as the effective stress in prestressed concrete beams, the long-term deflection of reinforced concrete beams, and the vertical shortening of high-rise buildings.

Numerous hypotheses have been proposed regarding the internal mechanisms of creep, but no single theory fully explains the phenomenon. Representative theories include the delayed elasticity theory, which suggests that stress distribution gradually shifts from viscous fluids bearing the load in the initial stages to the cement skeleton over time, leading to slow additional elastic deformation and resulting in creep (**Figure 3-5**). Another is the seepage theory, which attributes creep deformation to the movement of water under external pressure, escaping from pores and eventually evaporating (**Figure 3-6**). Additionally, some theories propose that creep deformation arises from microcracks or plastic deformation due to slippage in weak zones, such as the interfacial transition zones (ITZ) between aggregates and hardened cement paste (**Figure 3-7**).

Regarding the prediction of creep strain in concrete, numerous prediction equations and methods have been proposed alongside those for shrinkage strain. The Standard Specifications for Concrete Structures -2022 [Design Chapter] provides a prediction equation for creep strain per unit stress in concrete members, as shown in Equation (3-12)[23].

$$\varepsilon'_{cc}(t,t')/\sigma'_{cp} = \frac{4W(1-RH/100)+350}{12+f'_c(t')} \cdot \log_e(t-t'+1) \qquad (3-12)$$

$$t \text{ and } t' = \sum_{i=1}^{n} \Delta t_i \cdot exp\left[13.65 - \frac{4000}{273+T(\Delta t_i)/T_0}\right] \qquad (3-13)$$

$$f'_c(t') = \frac{1.11t'}{4.5+0.95t'}(-20+30\,C/W) \qquad (3-14)$$

Where:

$\varepsilon'_{cc}(t,t')/\sigma'_{cp}$: Creep strain per unit stress of concrete loaded at age t' (days), evaluated at age t (days) ($\times 10^{-6}/(\mathrm{N/mm^2})$)

W: Unit water volume of the concrete (kg/m^3) ($W \leq 175$ kg/m^3)

RH: Relative humidity (%) ($45\% \leq RH$)

t' and t: Effective ages of concrete at the time of loading and during loading (days), corrected using Equation (3-13) ($t' \geq 7$ days)

Δt_i: Number of days during which the temperature is T (°C)

T_0: 1 °C

$f'_c(t')$: Compressive strength of the concrete at effective age t' (days) at the time of loading

(N/mm^2). If measured values are unavailable, Equation (3-14) may be used.

C/W: Cement-to-water ratio

Additionally, the creep coefficient prediction equation is provided in Equation (3-15)(49)

$$\phi(t,t') = \frac{4W(1 - RH/100) + 350}{12 + f'_c(t')} \cdot \log_e(t - t' + 1) \cdot E_{ct} \qquad (3-15)$$

where:

$\phi(t,t')$: Creep coefficient for concrete loaded at age t' (days), evaluated at age t (days)

E_{ct}: Young's modulus of concrete at effective age t' (days) at the time of loading

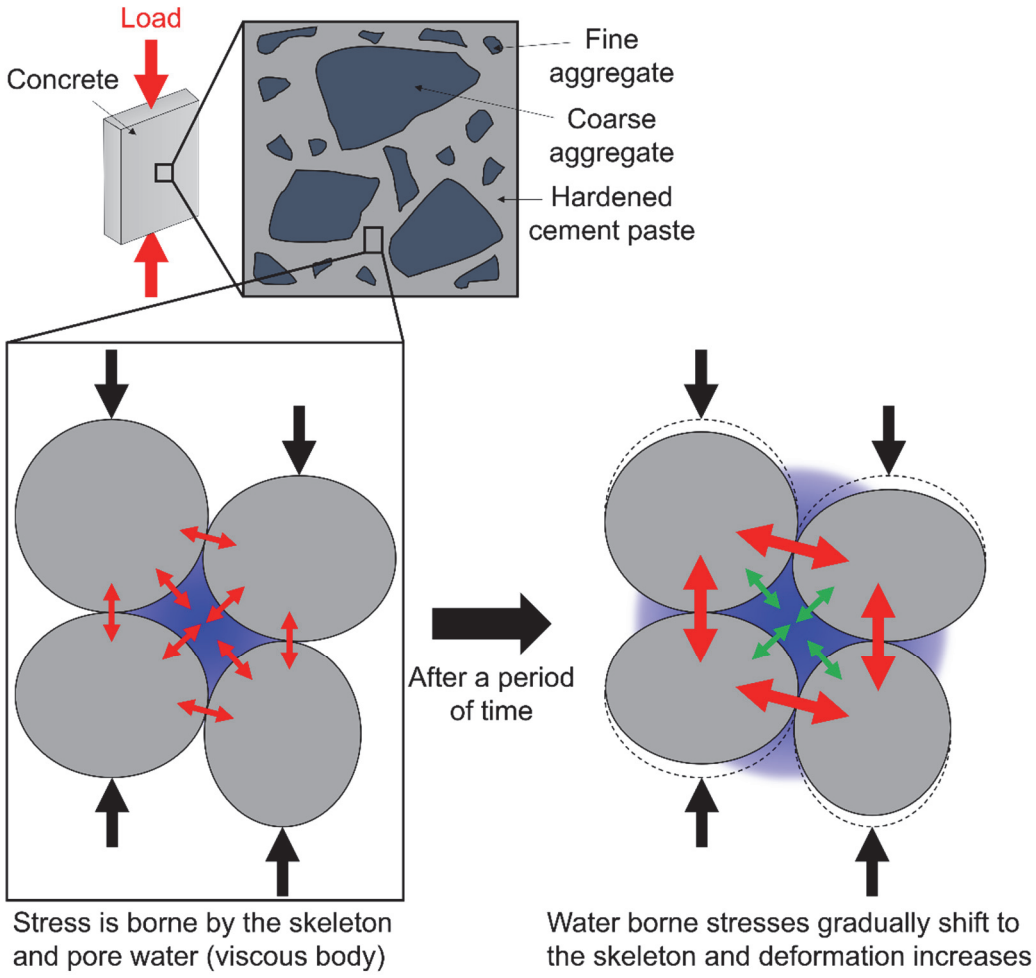

Figure 3-5 Schematic diagram of the theory of delayed elasticity

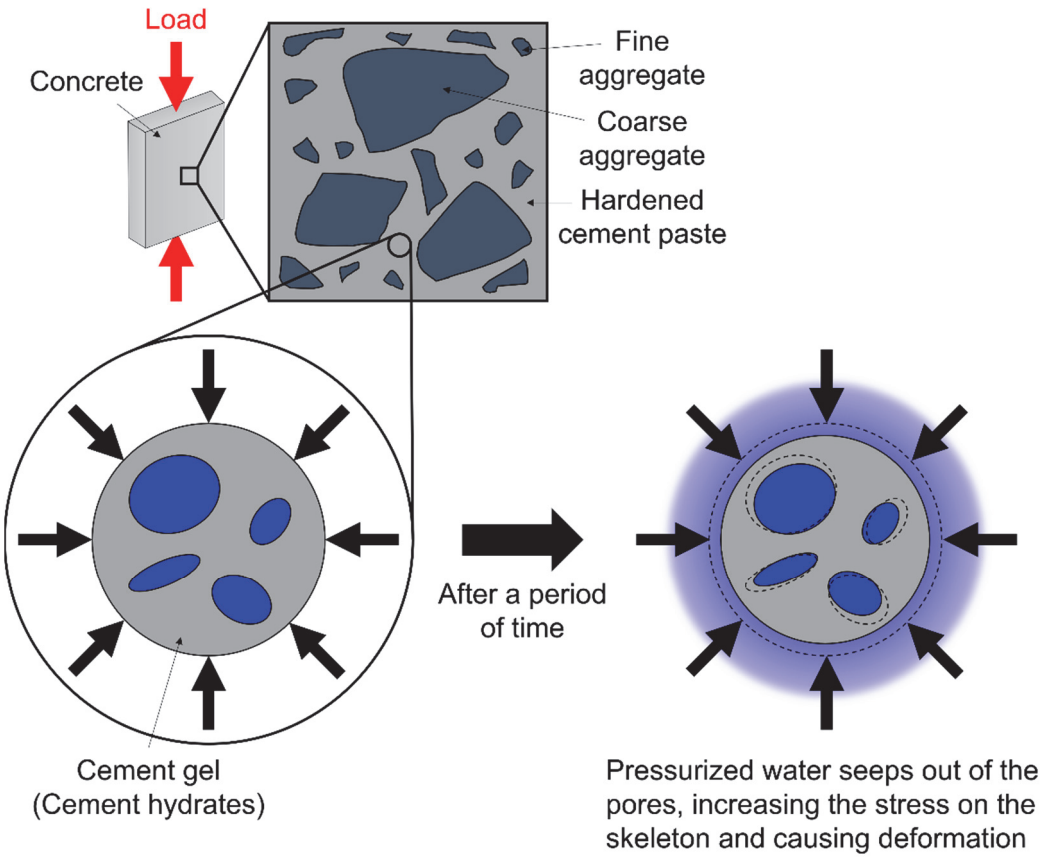

Figure 3-6 Schematic diagram of the seepage theory

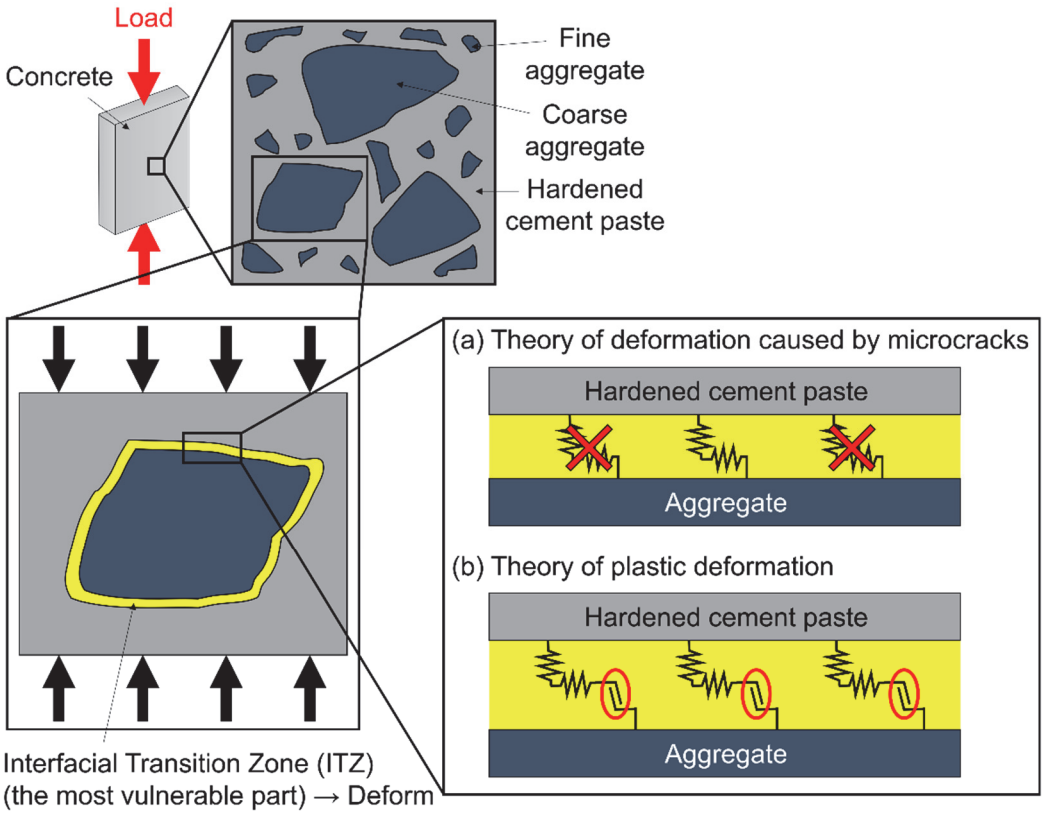

Figure 3-7 Schematic diagram of the theory of interfacial transition zone (ITZ) deformation

3.2.4. Research trends on the shrinkage and creep of geopolymer

Geopolymer (GP) solidify through dehydration and polycondensation reactions, resulting in an internal structure completely different from cementitious materials. Additionally, the variety of manufacturing conditions complicates the systematic understanding of their shrinkage and creep characteristics, as well as the underlying mechanisms[24]. Factors influencing these properties include the type of reactive filler or alkali-silicate solution, the solution-to-powder ratio, curing temperature, and calcium content[25-27]. Representative studies are summarized below. Homma[28] investigated the length changes and drying shrinkage of geopolymer mortar made with Class II fly ash and a geopolymer solution, cured at 80°C. During the heating phase (from room temperature to 80°C), expansion occurred, but shrinkage was observed during the constant-temperature phase. After cooling, the specimen almost returned to its original length. Regarding drying shrinkage, shorter curing times resulted in greater length changes, and the shrinkage characteristics varied depending on the type of alkali used. Ichimiya et al.[29] measured the length changes of geopolymer mortar made with various types of fly ash (Class I, II, and IV) and ground granulated blast furnace slag (GGBFS), cured at 60°C, and compared them with cement mortar. At 4 weeks of age, shrinkage strain in geopolymer mortar varied with fly ash type; Class IV fly ash showed approximately five times the shrinkage of Class I

fly ash and 1.7 times that of cement mortar. Although trends in mass loss rates were similar to shrinkage strain, some combinations (e.g., Class I fly ash) exhibited small shrinkage strain despite significant mass loss. Uehara et al.[30] partially replaced fly ash with GGBFS in geopolymer concrete cured at 80°C and examined its length and mass changes. The length change ranged between 250-550 μ, with higher alkali-to-water molar ratios resulting in smaller length changes under the same GGBFS replacement ratio. However, no clear trend between GGBFS replacement ratios and length changes was identified. Similar results have been reported in other studies[29, 31, 32], indicating that geopolymer concrete made with only fly ash tends to exhibit smaller length changes and larger mass loss rates, possibly due to the presence of large internal pores that allow significant water loss while reducing capillary shrinkage. For repair applications, geopolymers are typically cured at ambient temperature. However, fly ash alone is insufficient for rapid strength development, necessitating the use of GGBFS. Under such conditions, drying shrinkage and early-age cracking have been noted as significant concerns[33-36]. Okada et al.[37] replaced 30% of the binder with GGBFS and added 3% shrinkage-reducing agents (SRA) based on polyether derivatives to geopolymer concrete. They observed that the shrinkage strain was reduced from approximately -1000×10^{-6} (without SRA) to -200×10^{-6} with SRA, significantly mitigating drying shrinkage. While these studies primarily focus on non-ambient curing conditions, expansion agents have also been employed to enhance shrinkage resistance. Nakamura et al.[38] used ettringite-lime composite and calcium sulfoaluminate-based expansion agents in geopolymer mortar with 30% GGBFS replacement, cured at 60°C. Early-age expansion comparable to that of cement mortar was achieved, with greater expansion observed at higher additive dosages. However, ettringite-lime composites exhibited significant early-age expansion, followed by notable shrinkage. Other investigations have explored shrinkage in fiber-reinforced and recycled aggregate-based geopolymers[39, 40].

Wallah and Rangan[41-43] studied geopolymer concrete made with Class F fly ash as a reactive filler and sodium hydroxide and sodium silicate as alkali-silicate solutions. Applying 40% of the compressive strength as sustained stress over approximately one year, they reported extremely low creep. The specific creep ranged from $15\text{-}29\times10^{-6}$/MPa for specimens with compressive strengths of 67-40 MPa. The creep coefficient was 0.6-0.7 for specimens with compressive strengths of 40-57 MPa and 0.4-0.5 for those with 67 MPa, approximately half of the predicted values by Australian Standard AS 3600. Sagoe-Crentsil et al.[44] reported that geopolymer concrete with 40 MPa compressive strength exhibited creep coefficients 40-60% lower than ordinary Portland cement (OPC) concrete of equivalent strength. Although the mechanism remains unclear, they suggested that unreacted fly ash particles may act as micro-aggregates, contributing to creep reduction through a restraining effect. Castel et al.[45] investigated geopolymer mortar made with Class F fly ash, Kaolite high-performance ash, and GGBFS as reactive fillers, using sodium hydroxide (12M) and sodium silicate as alkali solutions. When 40% of the compressive strength was applied at 8 days of age, creep coefficients were

initially consistent with Eurocode 2 predictions but became smaller after 50 days. Geopolymer mortars cured at 80°C for 7 days exhibited negligible creep with coefficients of approximately 0.2, highlighting the need for further research as excessively low creep could induce stress concentration issues. Gunasekera et al.[46] investigated long-term creep and drying shrinkage in three geopolymer concretes made entirely of Class F fly ash. While concretes with fly ash from Gladstone and Pt. Augusta exhibited creep strains comparable to OPC concrete (700-800 μ), Tarong fly ash exhibited significantly higher creep (1900 μ), attributed to macropores ranging from 50 nm to 1 μm. Un et al.[47] studied the long-term behavior of geopolymer beams under sustained loads. Sustained loads were applied at 14 and 28 days of age, and creep tests were conducted using cylinder specimens. They reported that while geopolymer concrete exhibited sufficient structural strength, both compressive and flexural tensile strengths were affected by drying, with microcracks forming on drying surfaces. Nan et al.[48] reported that geopolymer concrete with 70 N/mm^2 compressive strength, made with Class I fly ash, GGBFS, and potassium silicate and hydroxide, exhibited a creep coefficient of 0.44 at 410 days of loading. The basic creep coefficient was 0.39, comparable to or smaller than high-strength concrete.

3.3. Shrinkage and creep test of geopolymer

To elucidate the time-dependent deformation characteristics of low water-to-powder ratio (W/P) geopolymer (GP) that are expected to enhance the radio wave transparency of concrete, and to systematize the time-dependent deformation characteristics of GP concrete while identifying influential factors, compression creep tests were conducted on various GP concretes, including low W/P GP. While most studies on GP concrete have utilized a mixture of fly ash (FA) and ground granulated blast furnace slag (GGBFS) as reactive fillers, this study exclusively used FA as the reactive filler to verify the properties of pure GP without calcium-derived hydrates in the solidified matrix.

3.3.1. Specimen overview

The test specimens were rectangular prisms (100 mm in width and depth, 400 mm in height), simulating structural members. To measure strain and temperature inside the specimens, a self-temperature-compensating strain gauge (KM-100BT, Tokyo Measuring Instruments Laboratory) was embedded at the center of each specimen. As shown in **Table 3-1**, five levels of test conditions were set, with two specimens prepared for each condition. The materials used for each condition are listed in **Table 3-2** and **Table 3-3**, and the mix proportions are shown in **Table 3-4**.

The "Normal" condition followed the mix and curing conditions specified by the Geopolymer Technology Research Subcommittee (361 Committee) of the Concrete Committee of the Japan Society of Civil Engineers[24]. The "Normal (Room Temp)" condition utilized the same mix proportions as "Normal" but was cured at room temperature, unlike the other conditions, which were subjected to

60°C sealed curing. The "Si Rich" condition increased the Si content by reducing the alkali concentration while maintaining the solution-to-powder ratio and unit water content as in "Normal." The "Low Water" condition reduced the solution-to-powder ratio while keeping the alkali solution composition identical to "Normal." Lastly, the "W/P17% (Paste)" condition, consistent with the investigations in CHAPTER 2, utilized an extremely low W/P to minimize unit water content and excluded aggregates. While chemical admixtures were used in CHAPTER 2, subsequent evaluations revealed minimal improvement in flowability or filling performance, so admixtures were excluded in this study. For the "W/P17% (Paste)" condition, an additional unloaded specimen with embedded reinforcing bars ("Reinforced") was prepared for shrinkage strain measurement (**Figure 3-8**). To ensure sufficient flowability and filling around the reinforcement, W/P was slightly increased to 17%.

Table 3-1 Conditions of geopolymer specimens for the compression creep test

	Alkali/Water	Silica/Alkali	Liquid/Powder	Curing Temp.
Normal	0.125	0.700	0.90	60℃
Normal (Room Temp)				Room(≃20℃)
Si Rich	0.108	1.046		60℃
Low Water	0.125	0.700	0.70	
W/P17% (Paste)	0.365	0.332	0.45	

Table 3-2 Materials of geopolymer specimens for the compression creep test

Type	Name	Mark		Ingredients / Physical properties
Active Filler (P)	Fly ash	FA		JIS Type II Specific surface area: 3690 cm^2/g Specific gravity: 2.29 g/cm^3
Alkaline solution (L)	Sodium silicate solution	SS		Listed in **Table 3-3**
	Sodium hydroxide	SH		Granular, Purity: 98.0% or higher
	Water	LW		Deionized water
Fine aggregate	Crushed sand	S		Hard sandstone from Hachioji, Tokyo Surface dry density: 2.65 g/cm^3 Water absorption rate: 1.30%
Coarse aggregate	Crushed stone	G	Large	Hard sandstone from Ome, Tokyo Surface dry density: 2.66 g/cm^3 Water absorption rate: 0.81%
			Small	Hard sandstone from Ome, Tokyo Surface dry density: 2.66 g/cm^3 Water absorption rate: 0.81%

Table 3-3 Ingredients and physical properties of sodium silicate solution manufactured by FUJIFILM Wako Pure Chemical Corporation

Test case	Specified value
Iron (Fe)	～0.03%
Sodium oxide (Na_2O)	17.0～19.0%
Silicon dioxide (SiO_2)	35.0～38.0%
Molar concentration (SiO_2/Na_2O)	2.06～2.31
Concentration	52.0～57.0%

Table 3-4 Mix proportions of geopolymer specimens for the compression creep test (TW: Total water volume)

	Unit weight (kg/m^3)								
	P	L			S	G		Air	TW
	FA	SS	SH	LW		Large	Small		
Normal	592	156	18	132	607	372	372	0	195
Si Rich	592	202	0	114	607	372	372	0	170
Low Water	661	136	16	115	607	372	372	0	195
W/P17% (Paste)	1458	275	137	137	0	0	0	0	248

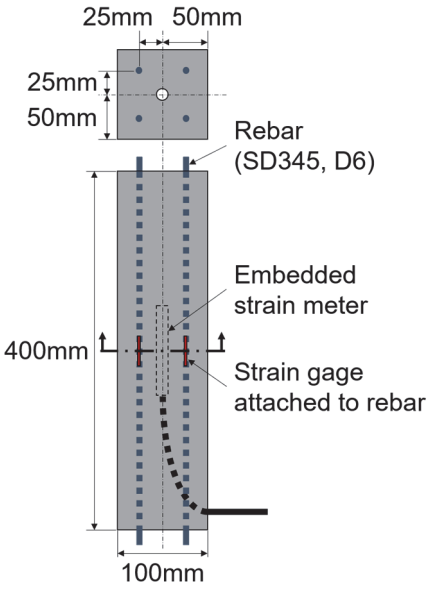

Figure 3-8 Schematic diagram of the reinforced WP17% (Paste) specimen

3.3.2. Preparation of specimens

The mixing and placement procedures differed between "W/P17% (Paste)" and other GP concretes.

For GP concretes, the alkali solution was prepared one day prior to mixing and stored at room temperature. Mixing was performed using a 100 L forced-mixing mixer. Reactive filler and fine aggregate were dry-mixed for 30 seconds, followed by the addition of the alkali solution and mixing for 60 seconds. After scraping down the sides of the mixer, coarse aggregate was added, and mixing continued for another 60 seconds. Immediately after mixing, placement into molds began, and slump flow tests (JIS A 1150) and air content tests (JIS A 1128) were conducted. Due to high flowability, the 500 mm flow time was recorded instead of the standard slump flow. The results of these tests are summarized in **Table 3-5**. While the designed air content was 0%, the measured air content was up to 4.0%, likely due to the high viscosity of the GP matrix and the entrapped air caused by viscous sodium

silicate solutions and the solution-to-powder ratio. Placement was conducted in two layers, with compaction performed using a formwork vibrator for each layer. **Figure 3-9** shows the placement immediately after the first layer.

For the "W/P17% (Paste)" condition, the alkali solution was prepared on the mixing day and maintained at 60°C in a constant-temperature and humidity chamber until use. Mixing was performed using a 30 L mortar mixer, with the reactive filler and alkali solution added sequentially. After low-speed mixing for 90 seconds, the sides of the mixer were scraped, followed by high-speed mixing for 60 seconds. Due to low flowability and rapid setting caused by the heat of the alkali solution, no tests for fresh-state properties or compaction were conducted. The paste was manually pressed into molds to ensure filling.

After placement, the specimen surfaces were wrapped and sealed with aluminum tape (**Figure 3-10**). Once all specimens were placed and sealed, except for "Normal (Room Temp)," they were transferred to a constant-temperature and humidity chamber. Strain gauges and strain sensors were connected to a data logger, and heating began. Specimens were cured at 60°C for 24 hours under sealed conditions, followed by cooling to 20°C and continued sealed curing for five days. After curing, specimens were disconnected from the data logger and removed from the chamber and demolded.

Table 3-5 Fresh properties of geopolymer concrete

	Time to reach 500mm flow (s)	Air volume (%)
Normal	7.08	1.9
Si Rich	22.82	2.5
Low Water	6.86	4.0

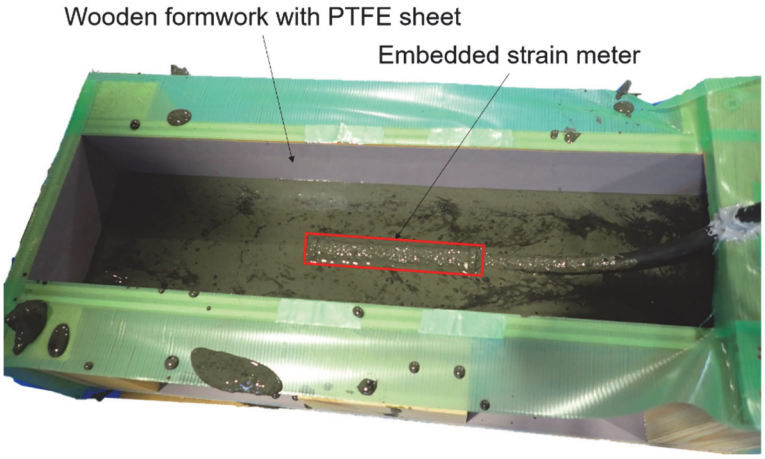

Figure 3-9 Specimen immediately after casting the first layer

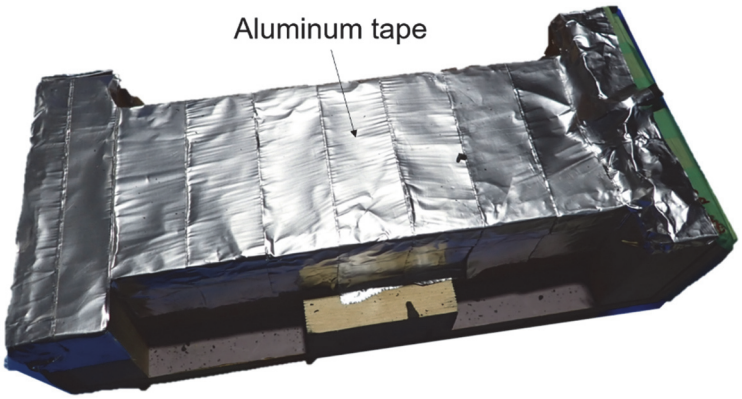

Figure 3-10 Specimen after sealing by aluminum tape

3.3.3. Compression creep test overview

After demolding the specimens, the strain gauges and strain sensors were immediately reconnected to the data logger, and the compression creep test was initiated in accordance with JIS A 1157. The testing facility was an indoor environment without temperature or humidity control.

For the loaded specimens, sustained loads were applied using the apparatus shown in **Figure 3-11**. The load was first applied using a hydraulic jack (**Figure 3-11** (a)), and once the designated load was reached, the upper nuts were tightened to maintain the load through the spring's restoring force (**Figure 3-11** (b)). The applied load was set at 30% of the compressive strength measured the day prior (**Figure 3-12**). However, for the "W/P17% (Paste)" condition, due to its high strength exceeding the spring's maximum deflection capacity, the maximum deflection load of the spring was used as the actual applied load. During the test, strain and temperature within the specimen were monitored, and strain gauges attached to the PC steel bars were used to confirm that the applied load was maintained without loss.

For the unloaded specimens used to measure shrinkage, the top and bottom surfaces were sealed with aluminum tape, and the specimens were placed adjacent to the loaded specimens (**Figure 3-13**). During the test, in addition to measuring strain and temperature within the specimens, periodic measurements of ambient temperature, humidity, and specimen weight were conducted. **Figure 3-14** shows the change in temperature and humidity.

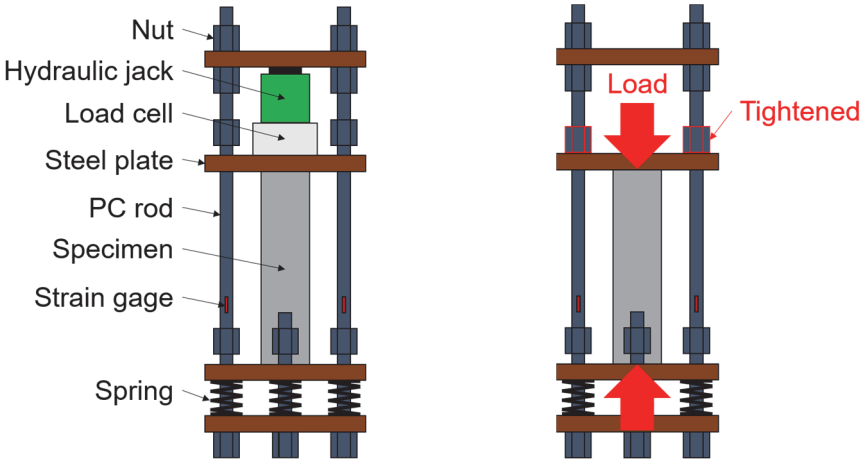

Figure 3-11 Schematic diagram of the testing equipment for compressive creep of geopolymer specimen (a)during loading, (b)during continuous loading

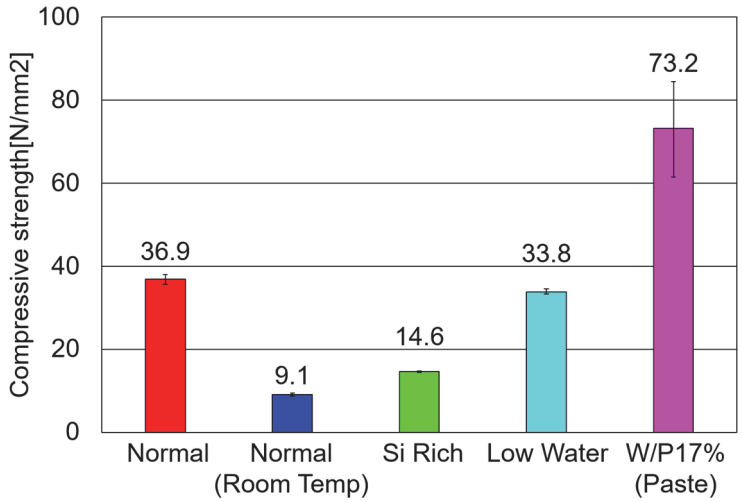

Figure 3-12 Compressive strength at 5 days of age

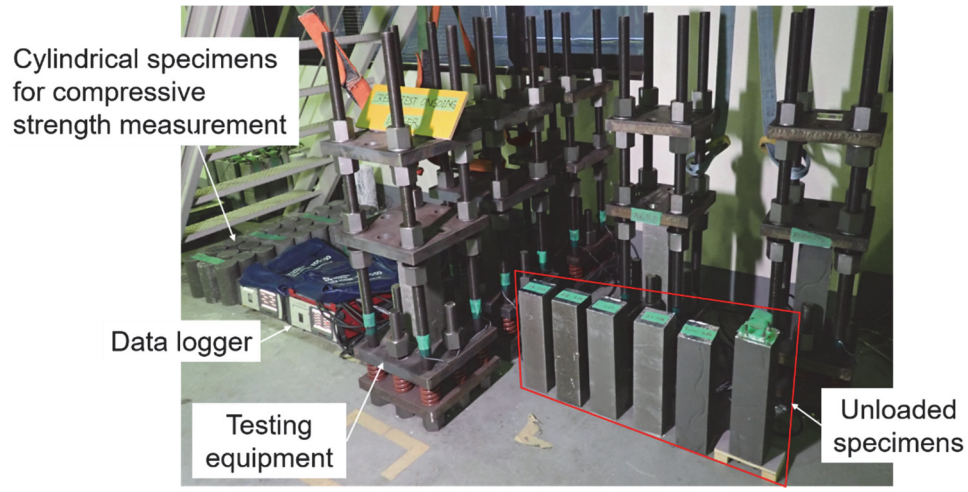

Figure 3-13 Overall view of the testing site

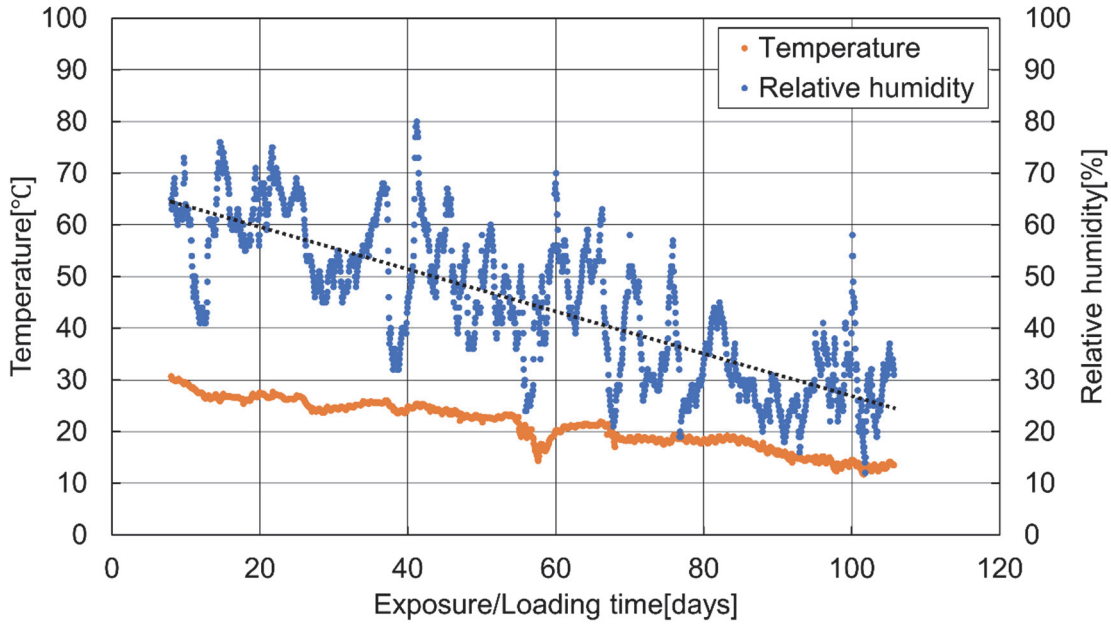

Figure 3-14 Change in ambient temperature and relative humidity

3.3.4. Compression test and MIP test overview

To investigate the influencing factors on time-dependent deformation properties, compressive strength and pore size distribution measurements were conducted. In accordance with JIS A 1108 and JIS A 1149, the compressive strength and static elastic modulus were measured at curing ages of 7, 28, and 91 days. Additionally, at curing ages of 28 and 91 days, the solidification reaction was terminated by acetone immersion, and the pore size distribution was measured using the mercury intrusion porosimetry (MIP) method. The measurement principles of the MIP method, as well as the

measurement procedure and conditions, are described below.

The mercury intrusion method is a technique used to measure the pore volume and pore size distribution of porous materials based on the volume of mercury intruded into the pores. Mercury has a high surface tension compared to most liquids and does not penetrate pores unless external pressure is applied. Additionally, it does not chemically react with porous materials such as cementitious hardened materials or silica-based materials. Assuming that the pores are cylindrical, the relationship between pore diameter D and applied pressure P can be expressed by the Washburn equation, as given in Equation (3-16):

$$D = -\frac{4\gamma_m \cos\theta}{P} \qquad (3-16)$$

Where:

D: Pore diameter (m)

γ_m: Surface tension of mercury (N/m), approximately $\gamma_m \approx 0.485\ \mathrm{N/m}$

θ_m Contact angle of mercury with the solid surface (deg), approximately$\theta_m \approx 140°$

P: Applied pressure (Pa)

This equation indicates that pore diameter D is inversely proportional to applied pressure P. Based on Equation (3-16), by measuring the volume of mercury intruded into the sample at incrementally increasing pressures, it is possible to quantify the distribution of different pore sizes. Typically, mercury intrudes into larger pores at low pressures and progressively enters smaller pores as the pressure increases.

Prior to measurement, cylindrical specimens were crushed into fragments approximately 2.5–5 mm in size. These fragments were immersed in acetone for 24 hours to halt the progression of solidification reactions. To facilitate acetone penetration, a water-flow pump was used to degas the samples. Acetone immersion is a commonly used technique to suppress cement hydration reactions by removing pore water, thereby ceasing further hydration. However, since geopolymer solidification does not involve hydration, it remains unclear whether water removal effectively inhibits the solidification reaction. Nevertheless, in the early stages of geopolymerization, dissolution of raw materials such as fly ash is necessary, and this process occurs only in the presence of water. Therefore, in this study, it was assumed that removing water from the geopolymer would inhibit the dissolution of raw materials, thereby preventing further geopolymerization. Based on this assumption, acetone immersion was adopted as the method to halt the solidification reaction. Following acetone immersion, the samples were subjected to ultrasonic cleaning for 15 minutes, after which the acetone was replaced, and ultrasonic cleaning was performed again. After washing, the samples were removed from the

acetone and degassed using a water-flow pump. Finally, the samples were dried in an oven at 40°C for more than 24 hours.

For measurements, PoreMaster 60GT (Anton Paar, Austria) was used. The technical specifications are summarized in **Table 3-7**. The measurement process involved placing the sample into a sealed measurement cell and recording its weight. Subsequently, the cell was inserted into the low-pressure station for measurement under low pressure. After completing the low-pressure measurement, the cell was transferred to the high-pressure station for measurement under high pressure. Using the measurement data, including the sample density, cumulative pore volume per unit volume (cc/cc) and pore volume per unit volume (cc/cc) were calculated.

Table 3-6 Technical specifications of MIP used (PoreMaster 60GT)

Low-pressure stations	2
(low-pressure range – psi)	(0.2 to 50)
(low-pressure pore size range – microns)	(1,100 to 4)
Cold trap	Yes
High-pressure stations	2
(high-pressure range – psi)	(20 to 60,000)
(high-pressure pore size range – microns)	(10 to 0.0036)
Automatic air purge system	Yes
High-pressure port open assist	Yes
Mid-range pressure transducer	Included
Transducer accuracy	Better than +/-0.11 % fso
Volume accuracy	Better than +/-1 % of sample stem volume
Volume resolution	Better than +/-0.0001 cm^3

3.4. Results

3.4.1. Shrinkage behavior

The time-dependent changes in internal strain, specifically the drying shrinkage strain, of the unloaded specimens, including those with reinforcing bars, after exposure are shown in **Figure 3-15**. The strains presented here have been corrected to remove thermal strain according to Equation (3-17), assuming a thermal expansion coefficient of $10 \times 10^{-6}/℃$, consistent with typical concrete values[23, 49]. It should be noted that while a systematic review of the thermal expansion coefficient of GP concrete has not been conducted, values comparable to those of conventional cement concrete have been observed in previous studies[50, 51].

$$\varepsilon = C_\varepsilon \varepsilon_i + (11.7 - \gamma) \cdot \Delta t - C_\beta \chi \qquad (3-17)$$

$$\chi = \varepsilon_{(t_2)} - \varepsilon_{(t_1)} \quad (3-18)$$

$$\varepsilon(t_i) = at_i^3 + bt_i^2 + ct_i + d \quad (3-19)$$

Where:

ε: Strain with thermal strain removed ($\times 10^{-6}$)

C_ε: Calibration coefficient ($\times 10^{-6}/1 \times 10^{-6}$)

ε_i: Change in indicated value from the initial reading (gauge factor $K = 2.00$) ($\times 10^{-6}$)

γ: Thermal expansion coefficient of the specimen ($\times 10^{-6}/℃$), assumed to be $10 \times 10^{-6}/℃$

Δt: Temperature difference (℃)

χ: Zero-point drift of the strain gauge (gauge factor $K = 2.00$) ($\times 10^{-6}$)

11.7: Thermal expansion coefficient of the calibration jig used for measuring zero-point drift ($\times 10^{-6}/℃$)

C_β: Correction coefficient ($\times 10^{-6}/℃$)

a, b, c, d: Coefficients derived from zero-point drift measurement data of the strain gauge

t_1: Actual temperature at the time of initial reading (℃)

t_2: Actual temperature at the time of measurement (℃)

Additionally, the time-dependent changes in shrinkage strain of general cement concrete were estimated using the shrinkage strain prediction equation presented in the 2022 Concrete Standard Specification [Design Edition] (Equation (3-5), reproduced), labeled as "Cement" in the figure. The cement concrete mix assumed a typical C/W ratio of 2.0, with aggregate quantity and properties consistent with GP concrete.

$$\varepsilon'_{ds}(t, t_0) = \frac{\frac{1 - RH/100}{1 - 60/100} \cdot \varepsilon'_{sh,inf} \cdot (t - t_0)}{\left(\frac{d}{100}\right)^2 \cdot \beta + (t - t_0)} \quad (3-5, \text{Reproduced})$$

$$d = \frac{4V}{S} \quad (3-6, \text{Reproduced})$$

$$\varepsilon'_{ds}(t, 7) = \frac{\varepsilon'_{sh,inf} \cdot (t - 7)}{\beta + (t - 7)} \quad (3-7, \text{Reproduced})$$

$$\varepsilon'_{sh,inf} = \left(1 + \frac{\beta}{182}\right) \cdot \varepsilon'_{sh} \quad (3-8, \text{Reproduced})$$

$$\beta = \frac{30}{\rho}\left(\frac{120}{-14 + 21 \cdot C/W} - 0.70\right) \quad (3-9, \text{Reproduced})$$

$$\varepsilon'_{sh} = 2.4\left(W + \frac{45}{-20 + 30 \cdot C/W} \cdot \alpha \cdot \Delta\omega\right) \qquad (3-10, \text{Reproduced})$$

$$\Delta\omega = \frac{\omega_S}{100 + \omega_S} S + \frac{\omega_G}{100 + \omega_G} G \qquad (3-11, \text{Reproduced})$$

Where:

$\varepsilon'_{ds}(t, t_0)$: Drying shrinkage strain of the specimen ($\times 10^{-6}$)

t, t_0: Concrete age and age at the start of drying (days) ($t_0 > 3$ days)

RH: Average relative humidity of the environment where the specimen is placed (%), assumed as the average relative humidity during the measurement period ($RH = 44.5\%$).

d: Effective member thickness (mm), set as $d = 100\text{mm}$ here.

V/S: Volume-to-surface area ratio (mm)

$\varepsilon'_{sh,inf}$: Final value of drying shrinkage strain ($\times 10^{-6}$)

β: Coefficient representing the time-dependent changes in drying shrinkage strain

ε'_{sh}: Estimated test value of shrinkage strain ($\times 10^{-6}$)

ρ: Unit volume mass of concrete (g/cm^3), assumed as $\rho = 2.10\text{g/cm}^3$ based on the mix proportion.

C/W: Cement-to-water ratio, assumed as $C/W = 2.0$.

W: Unit water content of concrete (kg/m^3), assumed as $W = 165\text{kg/m}^3$.

α: Coefficient representing the quality of the aggregate ($\alpha = 4$~6), assumed as $\alpha = 4$.

$\Delta\omega$: Water content in the aggregate

ω_S: Water absorption rate of fine aggregate (%), assumed as $\omega_S = 1.30\%$.

S: Unit weight of fine aggregate (kg/m^3), assumed as $S = 607\text{kg/m}^3$.

ω_G: Water absorption rate of coarse aggregate (%), assumed as $\omega_G = 0.81\%$.

G: Unit weight of coarse aggregate (kg/m^3), assumed as $G = 744\text{kg/m}^3$.

From **Figure 3-15**, it is evident that the magnitude of drying shrinkage strain in geopolymer (GP) varies significantly depending on its mix proportions and curing conditions. However, the drying shrinkage behavior of GP exhibits a distinct characteristic compared to that of "Cement," i.e., conventional cement concrete: a substantial shrinkage occurs immediately after exposure, followed by a gradual progression of shrinkage over time.

Focusing on GP concrete, the drying shrinkage strain in all cases is larger than that of "Cement," suggesting that GP concrete exhibits greater drying shrinkage compared to conventional cement concrete. The drying shrinkage strain of "Normal" is approximately 1.5 times larger than that of "Cement." The drying shrinkage strain of "Normal (Room Temp)" is more than twice that of "Normal" and nearly four times that of "Cement," indicating that the absence of heat curing leads to significantly

increased drying shrinkage. The drying shrinkage strain of "Si Rich," while not as pronounced as that of "Normal (Room Temp)," is still greater than that of "Normal" and "Cement," suggesting that increasing the Si/A ratio results in higher drying shrinkage. The drying shrinkage strain of "Low Water" is slightly smaller than, but largely follows the same trend as, "Normal," indicating that reducing the water-to-solids ratio (L/P) and unit water content has little effect on drying shrinkage behavior. In contrast, the drying shrinkage strain of "W/P17% (Paste)," which does not include aggregates, is smaller than that of other GP concretes and comparable to "Cement." Generally, in the absence of aggregates, drying shrinkage is larger than in the presence of aggregates. Thus, the drying shrinkage strain of binder-only materials is expected to exceed that of "Cement." Consequently, when comparing binder-only materials, GP with a low W/P ratio exhibits smaller drying shrinkage than the hardened cement paste in conventional cement concrete. Therefore, it is anticipated that GP with a significantly reduced W/P ratio, which minimizes unit water content, can reduce the drying shrinkage of concrete when used as a binder. However, approximately 70 days after exposure, the drying shrinkage strain of "W/P17% (Paste)" appears to accelerate, requiring careful monitoring in the future. In the case of "Reinforced," which incorporates reinforcement into "W/P17% (Paste)," the drying shrinkage strain is slightly smaller than that of "W/P17% (Paste)," and no signs of accelerated strain increase are observed, suggesting that reinforcement suppresses shrinkage.

The time-dependent changes in internal strain from immediately after placement, including specimens with reinforcement, are shown in **Figure 3-16**. These strains also exclude thermal strain. During the curing period, "W/P17% (Paste)" and "Reinforced" exhibit significant expansion, and their drying shrinkage strains remain small, indicating that they are still in the expansion range at 100 days of age relative to the initial placement. However, these results assume a thermal expansion coefficient of $10 \times 10^{-6}/℃$, and different results could arise if the actual coefficient differs. Comparing "W/P17% (Paste)" and "Reinforced," the expansion magnitude is smaller for "Reinforced." Since the mix proportion is identical and the thermal expansion coefficient is presumed the same, the difference in expansion magnitude is likely due to the restraint effect of reinforcement limiting specimen expansion.

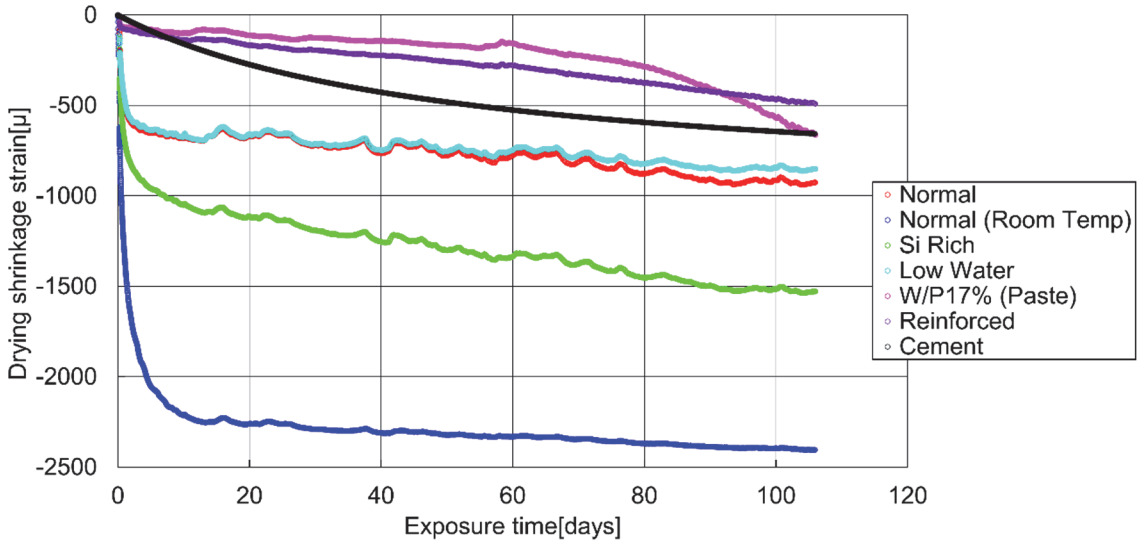

Figure 3-15 Change in drying shrinkage strain

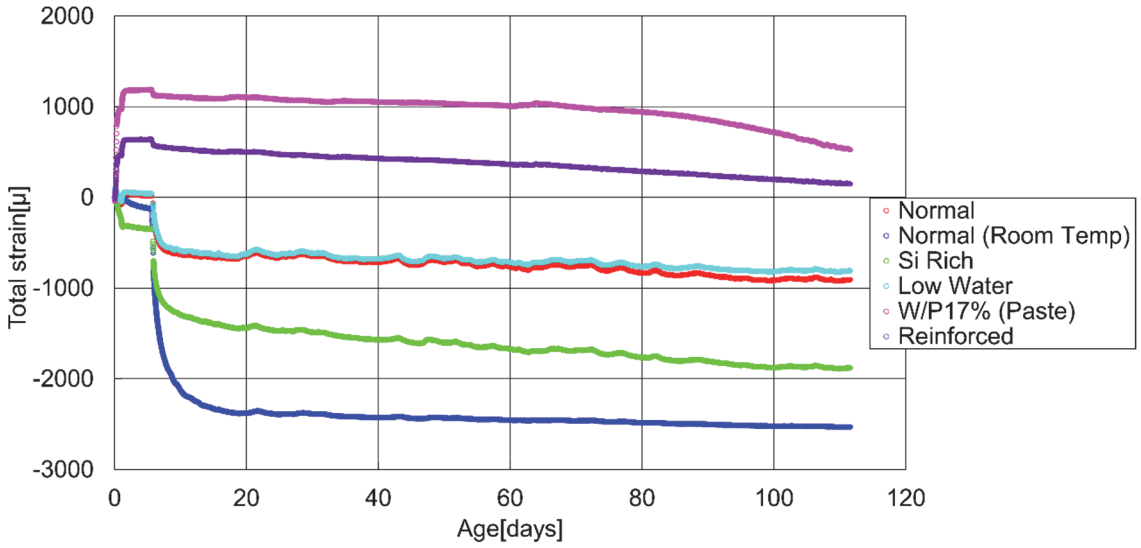

Figure 3-16 Change in total strain

3.4.2. Creep behavior

The time-dependent changes in creep strain obtained from the loaded specimens are shown in **Figure 3-17**. The creep strain was calculated using Equation (3-20).

$$\varepsilon_{ct} = \varepsilon_{at} - \varepsilon_e - \varepsilon_{st} \qquad (3-20)$$

$$\varepsilon_e = \varepsilon_{at0} - \varepsilon_{st0} \qquad (3-21)$$

Where:

ε_{ct}: Creep strain ($\times 10^{-6}$)

ε_{at}: Strain of the loaded specimen with thermal strain removed ($\times 10^{-6}$)

ε_{e}: Elastic strain ($\times 10^{-6}$)

ε_{st}: Strain of the unloaded specimen with thermal strain removed ($\times 10^{-6}$)

ε_{at0}: Strain of the loaded specimen at the end of loading ($\times 10^{-6}$)

ε_{st0}: Strain of the unloaded specimen at the end of loading ($\times 10^{-6}$)

From **Figure 3-17**, it is evident that the magnitude of creep strain, like drying shrinkage strain, varies significantly depending on mix and curing conditions. The magnitude of creep strain in GP concrete specimens generally aligns with the trends in drying shrinkage strain; however, the relationship between creep strain and drying shrinkage strain is reversed for "Normal" and "Low Water." Additionally, the creep strain of "W/P17% (Paste)" is more than twice that of "Normal" and exhibits greater variability.

The time-dependent changes in creep strain per unit stress are shown in **Figure 3-18**. The creep strain per unit stress was calculated using Equation (3-22).

$$\mu\varepsilon_{ct} = \frac{\varepsilon_{ct}}{\sigma} \qquad (3-22)$$

Where:

$\mu\varepsilon_{ct}$: Creep strain per unit stress ($\times 10^{-6}/(\mathrm{N/mm^2})$)

ε_{ct}: Creep strain ($\times 10^{-6}$)

σ: Applied stress ($\mathrm{N/mm^2}$)

Additionally, using the creep strain prediction equation per unit stress provided in the 2022 Concrete Standard Specification [Design Edition] (Equation (3-12), reproduced), the time-dependent changes in creep strain per unit stress for general cement concrete were estimated and included in the figure ("Cement").

$$\varepsilon'_{cc}(t,t')/\sigma'_{cp} = \frac{4W(1-RH/100)+350}{12+f'_c(t')} \cdot \log_e(t-t'+1) \qquad (3-12, \text{Reproduced})$$

$$t \text{ and } t' = \sum_{i=1}^{n} \Delta t_i \cdot exp\left[13.65 - \frac{4000}{273+T(\Delta t_i)/T_0}\right] \qquad (3-13, \text{Reproduced})$$

Where:

$\varepsilon'_{cc}(t,t')/\sigma'_{cp}$: Creep strain per unit stress of concrete loaded at an effective age of t' (days) at the

time of age t (days) ($\times 10^{-6}/(\mathrm{N/mm^2})$)

W: Unit water volume of concrete (kg/m³), assumed as $W = 165\mathrm{kg/m^3}$.

RH: Relative humidity (%), assumed as the average relative humidity during the measurement period ($RH = 44.5\%$).

t' and t: Effective age of concrete at loading and during loading (days), corrected using Equation (3-13). ($t' \geq 7$ days)

Δt_i: Duration of the period at temperature T (°C)

T_0: 1°C

$f'_c(t')$: Compressive strength of concrete at effective age t' (days) at the time of loading (N/mm²), assumed as $f'_c(t') = 30\mathrm{N/mm^2}$.

From **Figure 3-18**, the creep strain per unit stress of all GP specimens exceeds that of "Cement," indicating that GP generally exhibits a higher creep strain per unit stress than conventional cement concrete.

The time-dependent changes in the creep coefficient are shown in **Figure 3-19**. The creep coefficient was calculated using Equation (3-23).

$$\phi_t = \frac{\varepsilon_{ct}}{\varepsilon_e} \qquad (3-23)$$

Where:

ϕ_t: Creep coefficient

ε_{ct}: Creep strain ($\times 10^{-6}$)

ε_e: Elastic strain ($\times 10^{-6}$)

Additionally, using the creep coefficient prediction equation provided in the 2022 Concrete Standard Specification [Design Edition] (Equation (3-15), reproduced), the time-dependent changes in the creep coefficient for general cement concrete were estimated and included in the figure ("Cement").

$$\phi(t,t') = \frac{4W(1-RH/100)+350}{12+f'_c(t')} \cdot \log_e(t-t'+1) \cdot E_{ct} \qquad (3-15, \text{Reproduced})$$

$$E_{ct} = \left[k_1 + \frac{f'_c(t') - k_2}{k_3}\right] \times 10^4 \qquad (3-24)$$

Where:

$\phi(t,t')$: Creep coefficient for concrete loaded at age t' (days), evaluated at age t (days)

E_{ct}: Young's modulus of concrete at the effective age of t' (days) at the time of loading, calculated using the formula provided in the 2022 Concrete Standard Specification (Equation (3-24)).

k_1, k_2, k_3: Coefficients for the Young's modulus calculation formula, set as $k_1 = 2.8$, $k_2 = 30$, and $k_3 = 33$ based on **Table 3-7**.

Table 3-7 Coefficients in the Young's modulus calculation formula**(49)**

Compressive strength range	k_1	k_2	k_3
$f'_c < 30\mathrm{N/mm^2}$	2.2	18	20
$30 \leq f'_c < 40\mathrm{N/mm^2}$	2.8	30	33
$40 \leq f'_c < 70\mathrm{N/mm^2}$	3.1	40	50
$70 \leq f'_c < 80\mathrm{N/mm^2}$	3.7	70	100

From **Figure 3-19**, the creep coefficient of GP specimens correlates with creep strain, and the trends are consistent. The creep coefficients of "Normal" and "Low Water" are smaller than those of "Cement," while those of "Si Rich" and "Normal (Room Temp)" are larger. The creep coefficient of "W/P17% (Paste)" is comparable to or slightly larger than that of "Cement." Similar to drying shrinkage, creep generally increases in the absence of aggregates compared to when aggregates are present. Therefore, the creep coefficient of binder-only materials is expected to be larger than that of "Cement." When comparing binder-only materials, low W/P GP exhibits smaller creep than the hardened cement paste in conventional cement concrete. Consequently, it is anticipated that concrete using low W/P GP as a binder will exhibit smaller creep than conventional cement concrete. Additionally, GP concrete shows a characteristic behavior similar to drying shrinkage: it deforms significantly immediately after loading, and subsequent deformation proceeds more gradually, differing from cement concrete. Consequently, the creep coefficients of "Normal" and "Low Water" are initially larger than those of "Cement" but become smaller after 20–40 days. This suggests that the creep coefficients of "Si Rich" and "Normal (Room Temp)" may also eventually become smaller than those of "Cement."

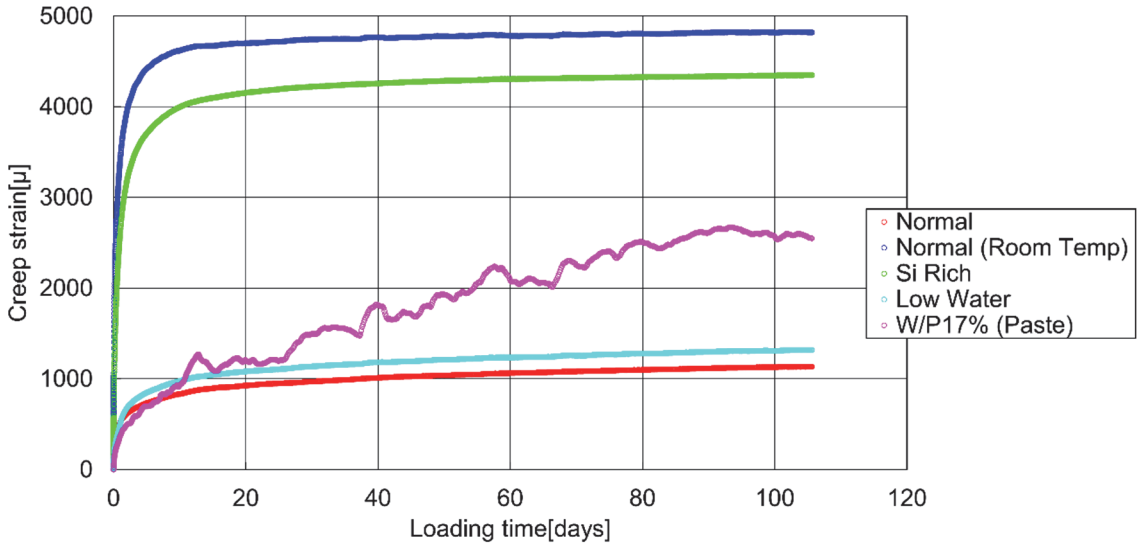

Figure 3-17 Change in creep strain

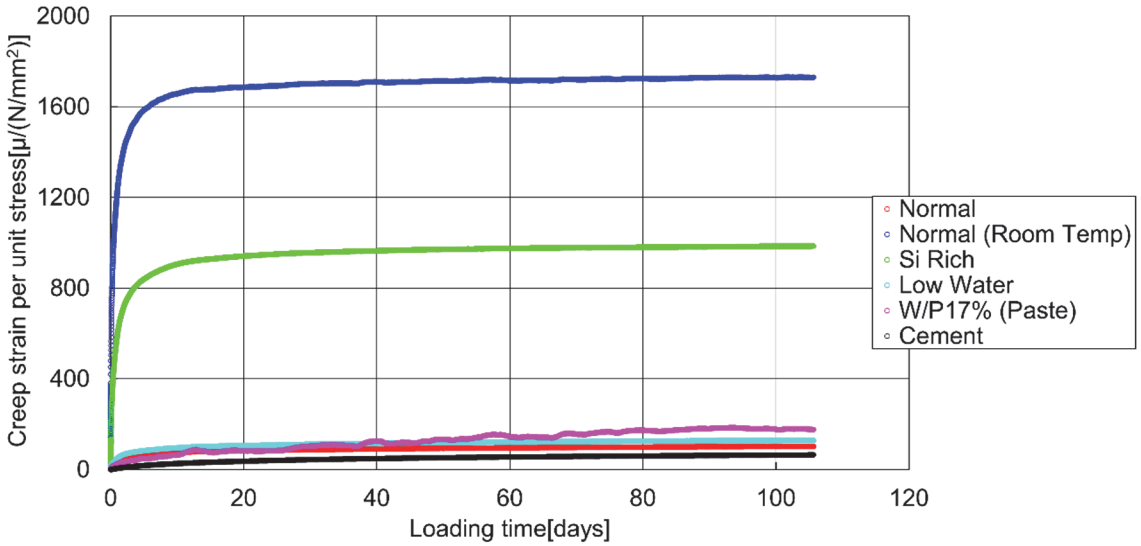

Figure 3-18 Change in creep strain per unit stress

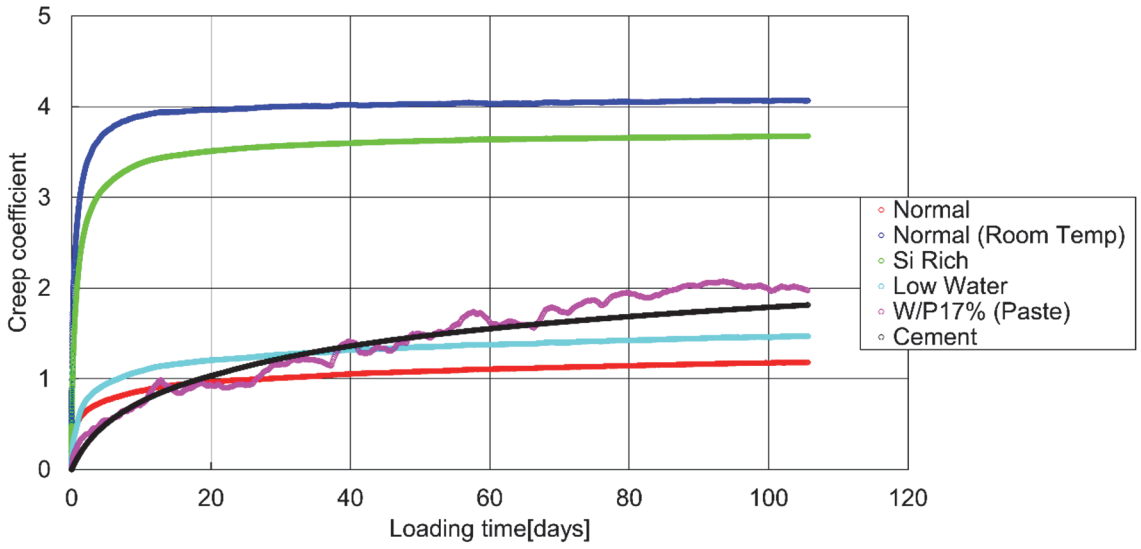

Figure 3-19 Change in creep coefficient

3.4.3. Compressive strength and Young's modulus

The time-dependent changes in compressive strength, including results at 5 days of age, are shown in **Figure 3-20**. First, the compressive strength of the "Normal" mix level is comparable to or slightly higher than that of conventional cement concrete with a W/C of approximately 50%. However, the compressive strength of GP concrete with 0% slag substitution in the standardized GP tests conducted in Japan is around 10 N/mm², significantly lower than the results obtained in this study. This discrepancy is likely due to differences in the heating rate, heating duration, or curing methods. In the standardized tests, the temperature increases from 20°C to 60°C over three hours, with a 60°C hold time of 12 hours. In contrast, in this study, the temperature rises from 20°C to 60°C in 30 minutes to an hour, with a 60°C hold time of 24 hours. This suggests that the greater heat input in this study accelerated the reaction. Additionally, the standardized tests involve demolding after heating and then air curing, while this study involves sealed curing for five days after heating before demolding. This sealed curing may have promoted reactions between the alkaline solution and particles in the pores, filling them and enhancing strength. The compressive strength of "Normal (Room Temp)" is lower than "Normal," indicating that GP with only FA as the reactive filler does not achieve sufficient strength without accelerated reactions during heat curing. However, especially within the first 28 days of curing, the strength increase rate is higher compared to other mix levels. This is likely because the lack of heat-induced reaction acceleration leaves many unreacted ions in the pores, which gradually react over time. The compressive strength of "Si Rich" is lower than "Normal" despite heat curing. Increasing the Si/A ratio reduces the A/W ratio, decreasing the alkalinity and the activation potential of the alkali, which may have hindered the reaction. The compressive strength of "Low Water" is slightly lower than "Normal," indicating that reducing the unit water content and L/P ratio does not

significantly increase strength in GP concrete, unlike in cement concrete. This is likely because reducing the amount of alkaline solution decreases the absolute amount of reactive ions, thereby limiting the reaction. "W/P17% (Paste)" exhibits significantly higher strength than other mix levels, demonstrating successful high-strength development through a low W/P ratio. However, the compressive strength is slightly lower compared to GP with W/P = 15% in CHAPTER 2, indicating that minor differences in W/P at extremely low levels can have a substantial impact on compressive strength. The high variability in compressive strength is likely due to poor filling caused by rapid setting.

The time-dependent changes in Young's modulus are shown in **Figure 3-21**. The trends in Young's modulus closely follow those of compressive strength, with higher compressive strength corresponding to higher Young's modulus. The relationship between Young's modulus and compressive strength is shown in **Figure 3-22**. From **Figure 3-22**, the relationship between the Young's modulus and compressive strength in GP can potentially be approximated logarithmically. The relationship between measured Young's modulus and calculated values using Equation (3-24) is shown in **Figure 3-23**. From **Figure 3-23**, it is evident that the measured Young's modulus is lower than the calculated values. Thus, it is difficult to directly apply the prediction equations for the Young's modulus of cement concrete to GP.

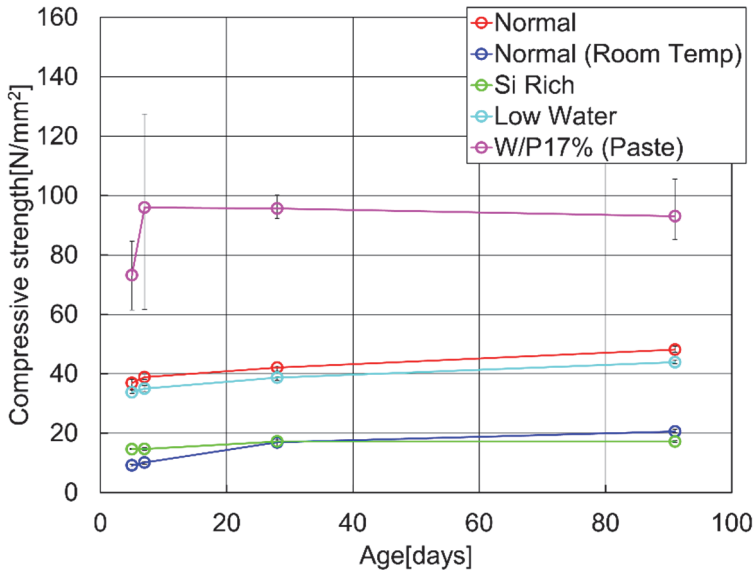

Figure 3-20 Change in compressive strength from 5 days to 91 days of age

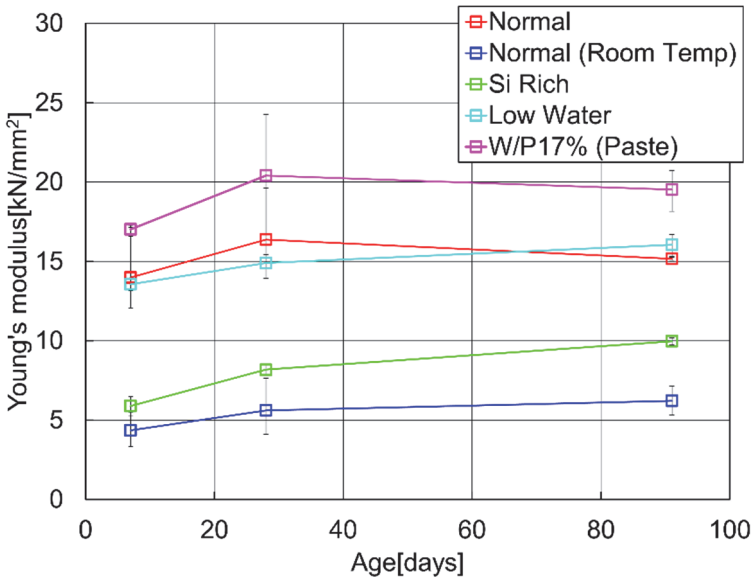

Figure 3-21 Change in Young's modulus from 7 days to 91 days of age

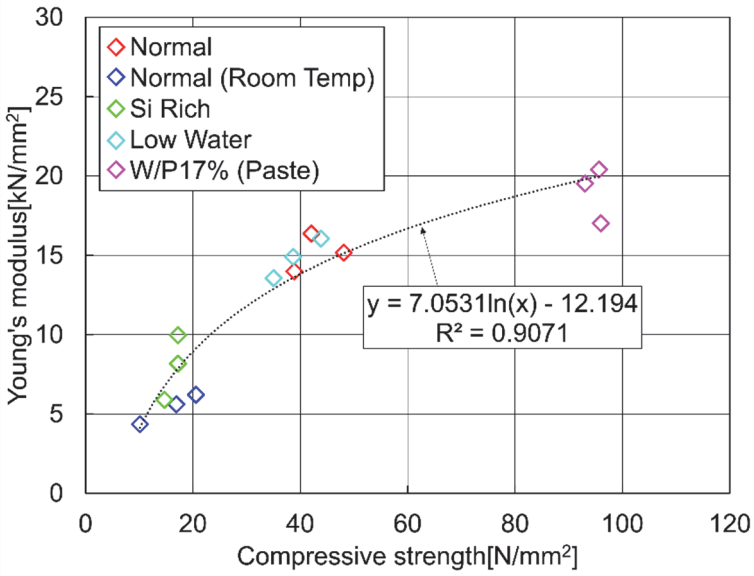

Figure 3-22 Relation between the Young's modulus and the compressive strength

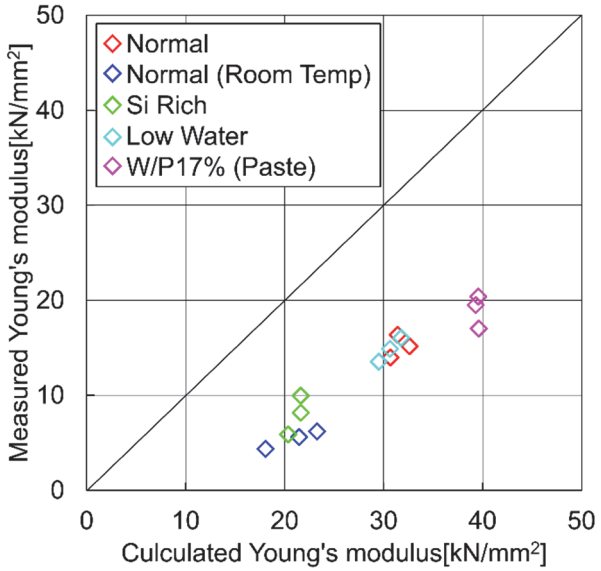

Figure 3-23 Relation between the measured Young's modulus and the calculated Young's modulus

3.4.4. Weight change

The time-dependent changes in specimen weight after exposure are shown in **Figure 3-24**. From **Figure 3-24**, the weight changes of "W/P17% (Paste)" and "Reinforced" are about one-fifth of those of GP concrete. However, there are no significant differences among the GP concrete specimens. GP concrete exhibits relatively large weight changes immediately after exposure, followed by more gradual changes after about 10 days.

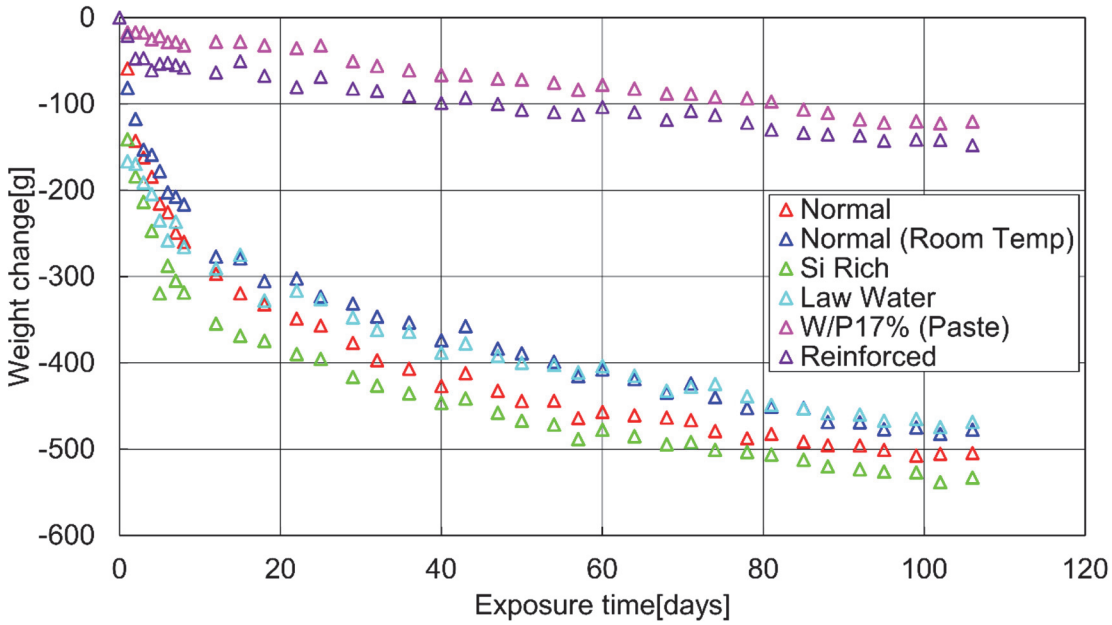

Figure 3-24 Weight change

3.4.5. Pore distribution

The cumulative pore volumes at 28 and 91 days of age are shown in **Figure 3-25** and **Figure 3-26**, respectively, while the pore size distributions are shown in **Figure 3-27** and **Figure 3-28**, respectively. For comparison with general cement concrete, the cumulative pore volume and pore size distribution of W/C = 50% cement concrete after sufficient reaction at 210 days of age are included as "Cement" in the figures. The vertical axis, "pore volume," represents the proportion of sample volume occupied by pores.

Comparing 28 and 91 days of age, there are no significant differences in cumulative pore volume and pore size distribution except for "Normal (Room Temp)." This suggests that the accelerated reactions during heat curing lead to early reaction completion. Conversely, "Normal (Room Temp)" exhibits a decrease in pores around 13 nm from 28 to 91 days, suggesting that delayed reactions gradually progressed over time, filling the pores.

Focusing on total pore volume, GP concrete generally exhibits higher total pore volumes than "Cement." The low W/P mix, "W/P17% (Paste)," shows about one-fifth the total pore volume of other mix levels and less than half that of "Cement."

Examining pore size distribution, "Cement" contains the largest number of pores in the 30–60 nm range, whereas GP has a higher concentration of smaller pores. Compared to "Normal," "Si Rich" has overall larger pore sizes, resulting in a higher total pore volume. While "Normal (Room Temp)" has a total pore volume similar to "Normal," its pore size distribution is concentrated around 13 nm, with fewer pores above 30 nm. "Low Water" exhibits reduced overall pore volume and fewer pores, leading to a smaller total pore volume. "W/P17% (Paste)" shows almost no pores above 10 nm but may have a certain amount of pores smaller than a few nanometers.

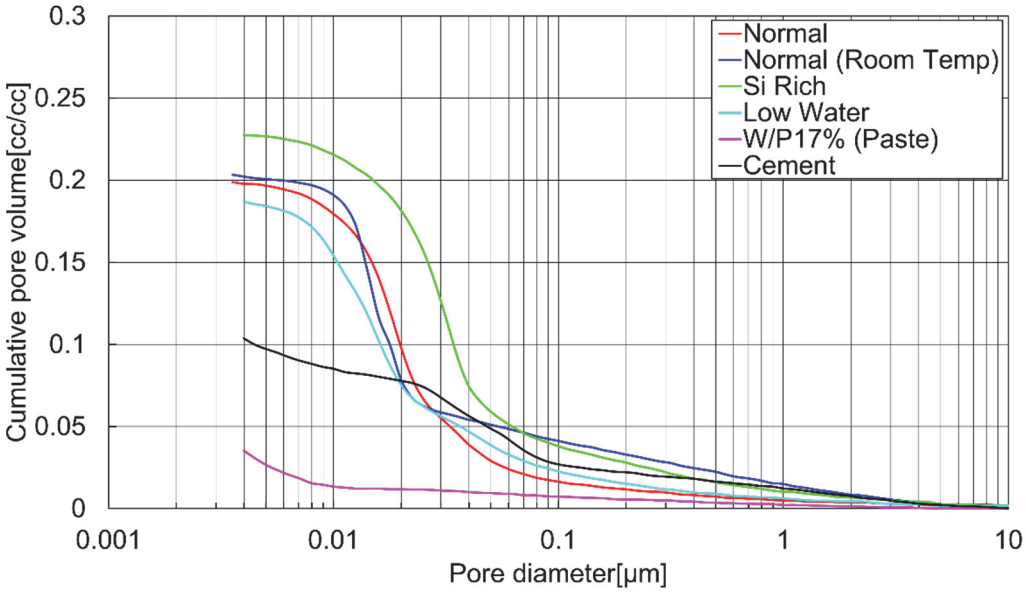

Figure 3-25 Cumulative pore volume at 28 days of age

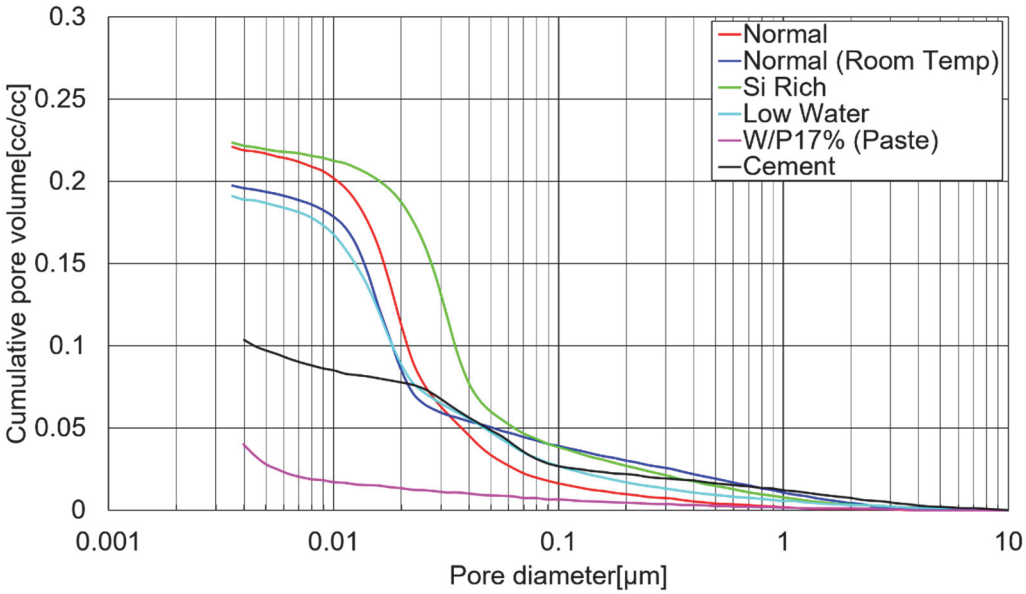

Figure 3-26 Cumulative pore volume at 91 days of age

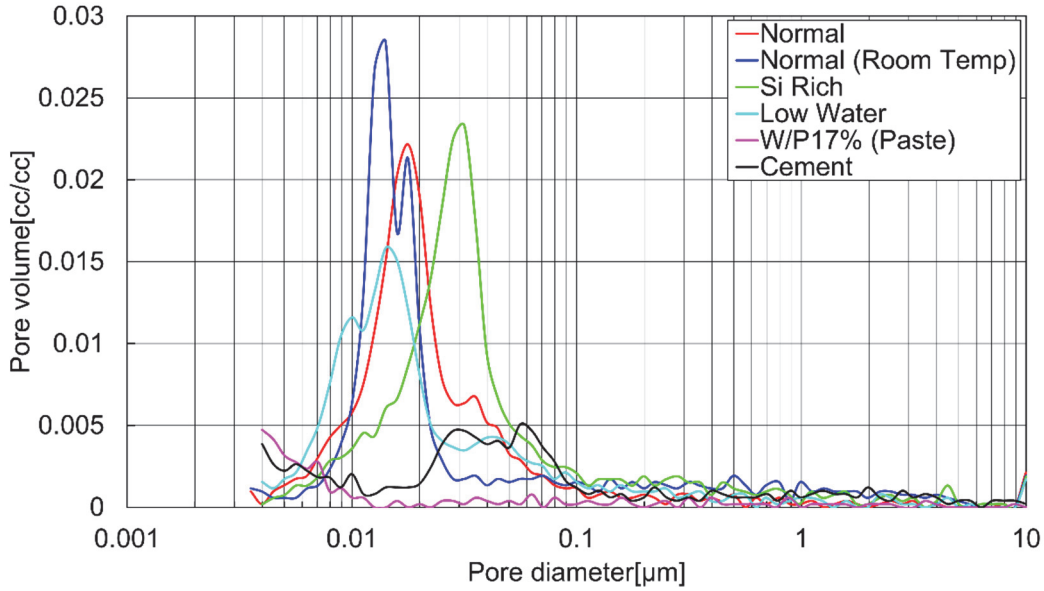

Figure 3-27 Pore distribution at 28 days of age

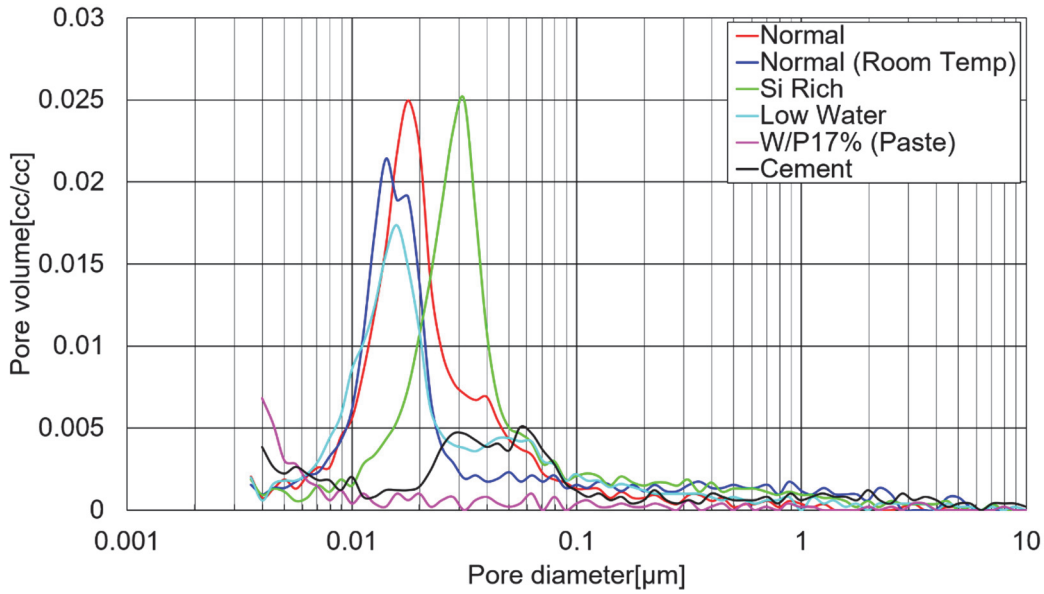

Figure 3-28 Pore distribution at 91 days of age

3.5. Consideration

In this section, the factors and mechanisms influencing the shrinkage and creep characteristics of geopolymer (GP) concrete are discussed based on the results presented in Section 3.4.

3.5.1. Shrinkage of geopolymer

Regarding "Normal," its compressive strength is comparable to that of conventional cement concrete, while its total pore volume is larger and its pore size distribution is concentrated in smaller diameters. As a result, the amount of water loss (dehydration) is greater than that of cement concrete, and the capillary tension is also larger. This is believed to result in greater drying shrinkage than in cement concrete. Moreover, since water is not consumed in the solidification reaction of GP, a large amount of water remains in the pores of the specimens immediately after exposure. Furthermore, due to the abundance of similarly sized pores, the ink-bottle effect is less likely to occur, resulting in a pore structure that facilitates water escape. Consequently, a large amount of water is lost immediately after exposure, leading to significant deformation, but the subsequent reduction in water loss lowers capillary tension, resulting in more gradual shrinkage over time.

In "Normal (Room Temp)," a similar phenomenon is likely occurring. However, due to its lower strength and smaller pore diameters compared to "Normal," the capillary tension is higher, and the structural resistance to this tension is weaker. Therefore, shrinkage is larger than in "Normal."

Although the strength of "Si Rich" is similar to "Normal (Room Temp)," its pores are concentrated in larger diameters compared to both "Normal (Room Temp)" and "Normal," reducing capillary tension. As a result, shrinkage is smaller than in "Normal (Room Temp)."

In "Low Water," the strength is similar to "Normal," but the pores are slightly smaller in diameter, leading to slightly higher capillary tension. However, the unit water content—i.e., the amount of water remaining in the pores—and the total pore volume are both smaller than in "Normal." Consequently, while the capillary tension per pore is higher, the overall capillary tension across the specimen is similar to "Normal," resulting in comparable shrinkage.

The "W/P17% (Paste)" sample is considered to have low capillary tension and high resistance to capillary tension due to its high strength and small total pore volume. This suggests that, despite the absence of aggregates and being composed solely of the binder, it exhibits less shrinkage than GP concrete. Additionally, after approximately 70 days of exposure, an acceleration in the increase of drying shrinkage strain was observed. This is presumed to be due to an increase in shrinkage driving force caused by mechanisms unique to low-W/P GP as the relative humidity (RH) decreased. From **Figure 3-14**, it can be observed that the average RH remained above approximately 40% for the first 70 days of exposure but fell below 40% thereafter. The extremely small pore size of low-W/P GP suggests that the viscoplastic behavior of water dominates, leading to a slow rate of water evaporation from the pores. This likely caused drying shrinkage to progress gradually during the initial exposure period. After approximately 70 days, as the RH fell below 40%, water fully evaporated from relatively larger pores (greater than several nanometers), and water began to dissipate from smaller pores (less than several nanometers), increasing the capillary tension. Furthermore, during the initial 70 days, disjoining pressure likely acted within smaller pores, but this pressure is believed to have decreased

after 70 days due to water dissipation. Consequently, the combined effects of increased capillary tension and decreased disjoining pressure accelerated the driving force for shrinkage, leading to a faster progression of drying shrinkage.

Here, both "W/P17% (Paste)" and "Reinforced" do not contain aggregates, possess a dense internal structure, and exhibit high strength. As a result, their thermal expansion coefficient might differ from that of conventional concrete or other GP concretes. According to Teramoto et al.[52], cementitious materials with low W/P ratios and ultra-high strength typically exhibit a thermal expansion coefficient larger than that of conventional cement concrete, reaching approximately $20 \times 10^{-6}/℃$. Similarly, the thermal expansion coefficient of low W/P GP is also expected to be greater than that of conventional cement concrete. For "W/P17% (Paste)" and "Reinforced," the drying shrinkage strain with temperature strain removed is shown in **Figure 3-29** for two cases: when the thermal expansion coefficient is assumed to be $10 \times 10^{-6}/℃$ and when it is assumed to be $20 \times 10^{-6}/℃$. For comparison, "Cement" is also included in the figure. From **Figure 3-29**, it can be observed that as the thermal expansion coefficient increases, the drying shrinkage strain of "W/P17% (Paste)" and "Reinforced" decreases, with the drying shrinkage strain of "W/P17% (Paste)" becoming slightly smaller than that of "Cement." Therefore, considering the effect of the thermal expansion coefficient, it can be suggested that low W/P GP is likely to exhibit less shrinkage than conventional cement concrete even when used independently.

From the observed shrinkage behavior and inferred mechanisms across the mix levels, it can be concluded that the shrinkage characteristics of GP are influenced by structural strength, total pore volume, and pore size distribution, similar to hardened cement paste. Higher structural strength, smaller total pore volume, and a concentration of larger pores are associated with reduced shrinkage. GP's structural strength, total pore volume, and pore size distribution vary significantly with mix proportion parameters such as L/P, W/P, A/W, and Si/A. Based on the results, reducing unit water content, lowering L/P or W/P to increase packing density, and increasing A/W to enhance alkalinity—combined with heat curing to accelerate reactions—are effective measures. These approaches increase resistance to shrinkage-driving forces through high strength while reducing water loss and total pore volume, thereby mitigating shrinkage. The "W/P17% (Paste)" mix successfully achieved these conditions, demonstrating its potential to suppress shrinkage and crack formation, which is crucial for low-W/P GP with high radio wave transparency. However, it is important to note that for low-W/P GP, drying shrinkage may accelerate significantly when the RH drops below approximately 40%, necessitating careful monitoring and consideration. Additionally, the shrinkage characteristics of GP exhibit a distinct behavior, with significant deformation occurring immediately after the start of exposure, followed by gradual deformation. This suggests that exposing the elements for several days before applying constraints could potentially suppress cracking.

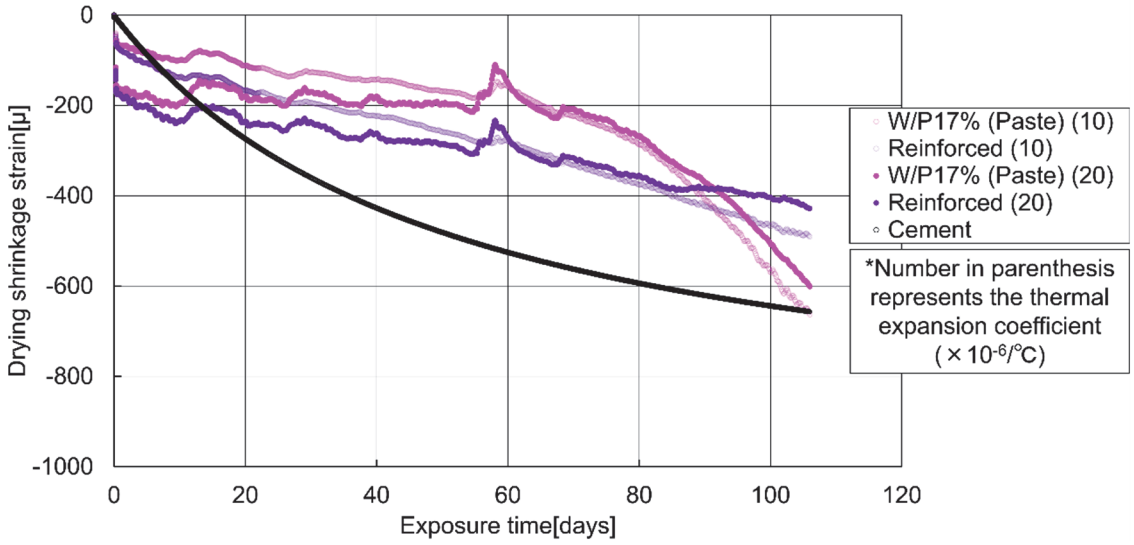

Figure 3-29 Comparison of drying shrinkage strain when the thermal expansion coefficient is set to $\mathbf{10 \times 10^{-6}}$/℃ and when it is set to $\mathbf{20 \times 10^{-6}}$/℃

3.5.2. Creep of geopolymer

The creep characteristics of GP concrete specimens, except "W/P17% (Paste)," follow similar trends to their shrinkage characteristics and are influenced by structural strength, total pore volume, and pore size distribution. Like shrinkage, GP exhibits a distinct behavior compared to cement concrete, with large deformation immediately after loading that gradually diminishes. This is attributed to significant water loss from the pores under load shortly after loading, followed by minimal subsequent water loss. Additionally, the influence of structural strength is more pronounced under load, leading to a stronger correlation between compressive strength and creep strain or creep coefficient. Structural strength particularly affects initial deformation: lower strength results in greater creep deformation of the structure itself, accompanied by higher water loss, contributing to larger overall creep deformation. However, the amorphous structure of GP differs fundamentally from the crystalline structure of cement hydrates (e.g., C-S-H), suggesting that the deformation mechanisms of GP's structure significantly influence its creep characteristics.

Conversely, the "W/P17% (Paste)" mix, which exhibited the smallest shrinkage, showed larger creep strain and creep coefficients compared to "Normal" and "Low Water," behaving similarly to typical cement concrete. Although the high strength of "W/P17% (Paste)" minimizes initial deformation, its small pore volume and difficulty in water egress lead to gradual water movement to finer pores under loading, resulting in behavior similar to cement concrete. The absence of aggregates in this mix increases the unit water content and water loss, leading to greater deformation. Vertical cracks observed in the specimen 80 days after loading suggest increased moisture exchange compared to unloaded specimens, possibly amplifying creep strain variations due to relative humidity

fluctuations.

From the observed creep behavior and inferred mechanisms, it can be concluded that GP creep characteristics are influenced by structural strength, total pore volume, and pore size distribution, as well as the deformation properties of the structure itself. To suppress GP creep, increasing strength to reduce initial deformation and designing a pore structure that facilitates water loss are essential. Maintaining moderate unit water content and L/P or W/P, while enhancing structural strength through higher A/W or increased curing temperatures, is effective. Additionally, based on the results for "W/P17% (Paste)," it can be inferred that using low-W/P GP, which exhibits excellent radio wave transparency, as a binder has a high potential to suppress creep. Furthermore, the creep behavior of low-W/P GP on its own appears to be predictable using conventional creep prediction equations for standard cement concrete.

3.6. Future prospects

The exposure and loading periods in this study were approximately 100 days, which is relatively short. To fully understand the shrinkage and creep characteristics of geopolymer (GP), it is essential to continue the tests over a longer period and expand the dataset. In particular, at this stage, the shrinkage and creep of "Normal (Room Temp)" and "Si Rich" are larger than those of conventional cement concrete. However, with prolonged exposure and loading, they may become smaller than those of conventional cement concrete. Additionally, "W/P17% (Paste)" and "Reinforced" specimens are still in an expansion phase compared to their condition immediately after casting, and their behavior should be carefully monitored in the future. Furthermore, measuring the thermal expansion coefficient of the specimens is expected to yield more accurate thermal strain data, leading to more precise shrinkage and creep strain measurements.

In the pore structure analysis, the mercury intrusion method measures pore sizes ranging from a few nanometers to several tens of micrometers, corresponding to capillary pores. However, particularly for low water-to-powder ratio (W/P) GP, it is likely that pores smaller than a few nanometers exist. While this study did not include such measurements, employing techniques like gas adsorption (BET method) to measure pores smaller than a few nanometers and using methods like the Archimedes method to determine total porosity is expected to clarify the relationship between shrinkage and creep characteristics and the pore size distribution and porosity of GP.

Water movement within concrete is influenced by not only the pore structure but also the contact angle of the inner pore walls. The roughness of GP's pore walls and the physical properties of the pore solution are considered fundamentally different from those of cement paste, which likely results in different contact angles. Measuring contact angles is expected to provide further insight into the effects of water movement within GP on its shrinkage and creep characteristics.

Moreover, by utilizing the characteristic shrinkage and creep behavior of geopolymer (GP), which

exhibits significant deformation immediately after exposure or loading followed by a gradual decrease in deformation, it is expected that the calculation and control of prestress can be facilitated. This suggests that GP could be highly beneficial for application in prestressed concrete (PC). However, research on prestressed GP concrete remains limited, and no studies have yet been conducted at the scale of actual structures. Therefore, further investigations, including manufacturing methods, are necessary to explore the feasibility of GP application in PC.

3.7. Concluding remarks

The study of the time-dependent deformation characteristics of geopolymer (GP) yielded the following insights:

(1) The shrinkage and creep characteristics of GP using fly ash (FA) as the sole active filler vary significantly depending on the mix proportion and curing conditions.

(2) GP's shrinkage and creep characteristics are influenced by structural strength, total pore volume, and pore size distribution. Creep characteristics are thought to be more strongly affected by structural strength compared to shrinkage.

(3) Compared to conventional cement concrete, GP exhibits a characteristic behavior where significant deformation occurs immediately after exposure or loading, followed by minimal deformation thereafter.

(4) To suppress shrinkage, reducing unit water content, lowering L/P or W/P to increase packing density, increasing A/W to enhance alkalinity, and promoting reactions through heat curing are effective. These measures increase resistance to shrinkage-driving forces through high strength, while reducing dehydration and total pore volume, thereby minimizing the overall shrinkage-driving force across the component.

(5) To suppress creep, it is effective to avoid excessively low unit water content, L/P, and W/P. Instead, increasing A/W or raising curing temperatures to enhance structural strength can reduce initial deformation under load and prevent subsequent deformation by creating a pore structure that facilitates water release.

(6) Concrete using low-W/P GP as a binder, which exhibits excellent radio wave transparency, is expected to experience less shrinkage compared to standard cement concrete, with a high potential to suppress cracks caused by shrinkage. Furthermore, concrete utilizing low-W/P GP as a binder may exhibit lower creep compared to conventional cement concrete.

(7) Continued shrinkage and creep testing, combined with detailed pore structure analysis using the BET method or the Archimedes method, as well as analysis of contact angles within pore walls, are expected to elucidate the mechanisms of water movement within GP. These efforts will contribute to a more detailed understanding of the mechanisms underlying shrinkage and creep in GP.

References

(1) 土木学会 複合構造委員会 複合構造におけるコンクリートの収縮・クリープの影響に関する研究小委員会. 複合構造におけるコンクリートの収縮・クリープの影響 ―材料と構造の新たな境界問題―. 丸善出版, 2022.

(2) Kurihara, R., Chijiwa, N. Investigation on the stiffness reduction of RC shear walls subjected to environmental action by multi-scale thermo-hygral analysis. The 66th Japan National Congress for Theoretical and Applied Mechanics. 2022, Vol. 66, pp. 213.

(3) Kurihara, R., Chijiwa, N. Multiscale analysis of shrinkage-induced performance degradation of shear wall and application to structural analysis. Structures. 2024, Vol. 61, pp. 106051.

(4) Kurihara, R., Chijiwa, N., Maekawa, K. Thermo-Hygral Analysis on Long-Term Natural Frequency of RC Buildings with Different Dimensions. Journal of Advanced Concrete Technology. 2017, Vol. 15, No. 8, pp. 381–396.

(5) 千々和伸浩, 石田哲也, 前川宏一. セメント硬化体中の微視的機構モデルに基づく実 PC 橋の長期時間依存変形シミュレーション. コンクリート工学年次論文集. 2010, Vol. 32, pp. 407‐412.

(6) Ohno, M., Chijiwa, N., Suryanto, B., Maekawa, K. An Investigation into the Long-Term Excessive Deflection of PC Viaducts by Using 3D Multi-scale Integrated Analysis. Journal of Advanced Concrete Technology. 2012, Vol. 10, pp. 47–58.

(7) 今井遥平, 千々和伸浩, 永来良吾. 月夜野大橋の長期的なクリープ計測と一考察. プレストレストコンクリート工学会 第 29 回シンポジウム論文集. 2020, pp. 179‐182.

(8) 木原亮太, 千々和伸浩, 洪汶宜. 地中 RC ボックスカルバートの遅れせん断ひび割れ発生機構に関する検討. 土木学会第 72 回年次学術講演会講演概要集. 2017, pp. 625–626.

(9) Mindess, S., Young, J. F. Concrete. Prentice-Hall, 1981, pp. 418–440, ISBN978-0-13-167106-5. https://books.google.co.jp/books?id=_7tRAAAAMAAJ.

(10) 谷村充, 富田六郎. “体積変化制御の物理と化学”. コンクリート混和材料ハンドブック. 日本材料学会, エヌ・ティー・エス, 2004, pp. 78‐90.

(11) Powers, Treval Clifford. Mechanisms of Shrinkage and Reversible Creep of Hardened Cement Paste, The Structure of Concrete. 1965. https://api.semanticscholar.org/CorpusID:210750477.

(12) 日本建築学会. 鉄筋コンクリート造建築物の収縮ひび割れ : メカニズムと対策技術の現状. 2003, ISBN4-8189-1030-9. https://ci.nii.ac.jp/ncid/BA62673365.

(13) Bazant, Zdenek, Wittmann, Folker. Creep and Shrinkage in Concrete Structures. 1982, ISBN0 471 10409 4.

(14) Feldman, R. F., Sereda, P. J. A model for hydrated Portland cement paste as deduced from sorption-length change and mechanical properties. Matériaux et Construction. 1968, Vol. 1, No. 6, pp. 509–520.

(15) Feldman, R. F. Density and porosity studies of hydrated Portland cement. Cement Technology. 1972, Vol. 3, No. 1, pp. 5–14.
(16) Ishai, Ori. The time-dependent deformational behaviour of cement paste, mortar and concrete. 1968, pp. 345–364.
(17) Alizadeh, Aali. Nanostructure and Engineering Properties of Basic and Modified Calcium-Silicate-Hydrate Systems. 2009.
(18) Uchikawa, H. Structural change of hardened mortar by drying. 3rd NCB international seminar (New Dehli-India). 1991, Vol. 4, "VIII-1"-"VIII-12".
(19) 田澤栄一. 水和反応による硬化セメントペーストのマクロな体積減少. セメント･コンクリート論文集. 1991, No. 45, pp. 122‐127.
(20) A. M. Paillere, M. Buil, and J. J. Serrano. Effect of Fiber Addition on the Autogenous Shrinkage of Silica Fume. ACI Materials Journal. 1989, Vol. 86, No. 2.
(21) 田澤栄一, 宮澤伸吾. 水和による自己収縮. コンクリート工学. 1994, Vol. 32, No. 9, pp. 25‐30.
(22) 田澤栄一. 自己収縮に及ぼすセメントの化学組成の影響. セメント･コンクリート論文集. 1993, Vol. 47, pp. 528‐533.
(23) Japan Society of Civil Engineers. Standard Specifications for Concrete Structures -2022 [Design Chapter]. 2023.
(24) 土木学会. コンクリート技術シリーズ No.132 土木分野におけるジオポリマー技術の実用化推進のための研究小委員会（361 委員会）成果報告書. 2022.
(25) Ridtirud, Charoenchai, Chindaprasirt, Prinya, Pimraksa, Kedsarin. Factors affecting the shrinkage of fly ash geopolymers. International Journal of Minerals, Metallurgy, and Materials. 2011, Vol. 18, No. 1, pp. 100–104.
(26) Nodehi, Mehrab, Taghvaee, Vahid Mohamad. Alkali-Activated Materials and Geopolymer: a Review of Common Precursors and Activators Addressing Circular Economy. Circular Economy and Sustainability. 2022, Vol. 2, No. 1, pp. 165–196.
(27) 佐藤隆恒, 上原元樹, 山﨑淳司. 低アルカリ水比, 高ケイ素アルカリ比のケイ酸アルカリ溶液を使用したジオポリマー硬化体の諸性質. コンクリート工学年次論文集. 2017, Vol. 39, No. 1, pp. 2035‐2040.
(28) 本間雅人. 加温養生を行ったジオポリマーモルタルの収縮特性. ジオポリマー･戻りコン, 材料施工, 2014 年度日本建築学会大会(近畿)学術講演会･建築デザイン発表会. 2014, pp. 355‐356.
(29) 一宮一夫, 原田耕司, 津郷俊二, 池田攻. フライアッシュ４種を用いたジオポリマーモルタルの基礎物性. コンクリート工学年次論文集. 2012, Vol. 34, No. 1, pp. 1900‐1905.
(30) 上原元樹, 南浩輔, 平田紘子, 山﨑淳司. ジオポリマー硬化体の配合･作製法と諸性質. コンクリート工学年次論文集. 2015, Vol. 37, No. 1, pp. 1987‐1992.

(31) 前川明弘, 三島直生, 畑中重光, 坪内徹朗. ポーラスジオポリマーコンクリートの乾燥収縮特性に関する基礎的研究.「建設分野におけるジオポリマー技術の現状と課題」に関するシンポジウム論文集. 2016, pp. 75-80.

(32) Ling, Yifeng, Wang, Kejin, Fu, Chuanqing. Shrinkage behavior of fly ash based geopolymer pastes with and without shrinkage reducing admixture. Cement and Concrete Composites. 2019, Vol. 98, pp. 74–82.

(33) 河尻留奈, 国枝稔, 上田尚史, 中村光. ジオポリマーの基礎物性と構造利用に関する基礎的研究. コンクリート工学年次論文集. 2011, Vol. 33, No. 1, pp. 1943-1948.

(34) ポンマハーサイパラミ, 五百蔵沙耶, 畑中重光. 断面修復材としてのジオポリマーの基礎物性に関する研究ー溶液粉体比および高炉スラグ微粉末の比表面積が及ぼす影響についてー. 日本建築学会大会学術 講演梗概集（関東）. pp. 1149-1150.

(35) 上原元樹, 佐藤隆恒, 小坂征雄, 山口正廣. 常温養生カリウム(K)型ジオポリマー左官用モルタルの調製と諸特性. コンクリート工学年次論文集. 2020, Vol. 42, No. 1, pp. 1780-1785.

(36) 王涛, 谷口修, 内藤英晴, 藤原浩巳. 常温硬化させたジオポリマーモルタルの基礎物性に関する検討. コンクリート工学年次論文集. 2020, Vol. 42, No. 1, pp. 1762-1767.

(37) 岡田朋久, 李柱国, 橋爪進, 永井伴英. フライアッシュと高炉スラグ微粉末を用いたジオポリマーコンクリートの性能に及ぼす収縮低減剤の影響に関する研究. コンクリート工学年次論文集. 2017, Vol. 39, No. 1, pp. 2029-2034.

(38) 中村丞吾, 新大軌, 宇城正貴, 島崎大樹. ジオポリマーにおける膨張材の水和反応に関する研究. コンクリート工学年次論文集. 2018, Vol. 40, No. 1, pp. 1833-1838.

(39) 束原実, 大木信洋, 上原元樹. 短繊維補強ジオポリマー短まくらぎの実用化に向けた基礎的検討. コンクリート工学年次論文集. 2015, Vol. 37, No. 1, pp. 1963-1968.

(40) 李柱国, 高垣内仁志, 杉原大祐, 李薛忠. 再生粗骨材を用いたジオポリマーコンクリートに関する実験的研究. コンクリート工学年次論文集. 2020, Vol. 42, No. 1, pp. 1798-1803.

(41) Hardjito, D., Wallah, SE, Sumajouw, DMJ, Rangan, BV. On the development of fly ash-based geopolymer concrete. ACI MATERIALS JOURNAL. 2004, Vol. 101, No. 6, pp. 467–472.

(42) Wallah, S. E., Rangan, B. V. LOW-CALCIUM FLY ASH-BASED GEOPOLYMER CONCRETE: LONG-TERM PROPERTIES.

(43) Wallah, Steenie. Creep Behaviour of Fly Ash-Based Geopolymer Concrete. Civil Engineering Dimension. 2010, Vol. 12.

(44) Sagoe-Crentsil, Kwesi, Brown, Trevor, Taylor, Alan. Drying shrinkage and creep performance of geopolymer concrete. Journal of Sustainable Cement-Based Materials. 2013, Vol. 2, No. 1, pp. 35–42.

(45) Castel, A., Foster, S. J., Ng, T., Sanjayan, J. G., Gilbert, R. I. Creep and drying shrinkage of a

blended slag and low calcium fly ash geopolymer Concrete. Materials and Structures. 2016, Vol. 49, No. 5, pp. 1619–1628.

(46) Gunasekera, C., Setunge, S., and Law, D. W. Creep and Drying Shrinkage of Different Fly-Ash-Based Geopolymers. ACI Materials Journal. 2019, Vol. 116, No. 1.

(47) Un, C. H., Sanjayan, J. G., San Nicolas, R., van Deventer, J. S. J. Predictions of long-term deflection of geopolymer concrete beams. Construction and Building Materials. 2015, Vol. 94, pp. 10–19.

(48) 南浩輔, 上原元樹, 梶田秀幸, 舟橋政司. ジオポリマーコンクリートの圧縮クリープに関する基礎的研究. コンクリート工学年次論文集. 2015, Vol. 37, No. 1, pp. 1969‐1974.

(49) 日本建築学会. 鉄筋コンクリート構造計算基準・同解説. 2018.

(50) 南浩輔, 白根勇二, 佐藤隆恒, 上原元樹. ケイ酸アルカリ溶液中のケイ素／アルカリ比がジオポリマーコンクリートの耐久性に及ぼす影響. コンクリート工学年次論文集. 2016, Vol. 38, No. 1, pp. 2331‐2336.

(51) 聶菁, 吉田有希, 木作友亮, 鈴木広也, 井川舜也. ジオポリマーコンクリート「セメノン」の開発. IHI 技報. 2024, Vol. 64, No. 2, pp. 67‐74.

(52) 寺本篤史, 宮治友也, 丸山一平, 鈴木雅博. 超高強度コンクリートの若材齢線膨張係数に関する研究. コンクリート工学年次論文集. 2007, Vol. 29, No. 1, pp. 633‐638.

CHAPTER 4. MICROSTRUCTURE OF GEOPOLYMER

4.1. Motivation

In the case of cement concrete, the desirable engineering characteristics of hardened concrete, such as strength, dimensional stability, and durability, are influenced not only by the proportion but also by the properties of the hydrated cement paste, which, in turn, depends on the microstructural features (i.e., the type, amount, and distribution of solids and voids)[(1)]. It can be said that the properties of cement concrete can be controlled by controlling the microstructure of the cement paste. The results of CHAPTER 2 and CHAPTER 3 suggest that the properties of geopolymer, including radio wave transparency and time-dependent deformation properties, are strongly influenced by microstructures such as pore structure, skeletal strength, and skeletal composition. Therefore, it is quite possible that the properties of geopolymer can also be controlled by controlling the microstructure. However, there have been few studies on the microstructure of geopolymer, and the relationship between mix proportions, production methods and microstructure, as well as the relationship between microstructure and properties, has not been fully clarified.

This chapter focuses on the microstructure formation mechanism within a fly ash-based geopolymer. Since the microstructure would strongly affect the properties of geopolymer, this study aims to clarify the microstructure formation mechanisms of the geopolymer and use these insights to improve the performance of the material by controlling parameters that directly change the final microstructure.

4.2. Literature review

4.2.1. Micro structure of geopolymer

The reaction mechanism and microstructure of geopolymer are totally different from these of cement. The interior of the hardened cement body has a Velcro-like structure of hydration products extending from the cement particles, while the interior of the geopolymer solidified body has a structure of alumina-silica powder particles solidified with an inorganic, irregularly shaped gel. This gel has been found to be amorphous, although its local structure is similar to that of a zeolite with a three-dimensional structure[(2)]. Zeolites are characterized by a three-dimensional structure in which they combine to form a "framework" like quartz, which is composed only of SiO_4 tetrahedra. However, Si^{4+} in some SiO_4 tetrahedra is replaced by aluminum ions (Al^{3+}), and the framework becomes negatively charged, and cations such as sodium ions (Na^+) and potassium ions (K^+) compensate for this. The structure consisting of a SiO_4 tetrahedral framework with Al substituting for Si and cations compensating for the negative charge is called an "aluminosilicate structure."[(3)] Geopolymer produced from powders with low calcium content, such as metakaolin and fly ash, are considered to have such aluminosilicate structures, but their atomic arrangement is less regular and they do not have a certain

long-period structure, so-called amorphous materials (**Figure 4-1**). This unique reaction product of geopolymer is called N-A-S-H (sodium aluminosilicate hydrate) in analogy to C-S-H (calcium silicate hydrate) in cement hydrates.

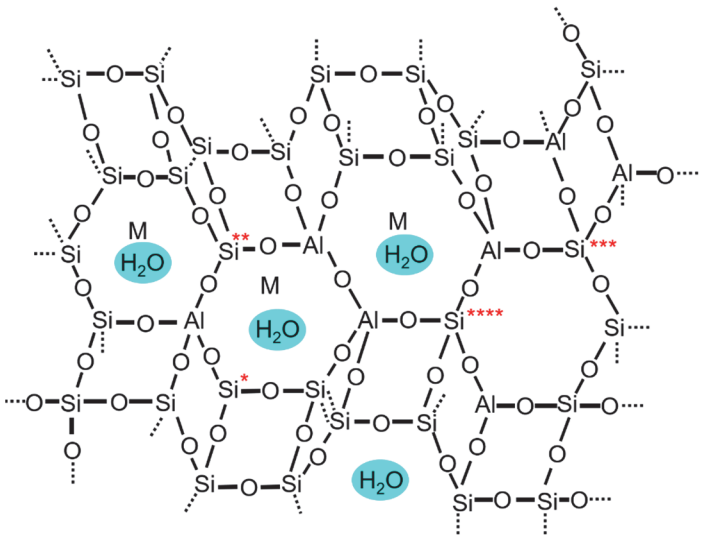

Figure 4-1 Schematic diagram of the structure of geopolymer (****: Q^4(4Al) by ^{29}Si-NMR, ***: Q^4(3Al), **: Q^4(2Al), *: Q^4(1Al), Unlabeled: Q^4(0Al))

4.2.2. Raman microscopy

Since the reaction product of geopolymer (N-A-S-H) is amorphous, X-ray diffraction, a common method for crystal structure analysis, does not provide much information. Therefore, in many cases, geopolymer is described by the local structure around Si or Al atoms by solid-state nuclear magnetic resonance (NMR) measurements of ^{29}Si or ^{27}Al. The schematic diagram of the condensed structure of SiO_4 tetrahedron in ^{29}Si-NMR spectrum is shown in **Figure 4-2**. ^{29}Si-NMR peak is represented by Q^n, where Q represents SiO_4 tetrahedron and n represents the degree of condensation, indicating that n oxygen atoms are shared by neighboring T (Si or Al). Three-dimensional structures such as zeolite or quartz in which all four oxygen atoms are shared are represented by Q^4. The main geopolymer reaction product from metakaolin or fly ash (N-A-S-H) is considered to have this Q^4 structure[4].

Raman spectroscopy is considered to be one of the effective methods to clarify the detailed reaction mechanism of geopolymer. Raman spectroscopy is a spectroscopic method for evaluating materials using Raman scattered light discovered by Raman[5]. When monochromatic radiation with a wavenumber $\tilde{\nu}_0$ is incident upon a system, the majority of the radiation is transmitted without modification. However, some of the radiation undergoes scattering. Analysis of the scattered radiation reveals not only the wavenumber $\tilde{\nu}_0$ associated with the incident radiation but also additional wavenumbers of the form $\tilde{\nu}' = \tilde{\nu}_0 + \tilde{\nu}_M$. In molecular systems, the wavenumbers $\tilde{\nu}_M$ are primarily

associated with transitions between rotational, vibrational, and electronic energy levels. This scattering, which results in a change in wavenumber, is referred to as Raman scattering[6, 7] (**Figure 4-3**).

The modified frequencies observed in Raman scattering can be explained by energy transfer between the incident radiation and the system. When the system interacts with radiation of wavenumber $\tilde{\nu}_0$, an upward transition occurs from a lower energy level E_1 to a higher energy level E_2, requiring an energy difference $\Delta E = E_2 - E_1$. This energy difference ΔE can be expressed in terms of a wavenumber $\tilde{\nu}_M$ associated with the two energy levels:

$$\Delta E = hc\tilde{\nu}_M \qquad (4-1)$$

The energy required for this transition is supplied by the absorption of one photon of the incident radiation, with energy $hc\tilde{\nu}_0$, and the simultaneous emission of a photon with a reduced energy $hc(\tilde{\nu}_0 - \tilde{\nu}_M)$. This results in the scattering of radiation at a lower wavenumber $\tilde{\nu}_0 - \tilde{\nu}_M$. Conversely, the interaction may induce a downward transition from a higher energy level E_2 to a lower energy level E_1, releasing an energy:

$$E_2 - E_1 = hc\tilde{\nu}_M \qquad (4-2)$$

In this case, a photon of the incident radiation is absorbed with energy $hc\tilde{\nu}_0$, and a photon of higher energy $hc(\tilde{\nu}_0 + \tilde{\nu}_M)$ is emitted, leading to scattering at a higher wavenumber $\tilde{\nu}_0 + \tilde{\nu}_M$.

For Rayleigh scattering, the energy state of the system remains unchanged. The system, however, participates in the scattering process by absorbing a photon with energy $hc\tilde{\nu}_0$ and simultaneously re-emitting a photon of identical energy. This results in scattering with no change in wavenumber, $\tilde{\nu}_0$.

In the context of Raman scattering, the characteristic feature of a Raman band is not its absolute wavenumber $\tilde{\nu}' = \tilde{\nu}_0 \pm \tilde{\nu}_M$, but rather the magnitude of the wavenumber shift $\tilde{\nu}_M$ from the incident wavenumber. These shifts are referred to as Raman wavenumbers. To distinguish between Stokes and anti-Stokes Raman scattering, the wavenumber shift $\Delta\tilde{\nu}$ is defined as positive for Stokes scattering and negative for anti-Stokes scattering, such that $\Delta\tilde{\nu} = \tilde{\nu}_0 + \tilde{\nu}'$ (**Figure 4-4**).

The relative intensity of anti-Stokes Raman scattering decreases rapidly with increasing wavenumber shift. This is because anti-Stokes scattering involves transitions from a higher populated energy state to a lower energy state, which are inherently less probable.

In Raman spectroscopy, Stokes scattering light, which has higher intensity, is typically used for analysis. A monochromatic laser serves as the excitation light source, and the scattered light is dispersed using a diffraction grating to obtain a Raman spectrum. The wavelength difference between the incident light and the scattered light corresponds to the energy of molecular vibrations inherent to the material. As a result, materials with different molecular structures produce Raman scattered light

with distinct wavelengths, leading to unique Raman spectra. Using Raman spectra, various physical properties, such as stress, temperature, electrical characteristics, orientation, and crystallinity, can be examined. Specifically, peak positions provide information about chemical bonds, the overall spectral shape reveals molecular structure and differences in crystal structures, peak widths at half-maximum indicate variations in crystallinity, and peak shifts offer insights into stress or strain[6-8].

The advantages of Raman spectroscopy include the ability to analyze various forms of materials such as solids, liquids, and gases, the ease of analyzing samples containing water because they are not easily affected by moisture, and the ability to make *in situ* measurements because no vacuum drying or other sample preparation is required[6-8].

In addition, the use of confocal Raman microscopy (CRM) allows high-resolution imaging of the two- and three-dimensional chemical composition distribution of samples, which, when combined with *in situ* measurements, enables real-time reaction monitoring[8-10]. A confocal Raman imaging optical system in CRM is an optical setup designed to efficiently detect scattered light from a single point on a sample by placing a pinhole at the confocal position corresponding to that point (**Figure 4-5**). During imaging, signals are collected from each point either by moving the sample with a stage scan or by scanning the focal position across the sample using a galvanometric mirror or similar device. The key feature of the confocal Raman imaging optical system is its spatial resolution. The spatial resolution in a confocal optical system is determined by the numerical aperture (N.A.) of the objective lens, the wavelength of light, and the size of the pinhole at the confocal position. The spatial resolution defined by the N.A. of the objective lens and the wavelength is typically described using the Rayleigh criterion, which refers to the minimum resolvable distance between two bright points on the sample.

CRM is becoming a popular technique to characterize the cement hydration process[11-18]. Garg et al.[14, 16–18] have conducted over a decade of research using CRM for microscale analysis to elucidate the distribution of various phases in cementitious materials and their temporal changes. They have identified and characterized more than ten phases, including Alite and Belite, in anhydrous cement and hardened cement paste, detailing their distribution, morphology, and abundance. Their research outcomes enable a new dimension of physical and chemical particle characterization and pave the way for future applications of Raman imaging on other heterogeneous, powdered systems. Loh et al.[15] were the first to visualize the growth of hydration products at submicron resolution and its direct relationship to setting, confirming that setting is indeed a percolation process. The proposed time space-resolved characterization method can map and quantitatively analyze the heterogeneous reaction of the cementitious colloidal system and thus provide potential application value in the field of cement chemistry and materials design more broadly.

However, CRM is not commonly used for geopolymer, because the Raman spectra of the reaction products of low-calcium geopolymer such as fly ash-based or metakaolin-based geopolymer have not been clarified. Although several studies have examined the Raman spectra of solidified geopolymer[19,

[20], it is very difficult to extract the Raman spectra of the geopolymer reaction products because the amorphous structure of geopolymer reaction products makes their Raman spectral signals weak and obscured by the strong signals of other components such as hydrates. It goes without saying that this has also been a significant obstacle in the *in situ* observation of geopolymer. To date, there are no reported cases of visualizing the growth process of reaction products in geopolymer through *in situ* observation using CRM.

Since the main geopolymer reaction product from metakaolin or fly ash (N-A-S-H) is considered to have Q^4 structure, the Raman spectrum of geopolymer reaction product is expected to be similar to those of Q^4 aluminosilicates such as zeolite and quartz. Various studies have been conducted on the Raman spectra of aluminosilicates[21-23]. Although the peak intensity varies depending on the Na_2O, Al_2O_3, and SiO_2 content, it has been found that peaks indicating O-bending motions in Si-O-Si rings sharing three or four SiO_4 tetrahedra appear around 500-600 cm^{-1}, and that peaks indicating stretching motions in SiO_4 tetrahedra with 4-n nonbridging oxygens appear around 950 cm^{-1} (Q^1, Q^2) and 1100 cm^{-1} (Q^3, Q^4)[23]. Therefore, the Raman spectrum of geopolymer reaction product is expected to have peaks around 500-600 cm^{-1} and 1100 cm^{-1}.

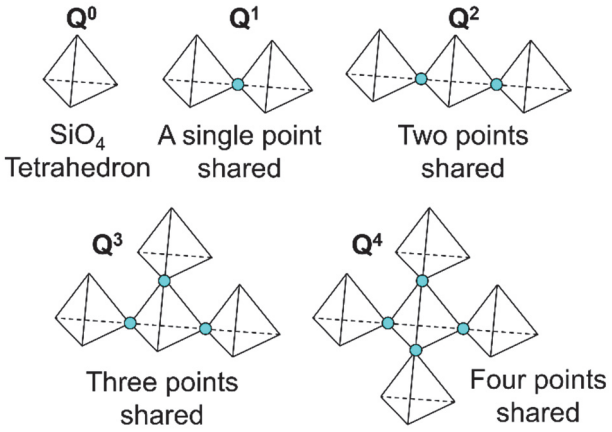

Figure 4-2 Schematic diagram of the condensed structure of SiO_4 tetrahedron in ^{29}Si-NMR spectrum

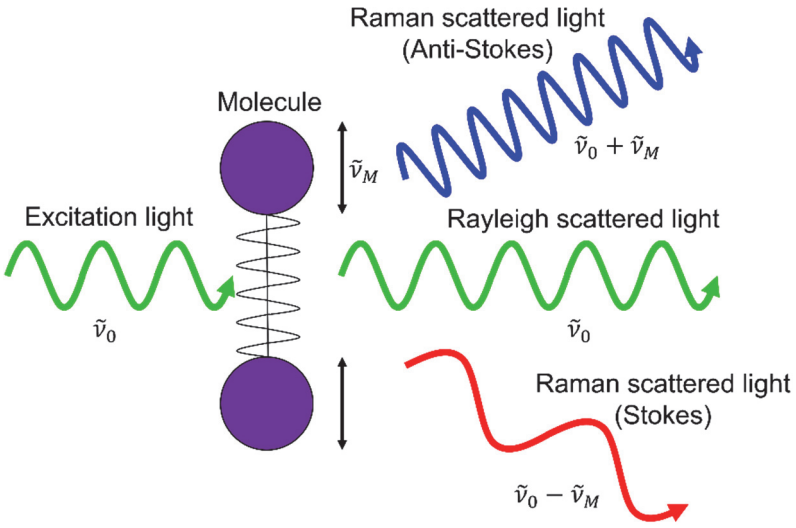

Figure 4-3 Schematic diagram of Raman scattering

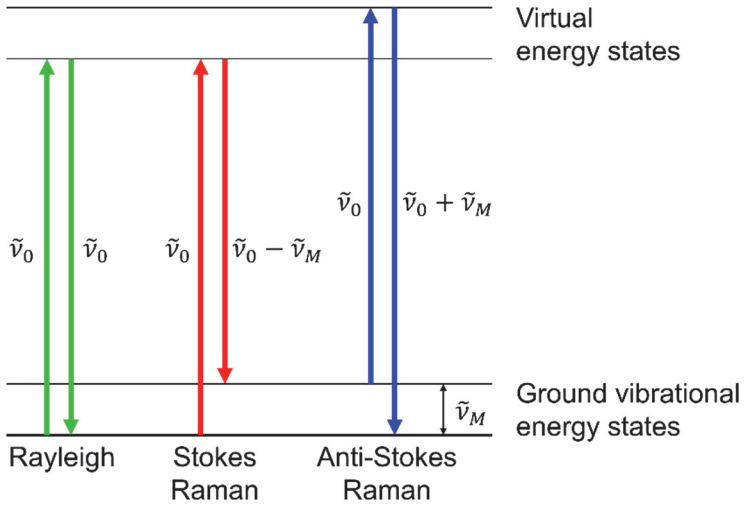

Figure 4-4 Schematic diagram of an energy transfer model of Rayleigh scattering, Stokes Raman and anti-Stokes Raman scattering.

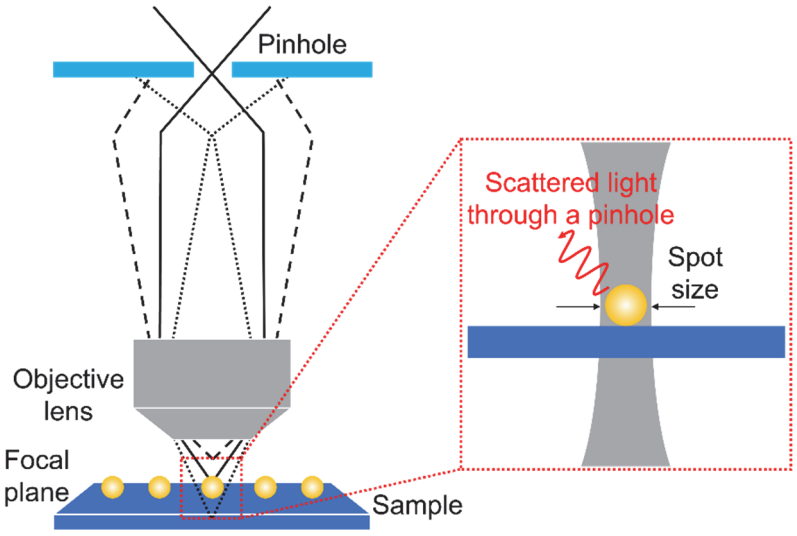

Figure 4-5 Schematic diagram of confocal Raman imaging optical system

4.3. Methodology

4.3.1. Experiment method

In order to clarify the growth process of the reaction products in the geopolymer, the original experiment system for *in situ* Raman imaging while heating the sample was built (**Figure 4-6** (a)). The heating stage, which consists of a 3D-printed base and a steel plate with a heating film attached (**Figure 4-6** (b)), was installed on the stage of a CRM system (Alpha 300RA, WITec, Germany). The heating film was powered by the electric current from an adjustable power supply. The prepared samples were fixed on the steel plate by magnetic clips (**Figure 4-6** (b)).

The geopolymer sample was prepared using the materials shown in **Table 4-1**, and the specific properties of the materials are shown in Table 4-2, **Table 4-3**, and **Table 4-4**. Here, the class F fly ash used to form the geopolymers was collected from the Salt River Materials group in Pheonix, Arizona. Fly ash is a byproduct of the coal combustion process during power generation and is often used as an additive in OPC concretes as a pozzolanic material due to the high silica content. The XRF results collected from the raw precursor powder is shown below in **Table 2.** Sodium silicate is produced by melting high purity sand with sodium carbonate (soda ash) in high temperature furnaces. The resulting product is a water-soluble silicate powder that is known as water glass or sodium silicate solution once it is dissolved in water. Sodium silicate solution is chemically comprised of a weight ratio of silica to sodium oxide dissolved in water. The sodium silicate used in this study has a weight ratio of 3.22 (SiO_2:Na_2O), which breaks down as ~28.7% silica (SiO_2) to ~8.9% sodium oxide (Na_2O), and that translates into a solution that is approximately 37.5% sodium silicate by weight in water. The mix proportion shown in **Table 4-5**. In the mix proportion, the liquid to powder volume ratio (L/P), the alkali to total water ratio (A/W), and the silica to alkali ratio (Si/A) were set to the same value used in

the common geopolymer tests proposed by the research subcommittee for promoting the practical application of geopolymer technology in the civil engineering field in the Japan Society of Civil Engineers (JSCE)[24].

To validate the original experiment and analysis method, a cement paste sample was also prepared using Portland cement blended with Type I and II. The L/P (volume ratio) was set to the same value (0.9) as the geopolymer sample. This gives a W/C (mass ratio) of 0.28. Because of the low W/C, a superplasticizer (PLASTOL 6400, Euclid Chemical) was added for 0.5% of the cement mass to ensure the workability. The experiment for the cement paste samples were conducted at room temperature without the heating stage to avoid overly fast reaction speed.

The day before the experiment, the alkaline solution was mixed and placed in a sealed container. Before mixing, the power supply was turned on, and the voltage was adjusted so the steel plate was heated to a constant 60°C. The temperature was maintained at 60°C throughout the experiment for the geopolymer sample in order to accelerate the geopolymer reaction. After confirming that the surface temperature of the steel plate reached 60°C, the mixing was started. The powder was put into a beaker, in which the solution was added and mixed for 1 minute using a glass rod. The mixed paste was put on a glass slide using a needle. The amount of paste on the glass slide should be as small as possible to reduce the volume change of the paste. After that, the paste was covered with cover glass and sealed with aluminum tapes (**Figure 4-6** (b)). The prepared sample was fixed on the steel plate by magnetic clips.

The CRM system was manipulated to focus on the surface of the paste. After the scan area was determined, the brightness was adjusted and the image was re-focused. After that, the first scan started using the settings shown in **Table 4-6**. In this study, the first scan started 20 minutes after mixing. The same scans were conducted 1, 2, 3, 4, 5, 8, and 24 hours after mixing. To maintain the focal plane as consistent as possible across all scans, optical focus was carefully adjusted before initiating each scan.

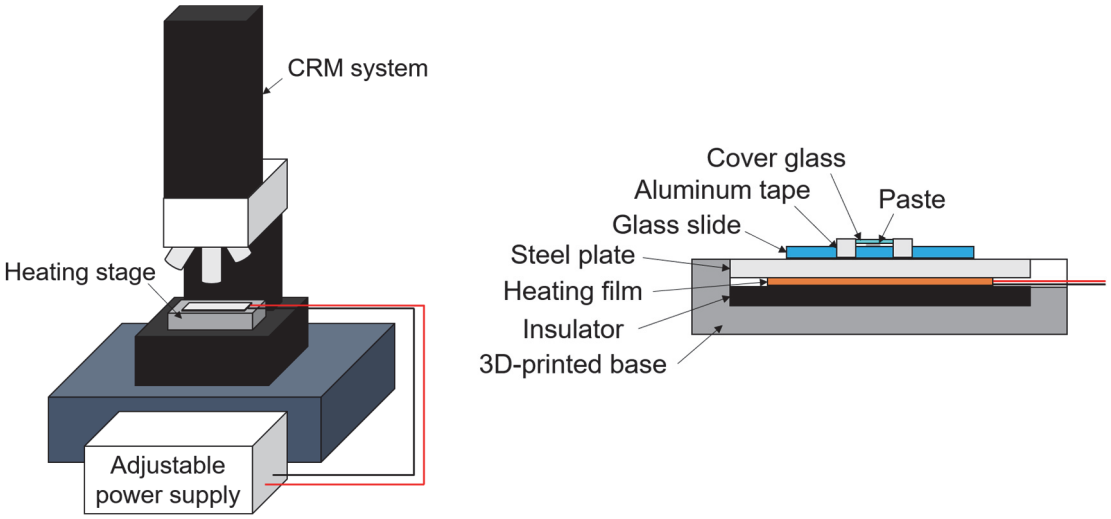

(a) (b)

Figure 4-6 Schematic diagrams of the experimental setup. (a) Experiment system. (b) Cross-section view of the heating stage and the sample preparation

Table 4-1 Materials for the geopolymer sample

Type	Name	Symbol	Ingredients and Properties
Active filler (P)	Fly ash	FA	ASTM Class F, Density 2.35g/cm^3
Alkaline solution (L)	Sodium silicate solution	SS	Silicon dioxide content: 28.7%
	Sodium hydroxide	SH	Pellets, Purity 97%
	Water	LW	Deionized water

Table 4-2 Elemental composition of fly ash as measured by XRF

Oxide	Percentage (%)
SiO_2	56.79
Al_2O_3	17.07
Fe_2O_3	4.17
CaO	8.16
MgO	1.98
SO_3	0.57
Na_2O	2.66
K_2O	2.11
TiO_2	0.78
P_2O_5	0.39
SrO	0.172
Mn_2O_3	0.036
Cr_2O_3	0.011
ZnO	0.01
LOI	4.927
Total oxides	99.83

Table 4-3 Physical and chemical properties of sodium silicate solution

Sodium silicate	37% Wt.% (28% silica + 9% sodium oxide)
Water	63% Wt.%
Appearance	Thick liquid
Color	Clear to murky white
Odor	Odorless or musty odor
pH	Approximately 11.3
Specific gravity	1.39 g/cm^3 (20°C), 41° BÈ, 11.62 lbs/gal
Solubility in water	Miscible

Table 4-4 Specification test results of sodium hydroxide

Calcium	0.005%
Chloride	= 0.005%
Heavy metals	= 0.002%
Iron	= 0.001%
Magnesium	= 0.002%
Mercury	= 0.1 ppm
Nickel	= 0.001%
Nitrogen compounds	= 0.001%
Phosphate	= 0.001%
Potassium	= 0.001%
Purity	= 97%
Sodium carbonate	= 1%
Sulfate	= 0.003%

Table 4-5 Mix proportions for the geopolymer sample

Unit volume(kg/m^3)				A/W	Si/A	L/P
P	L					
FA	SS	SH	LW			
1237	412	65	148	0.125	0.700	0.9

Table 4-6 Setting for the Raman system

Magnification	50× (N.A. = 0.75) (Zeiss EC Epiplan)
Laser	532nm, 3.00mW
Spectrograph	G2: 600 g/mm, BLZ 500.00 nm, Centre Wavenumber: 2400.0 1/cm
Integration Time	0.5 s
Image Scan	Scan area: 20×20 µm Points per Line: 50, Lines per Image: 50, Layers per Scan: 1

4.3.2. Analysis method

WITec Project SIX software was used for data analysis and visualization. The data was first processed with cosmic ray removal (Filter size: 2, Dynamic factor: 8) and a background subtraction was applied based on the shape (Shape size: 100).

In this study, the new analysis method was proposed for extracting the Raman spectrum and *in situ* mapping of reaction products of geopolymer which could not be obtained by ordinary Raman spectroscopy. First, the average Raman spectra of each mapped area was obtained by averaging the

CCD counts of each wavenumber at every point in the scanned area (50×50 points). If an increase in intensity is observed in the average spectra, the increase is considered to be due to the growth of reaction products. Therefore, it can be said that the difference between the two spectra obtained at the first scan (20m) and the last scan (24h) represents the spectrum of reaction products produced between the first and last scan. The target spectrum was obtained by subtracting the average spectra of the 20m scan and the 24h scan, using Graph Demixer function embedded in WITec Project SIX software. Only the wavenumber range where the intensity increased within the spectrum was extracted, using the Repair function embedded in WITec Project SIX software. For the remaining ranges, the intensity was set to a constant value equal to the intensity at the boundaries of the extracted range. Finally, the peak intensity of the extracted spectrum was measured at each point within the scan area, and the peak intensity was represented as a color, resulting in a Raman image. The Raman images at each time step were output with a consistent color scale.

4.4. Results and discussions

4.4.1. Cement paste sample

To confirm the validity of the proposed analysis method, results of the cement paste sample are shown. The average spectrum at each time step is shown in **Figure 4-7**. An increase in the intensity of strong peaks was found at around 1000 cm^{-1}. The cropped spectrum from around 400 cm^{-1} to around 1200 cm^{-1} in the difference spectrum between the two spectra obtained at the first scan (20m) and the last scan (24h) is shown in **Figure 4-8**. The cropped spectrum includes some strong peaks of $\upsilon_1[SO_4^{2-}]$ bands[12], such as 980 cm^{-1}, 991 cm^{-1}, 1003 cm^{-1}. These peaks are considered to represent monosulfate, ettringite, and gypsum, respectively[12, 15]. Since ettringite and monosulfate are the reaction products from the hydration reaction of cement and water, it can be said that the proposed analysis method can detect the reaction products properly.

Obtained distributions at each time step by the Raman imaging using the cropped spectrum are shown in **Figure 4-9**. The brighter the color, the higher the concentration of the component, and black areas are considered to be pores. The distributions show that the bright area expands over time, especially between the first scan (20m) and the second scan (1h). To clarify the extent to which the distribution has expanded, an overlay image of distributions at the second scan (1h) and the last scan (24h) was generated (**Figure 4-10)**. Since the sample moved slightly over time, the overlaying positions were adjusted so that the positions of the pores coincided. The overlay image shows that the reaction products grew up to approximately 5.6 μm and are filling the pores, and that the reaction products have a complex shape, which in turn complicates the pore shape. This result indicates that the proposed analysis can visualize the distribution of reaction products and its changes over time.

In addition, the cropped spectrum was decomposed into three spectra, each with one strong peak (**Figure 4-11**) by “Repair” tool, and the results of mapping the distribution of each component and the

combined bitmap are shown in **Figure 4-12**. These mapping results show that the distributions shown in **Figure 4-9** are primarily due to components exhibiting peaks at 980 cm^{-1} and 1003 cm^{-1}, and these two distributions are almost identical. This result indicates that the 980 cm^{-1} and 1003 cm^{-1} peaks may represent a single component rather than separate components. Belite (C_2S) is the most likely compound to contain these two peaks[12], but belite is not a reaction product, but a compound originally included in the cement. Therefore, if this compound is belite, two peaks should appear in the first scan, so it is more natural to assume that it is some kind of reaction product. In this paper, the two peaks are treated as indicating different compounds, monosulfate and gypsum, but further investigation is needed to identify this compound with high accuracy.

Furthermore, the average spectrum at each time step and the difference spectrum obtained in this study don't include the peaks representing main reaction products such as calcium silicate hydrate (C-S-H). C-S-H is identified by a strong peak around at 3618 cm^{-1} that indicates the OH stretching band in $Ca(OH)_2$[12, 15]. Using the conventional analysis method, a sharp peak around at 3618 cm^{-1} was detected, but the peak intensity was smaller than the three peaks around at 1000 cm^{-1} and the distribution was also smaller, so it is assumed that it did not appear in the total average spectrum of the scan area. Further study is required to enable extraction of spectra of compounds with weak peak intensities.

Thus, although there are several points that require further study, it is possible to extract spectra of some reaction products and visualize their distribution by using the proposed method.

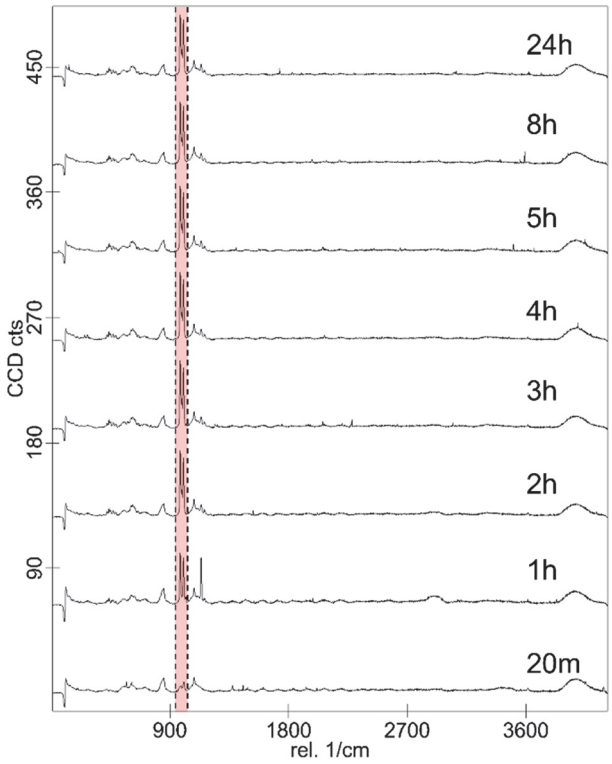

Figure 4-7 Average spectrum at each time step (Cement paste sample)

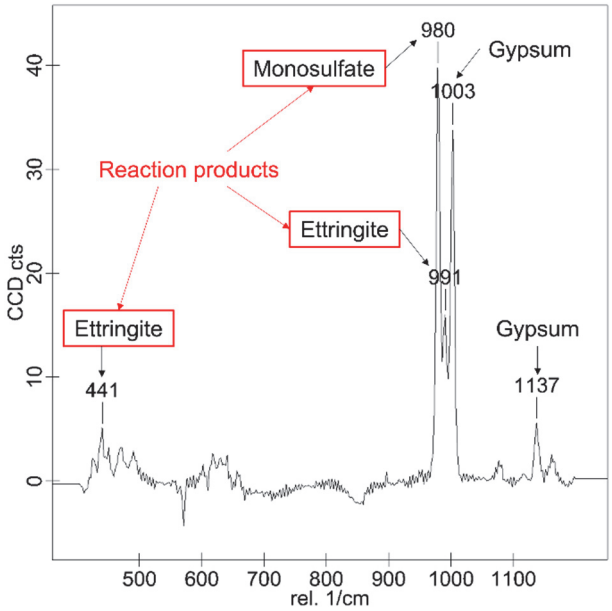

Figure 4-8 Cropped spectrum from the difference between the two spectra obtained at the first scan (20m) and the last scan (24h) (Cement paste sample)

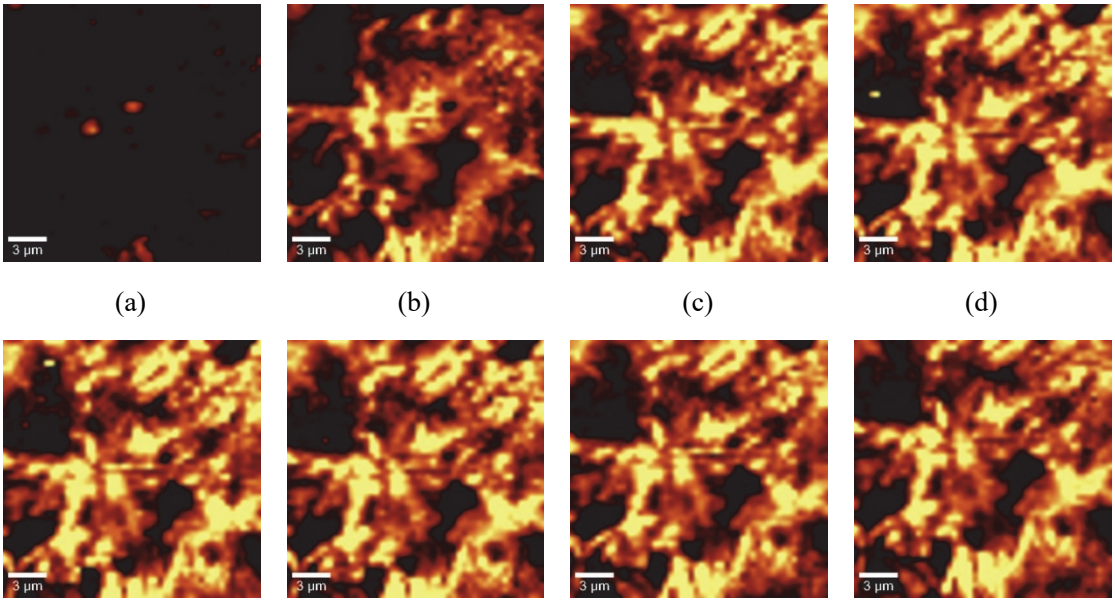

Figure 4-9 Distributions of reaction products at each time step (Cement paste sample), (a) 20 minutes after mixing, (b) 1 hour after mixing, (c) 2 hours after mixing, (d) 3 hours after mixing, (e) 4 hours after mixing, (f) 5 hours after mixing, (g) 8 hours after mixing, (h) 24 hours after mixing

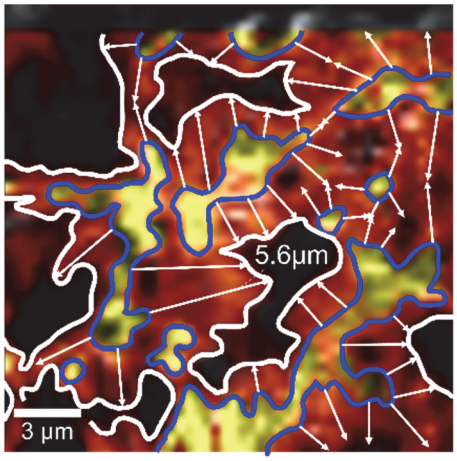

Figure 4-10 Overlayed image of distributions at the second scan (1h) and the last scan (24h) (Cement paste sample)

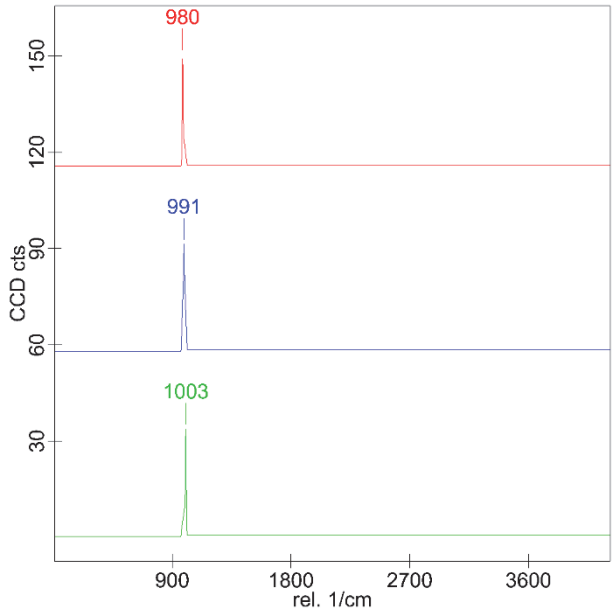

Figure 4-11 Decomposed spectra from the cropped spectrum

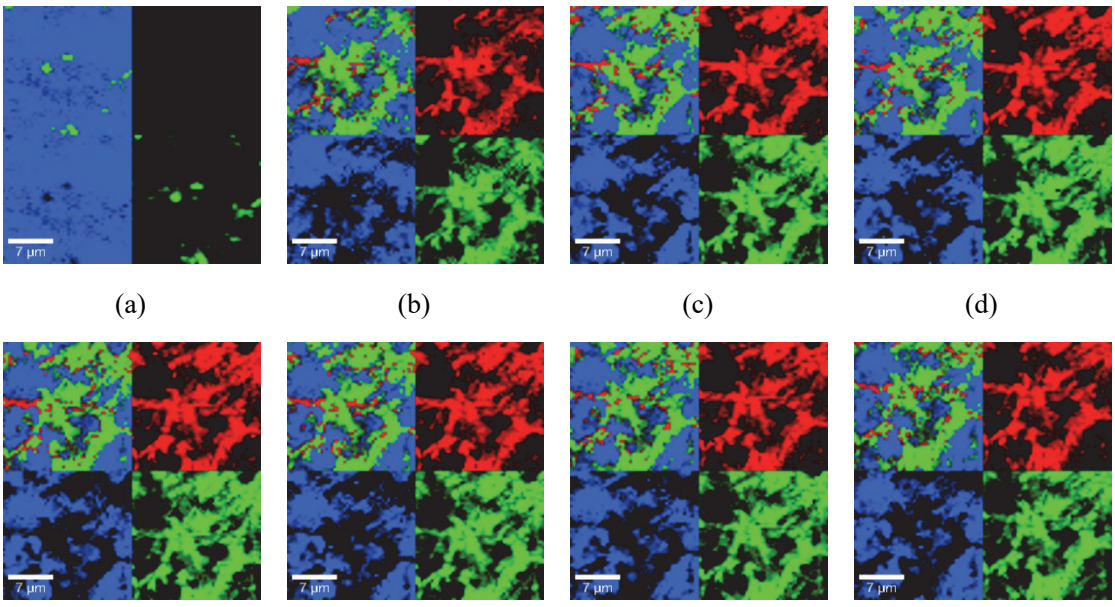

(a) (b) (c) (d)

(e) (f) (g) (h)

Figure 4-12 Distributions of each component and the combined bitmap at each time step (Red: 980cm^{-1}, Blue: 991cm^{-1}, Green: 1003cm^{-1}), (a) 20 minutes after mixing, (b) 1 hour after mixing, (c) 2 hours after mixing, (d) 3 hours after mixing, (e) 4 hours after mixing, (f) 5 hours after mixing, (g) 8 hours after mixing, (h) 24 hours after mixing

4.4.2. Geopolymer sample

The average spectrum at each time step is shown in **Figure 4-13**. An increase in the intensity of

the round peaks at around 500-600 cm^{-1} and around 1100 cm^{-1} was found as the material cured. The cropped spectrum from around 500 cm^{-1} to around 1200 cm^{-1} in the difference spectrum between the two spectra obtained at the first scan (20m) and the last scan (24h) is shown in **Figure 4-14**. The cropped spectrum includes round peaks at around 500-600 cm^{-1} and around 1100 cm^{-1}, indicating O-bending motions in Si-O-Si rings sharing three or four SiO_4 tetrahedra and stretching motions in SiO_4 tetrahedra (Q^3, Q^4) with 4-n nonbridging oxygens, respectively. Since the main geopolymer reaction product from metakaolin or fly ash (N-A-S-H) is considered to be Q^4 structure, it can be said that this spectrum correctly represents the geopolymer reaction product. A small peak at around 1000 cm^{-1} is also observed, which represents stretching motions in SiO_4 tetrahedra (Q^1, Q^2) with 4-n nonbridging oxygens, and is considered to be derived from C-S(A)-H formed by the reaction of alkali with calcium components slightly contained in the fly ash. The cropped spectra shown in **Figure 4-14** shows distinct peaks not fully expressed in the reference spectra collected from the bulk fly ash. In the base fly ash, the major peaks were found to be quartz, albite, and sanidine with each reference shown in **Figure 4-15**. In the cropped spectra the peaks are also in the same silicate regions but do not contain all the fingerprint peaks that allow for a positive identification of a crystalline phase.

Obtained distribution at each time step by the Raman imaging using the cropped spectrum is shown in **Figure 4-16**. The distributions show that the bright area expands over time. Furthermore, it can be observed that the areas with colors closer to yellow within the bright regions expand over time, especially between the first scan (20m) and the second scan (1h). In these Raman images, the brighter the color, or in other words, the closer the color is to yellow, the higher the peak intensity. This indicates that, in addition to the growth of reaction products as the reaction progresses, the framework within the products is becoming more densely structured.

An overlay image of the distributions at the first scan (20m) and the last scan (24h) is shown in **Figure 4-17**. Since the sample moved slightly over time, the overlaying positions were adjusted so that the positions of the pores coincided as same as the cement paste sample. The overlay image shows that the reaction products grew up to approximately 5.8 μm and are filling the pores as same as the cement paste sample, but the structure of the reaction products and pores seem quite different from those of the cement paste sample as seen in Figure 4-7 and **Figure 4-8**. In the cement paste sample, needle-like reaction products extend in different directions and appear to form a three-dimensional microstructure, while in the geopolymer sample, the reaction proceeds uniformly and appears to form a flat amorphous microstructure. In literature this distinction between morphology can be seen using electron microscopy (SEM), where at early ages OPC forms needle-like structures that densify overtime while fly ash tends to form an amorphous mass with unreacted material trapped within the matrix[25, 26]. In the Raman mapping results a higher degree of crystallinity and spectral resolution can be seen in areas with high intensity well-defined peaks. Between the two materials the reaction products of the OPC had higher peak intensities compared to the geopolymer samples. This could be

due to the geopolymer reaction products behaving as a continuous amorphous gel phase without a specific crystalline network, while the cement hydration reaction products exist in several phases with different crystal structures and morphologies. The microstructure of a geopolymer, especially the pore structure created by the gaps between reaction products, is simpler than that of cement, and many pores of similar size are expected to exist as shown in Sub-section 3.4.5. The nano pores (2nm-100nm) in geopolymer have been shown to be the interstitial spaces left between clusters of granular aluminosilicate gel particles[27, 28]. It is also clear that the pores in geopolymer tend to be concentrated within these nano pores[29]. It can be said that the results are consistent with these known facts. Therefore, the obtained results capture the known microstructural characteristics of both cement paste and geopolymer, demonstrating that the proposed method accurately visualized the distribution and growth of reaction products in geopolymer.

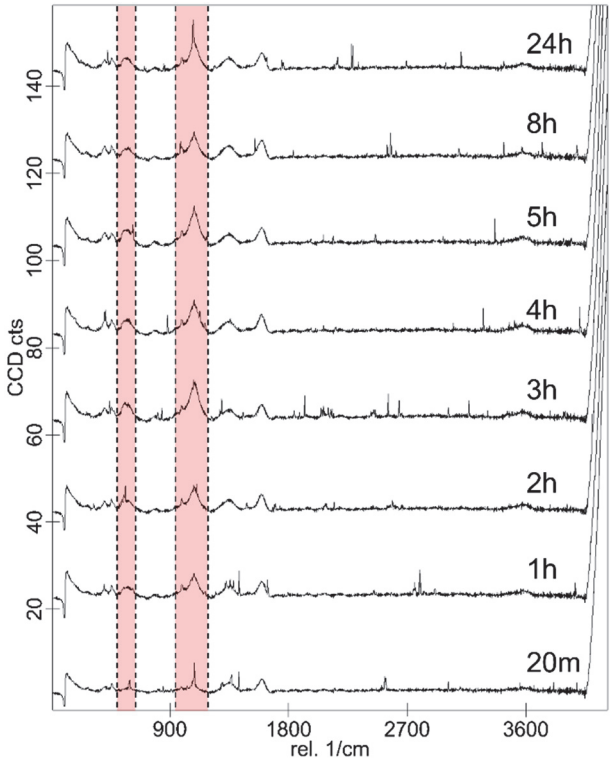

Figure 4-13 Average spectrum at each time step (Geopolymer sample)

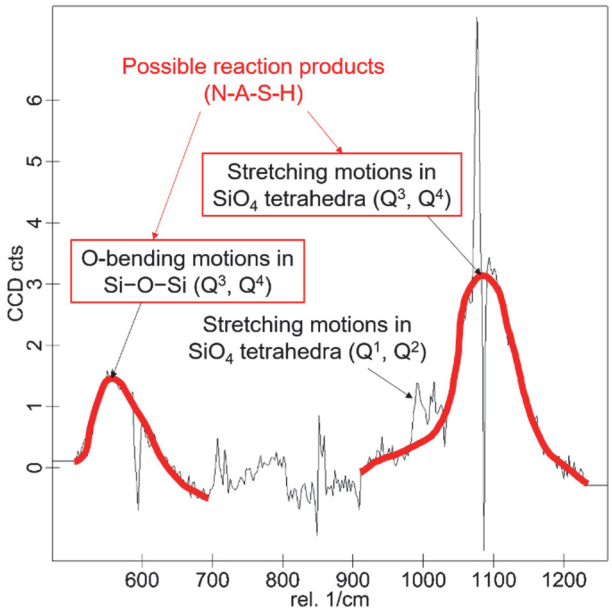

Figure 4-14 Cropped spectrum from the difference between the two spectra obtained at the first scan (20m) and the last scan (24h) (Geopolymer sample)

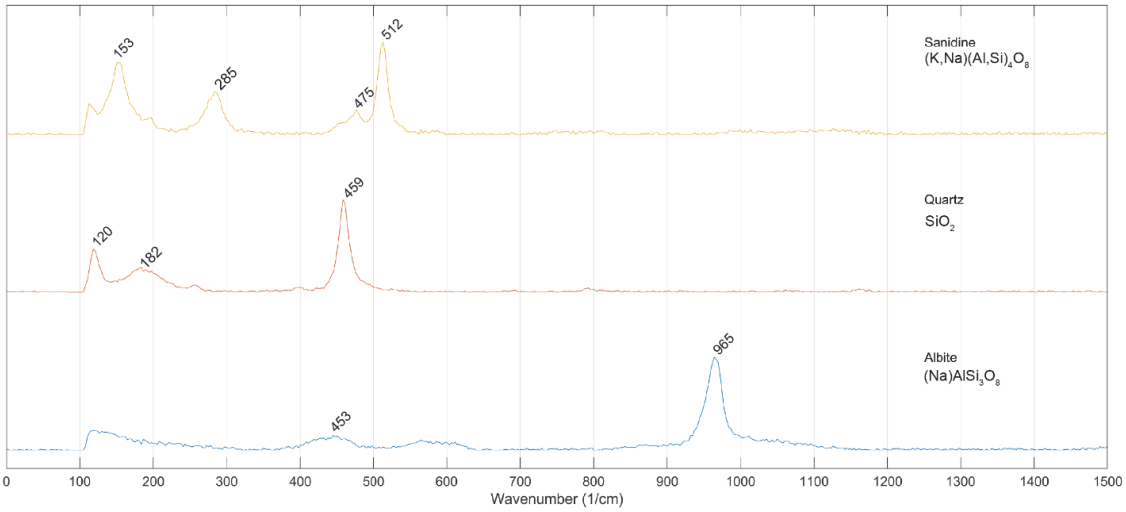

Figure 4-15 Reference Raman spectra collected from the raw fly ash before mixing with the activation solution

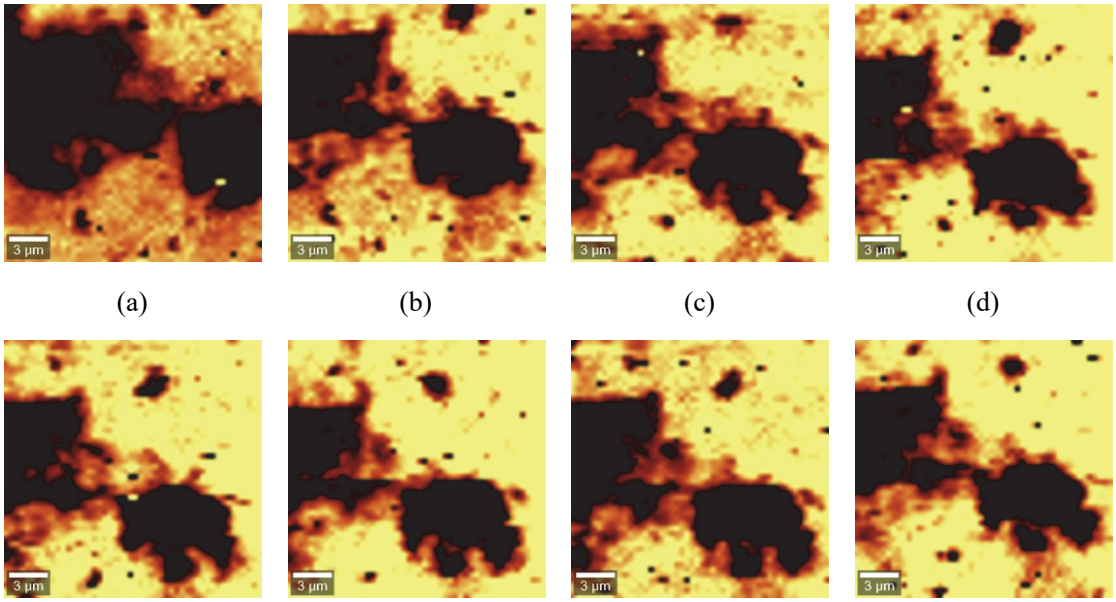

Figure 4-16 Distributions of reaction products at each time step (Geopolymer sample), (a) 20 minutes after mixing, (b) 1 hour after mixing, (c) 2 hours after mixing, (d) 3 hours after mixing, (e) 4 hours after mixing, (f) 5 hours after mixing, (g) 8 hours after mixing, (h) 24 hours after mixing

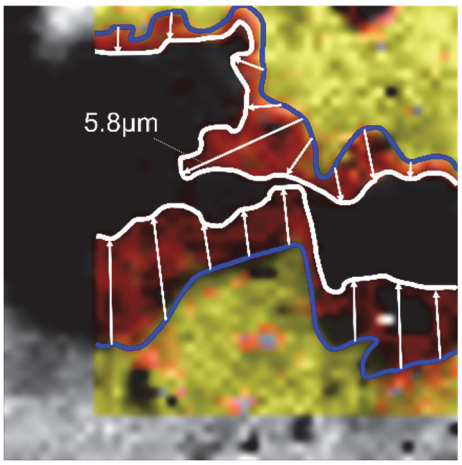

Figure 4-17 Overlayed image of distributions at the first scan (20m) and the last scan (24h) (Geopolymer sample)

4.5. Future prospects

The proposed experiment and analysis methods are very useful to clarify the differences in the microstructure formation process of geopolymer depending on mix proportions and production methods, and can promote greater use of geopolymer. Furthermore, these methods are considered to be very useful for the *in situ* analysis not only of geopolymer but also of materials for which Raman

spectra are unknown. However, the proposed method has several points that need improvement, such as the fact that it is more difficult to identify compounds than conventional Raman analysis, and the fact that detection is difficult when the peak intensity is weak. In addition, the volume of the paste changes over time, resulting in subtle changes in the height of the surface of the paste to be observed. Although the height of the lens is adjusted and optically focused at each time step so that the same surface can be observed, it is possible that the same surface is not observed completely. Further studies are needed to improve the accuracy of this method.

Furthermore, it is necessary to collect a lot of data under various conditions including low water-to-powder ratio (W/P) mix and to clarify the differences in shape and growth speed of reaction products in order to systematize the microstructure formation process and to control the microstructure of geopolymer. Moreover, it is expected that more detailed relationships between microstructure and macro properties can be elucidated by separating spectra and clarifying the distribution of each compound, as in cement paste, and by clarifying the differences in their distribution depending on mix proportions and curing conditions.

4.6. Concluding remarks

The following are the findings obtained from the study on the microstructure formation mechanism of geopolymer.

(1) The growth process of reaction products (N-A-S-H) in geopolymer was visualized for the first time using CRM.

(2) To apply CRM to geopolymer, the previously unknown spectrum of reaction products was defined as the difference between the average spectrum of the scanned area immediately after mixing and that measured 24 hours later. This definition enabled the acquisition of a reliable Raman spectrum for the geopolymer reaction product (N-A-S-H), making *in situ* Raman imaging feasible.

(3) The obtained Raman images captured the planar expansion of geopolymer reaction products over time, revealing that the microstructure of geopolymer differs significantly from that of cement paste.

(4) The observed characteristics of the geopolymer's microstructure generally align with previous findings, demonstrating that the proposed method accurately extracts the distribution of geopolymer reaction products.

(5) The proposed method represents a significant contribution to elucidating the characteristics of geopolymer and establishing methods for its control, ultimately supporting the broader application of geopolymer materials. Furthermore, it holds potential for application in other fields.

(6) It is necessary to improve the accuracy of proposed methods and to collect a lot of data under various conditions, in order to systematize the microstructure formation process and to control

the microstructure of geopolymer.

References

(1) Mehta, P. K., Monteiro, P. J. M. Concrete: Microstructure, Properties, and Materials. 4th Edition, New York, McGraw-Hill Education, 2014, ISBN978-0-07-179787-0. https://www.accessengineeringlibrary.com/content/book/9780071797870.

(2) Davidovits, J. PROPERTIES OF GEOPOLYMER CEMENTS. 1994.

(3) Fernández-Jiménez, A., Palomo, A. Composition and microstructure of alkali activated fly ash binder: Effect of the activator. Cement and Concrete Research. 2005, Vol. 35, No. 10, pp. 1984–1992.

(4) Palomo, A., Krivenko, P., Garcia-Lodeiro, I., Kavalerova, E., Maltseva, O., Fernández-Jiménez, A. A review on alkaline activation: new analytical perspectives. Materiales de Construcción. 2014, Vol. 64, No. 315, pp. e022.

(5) Raman, C. V., Krishnan, K. S. A New Type of Secondary Radiation. Nature. 1928, Vol. 121, No. 3048, pp. 501–502.

(6) Long, D. A. Raman spectroscopy. New York. 1977, Vol. 1, pp. 310.

(7) Keresztury, G., Chalmers, J. M., Griffith, P. R. Raman spectroscopy: theory. Handbook of vibrational spectroscopy. 2002, Vol. 1, pp. 71–87.

(8) Das, R. S., Agrawal, Y. K. Raman spectroscopy: Recent advancements, techniques and applications. Vibrational Spectroscopy. 2011, Vol. 57, No. 2, pp. 163–176.

(9) Dieing, T., Hollricher, O., Toporski, J. Confocal raman microscopy. Springer Science & Business Media, 2011, ISBN3-642-12521-2.

(10) Toporski, J., Dieing, T., Hollricher, O. Confocal Raman Microscopy. Springer, 2018, ISBN3-319-75380-0.

(11) Bensted, J. Uses of Raman Spectroscopy in Cement Chemistry. Journal of the American Ceramic Society. 1976, Vol. 59, No. 3–4, pp. 140–143.

(12) Black, L. Raman spectroscopy of cementitious materials. Spectroscopic Properties of Inorganic and Organometallic Compounds. 2009, ISBN978-1-84755-918-0. https://doi.org/10.1039/b715000h.

(13) Richardson, I. G., Skibsted, J., Black, L., Kirkpatrick, R. J. Characterisation of cement hydrate phases by TEM, NMR and Raman spectroscopy. Advances in Cement Research. 2010, Vol. 22, No. 4, pp. 233–248.

(14) Garg, N., Wang, K., Martin, S. W. A Raman spectroscopic study of the evolution of sulfates and hydroxides in cement–fly ash pastes. Cement and Concrete Research. 2013, Vol. 53, pp. 91–103.

(15) Loh, H. C., Kim, H. J., Ulm, F. J., Masic, A. Time-Space-Resolved Chemical Deconvolution of

Cementitious Colloidal Systems Using Raman Spectroscopy. Langmuir. 2021, Vol. 37, No. 23, pp. 7019–7031.

(16) Polavaram, K. C., Garg, N. Enabling phase quantification of anhydrous cements via Raman imaging. Cement and Concrete Research. 2021, Vol. 150, pp. 106592.

(17) Polavaram, K. C., Garg, N. Elucidating the Size and Shape of Individual Clinker Phases via Raman Imaging: Impact on Cement Hydration. The Journal of Physical Chemistry C. 2023, Vol. 127, No. 34, pp. 17157–17170.

(18) Polavaram, K. C., Kothari, C., Witte, A. C., Srivastava, S., Kumar, S. R., Samouh, H., Garg, N. Raman Imaging of Cementitious Systems. Smart & Sustainable Infrastructure: Building a Greener Tomorrow. Springer Nature Switzerland, 2024, pp. 896‑907.

(19) Böke, N., Birch, G. D., Nyale, S. M., Petrik, L. F. New synthesis method for the production of coal fly ash-based foamed geopolymers. Construction and Building Materials. 2015, Vol. 75, pp. 189–199.

(20) Caggiani, M. C., Coccato, A., Barone, G., Finocchiaro, C., Fugazzotto, M., Lanzafame, G., Occhipinti, R., Stroscio, A., Mazzoleni, P. Raman spectroscopy potentiality in the study of geopolymers reaction degree. Journal of Raman Spectroscopy. 2022, Vol. 53, No. 3, pp. 617–629.

(21) McKeown, D. A., Galeener, F. L., Brown, G. E. Raman studies of Al coordination in silica-rich sodium aluminosilicate glasses and some related minerals. Journal of Non-Crystalline Solids. 1984, Vol. 68, No. 2, pp. 361–378.

(22) Krol, D. M., Alton, A. C., Rabinovich, E. M. Raman study of the structure of sodium aluminosilicate gels. Journal of Non-Crystalline Solids. 1991, Vol. 130, No. 2, pp. 182–186.

(23) Hehlen, B., Neuville, D. R. Raman Response of Network Modifier Cations in Alumino-Silicate Glasses. The Journal of Physical Chemistry B. 2015, Vol. 119, No. 10, pp. 4093–4098.

(24) Japan Society of Civil Engineers. Concrete Engineering Series No. 132 “Report of the Research Subcommittee for the Promotion of Practical Application of Geopolymer Technology in Civil Engineering”. 2022.

(25) Bellum, R. R., Muniraj, K., Indukuri, C. S. R., Madduru, S. R. C. Investigation on Performance Enhancement of Fly ash-GGBFS Based Graphene Geopolymer Concrete. Journal of Building Engineering. 2020, Vol. 32, p. 101659.

(26) Yang, T., Zhu, H., Zhang, Z. Influence of fly ash on the pore structure and shrinkage characteristics of metakaolin-based geopolymer pastes and mortars. Construction and Building Materials. 2017, Vol. 153, pp. 284–293.

(27) Yeqing, S., Min, D., Anqun, L. Structural evolution of hydrated cement compacts. Materials and Structures. 2011, Vol. 44, No. 10, pp. 1735–1743.

(28) Kirubajiny, P., Marita, B., Jay, S., Pathmanathan, R., Singh, C. D. Durability Performance of

Precast Fly Ash–Based Geopolymer Concrete under Atmospheric Exposure Conditions. Journal of Materials in Civil Engineering. 2018, Vol. 30, No. 3, p. 04018007.

(29) Chen, S., Ruan, S., Zeng, Q., Liu, Y., Zhang, M., Tian, Y., Yan, D. Pore structure of geopolymer materials and its correlations to engineering properties: A review. Construction and Building Materials. 2022, Vol. 328, p. 127064.

CHAPTER 5. CONCLUSION

5.1. Proposal for concrete with both high radio transparency and sufficient mechanical performance

Based on the findings presented in CHAPTER 2, CHAPTER 3, and CHAPTER 4, this section proposes a concrete material that possesses high radio wave transparency while maintaining sufficient mechanical performance as a construction material, along with the process required to achieve this material. The term "mechanical performance" in this context refers not only to the mechanical properties of the structural component but also to its time-dependent deformation characteristics. Ensuring sufficient mechanical performance means that the material must exhibit adequate mechanical properties as a structural component while simultaneously minimizing time-dependent deformation, thereby preventing cracking and maintaining both radio wave transparency and mechanical performance over an extended period.

Findings from CHAPTER 2 indicate that in order to enhance the radio wave transparency of a plain concrete component while preserving its mechanical properties, using low W/P geopolymer (GP) as the binder is effective, and further improvements can be expected through drying treatment. Furthermore, results from CHAPTER 3 reveal that low W/P GP exhibits minimal shrinkage, which suggests a high potential for reducing shrinkage-induced cracking. Consequently, concrete that achieves both high radio wave transparency and mechanical performance while simultaneously suppressing time-dependent deformation, which can lead to cracking, can be concluded as "concrete utilizing GP with an extremely low W/P ratio as the binder."

The creep characteristics of low W/P GP have been partially clarified in CHAPTER 3, and it is expected that predicting its creep behavior when applied to structures will be relatively straightforward. Additionally, as discussed in Sub-section 3.5.2, the creep behavior of low W/P GP can potentially be controlled through appropriate drying treatment of structural components. Although a significant amount of water remains within the solidified GP due to its dehydration reaction, its dense internal structure inhibits moisture migration under no-load conditions. However, when subjected to loading, water gradually migrates from larger pores to finer pores, leading to creep deformation. Therefore, by adjusting the internal water content of the component before load application through drying treatment, the amount of moisture displaced under loading can be regulated, ultimately allowing for creep control. Drying treatment is effective not only for improving radio wave transparency but also for reducing the risk of drying-induced cracking due to the minimal shrinkage observed in GP. As indicated in Sub-sections 2.8.2 and 3.3.2, the low W/P GP proposed in this study requires heating during manufacturing and must undergo heat curing, suggesting that its application as a precast component is appropriate. This further implies that the introduction of drying treatment is relatively feasible. By applying drying treatment to precast components and optimizing the drying conditions, it is expected that concrete components with controlled radio wave transparency and creep characteristics can be

realized.

Furthermore, by applying the microscale analysis method proposed in CHAPTER 4 to various types of GP, including low W/P GP, it is expected that a systematic understanding of the relationship between mixture and curing conditions and the resulting microstructure can be established. Furthermore, by integrating the analytical results obtained through the proposed method with other analytical data, such as porosity and chemical composition obtained from different analysis methods, along with macroscopic property measurements (e.g., radio wave transparency, compressive strength, shrinkage, and creep), a more detailed understanding of the relationship between manufacturing conditions and macroscopic properties can be achieved. Through this process, the mechanisms governing macroscopic properties can be elucidated, ultimately leading to the development of methods for controlling macroscopic properties via microstructural regulation. This would ensure that the performance of low W/P GP is substantiated by microstructural mechanisms and that its properties can be consistently maintained through microstructural control. Therefore, building upon the findings of CHAPTER 4, the applicability of low W/P GP to concrete structural components is expected to be further enhanced.

5.2. Future prospects

As described in Sections 2.9, 3.6, and 4.5, this study has not yet fully elucidated the mechanisms underlying radio wave shielding and the enhancement of radio wave transparency in concrete, the comprehensive time-dependent deformation characteristics of GP and their governing mechanisms, or the mechanisms of GP microstructure formation. To establish methodologies for improving the radio wave transparency of concrete and controlling its time-dependent deformation characteristics, extensive data collection and accumulation on concrete's internal structure, moisture content, and radio wave transparency are necessary. Additionally, further research is required to expand data on the time-dependent deformation of GP, clarify moisture migration mechanisms within GP, and improve the accuracy of the proposed microscale analysis methods while accumulating data under various conditions. Considering practical manufacturing processes, improving the workability of low W/P GP is also essential.

Moreover, the properties of concrete incorporating aggregates need to be examined. This study has primarily focused on improving the radio wave transparency of cementitious phases, which predominantly govern the radio wave shielding characteristics of concrete. However, for practical application in structural components, factors such as aggregate content, type, and shape may significantly influence radio wave transparency and should be thoroughly investigated. Changes in these aggregate-related parameters also affect the mechanical properties of the concrete, meaning that balancing mechanical performance and radio wave transparency will remain a crucial consideration.

As mentioned in Section 1.2, when concrete is used as a construction material, reinforcement is

incorporated to compensate for its low tensile strength. However, reinforcement itself also contributes to radio wave shielding. Thus, in order to realize reinforced concrete components with high radio wave transparency, it is necessary to evaluate the radio wave transmission characteristics of both the concrete and the reinforcement. As seismic design standards become more stringent, reinforcement ratios tend to increase, leading to enhanced mechanical performance while potentially reducing radio wave transparency. On the other hand, strategically placing reinforcement according to the properties of radio waves could enable flexible control over the radio wave transparency of structural components. Investigating this aspect may lead to the development of construction materials capable of actively controlling both mechanical and radio wave transmission properties.

Such a new construction material would not only be useful for newly constructed buildings but also be applicable to existing structures through renovation methods such as partial wall replacement. This could further lead to the development of innovative repair and retrofit techniques. Consequently, future research should focus on developing reinforced concrete that allows for controllable radio wave transparency by optimizing both the material and placement of reinforcement, with low W/P GP serving as the base material. Specifically, adjusting the material, diameter, and spacing of reinforcement according to radio wave characteristics could significantly reduce transmission losses or selectively allow the passage of radio waves within specific frequency bands. By evaluating the changes in radio wave transparency due to variations in reinforcement material, diameter, spacing, and frequency, it will be possible to propose optimal reinforcement configurations for different frequency ranges.

In addition to evaluating radio wave transparency, it is also necessary to consider the mechanical performance of reinforced concrete, including reinforcement strength and prestressing effects. This will contribute to the development of reinforced concrete components that achieve a high-level balance between mechanical performance and radio wave transparency, ultimately leading to an advanced design methodology for construction materials with tunable electromagnetic properties.

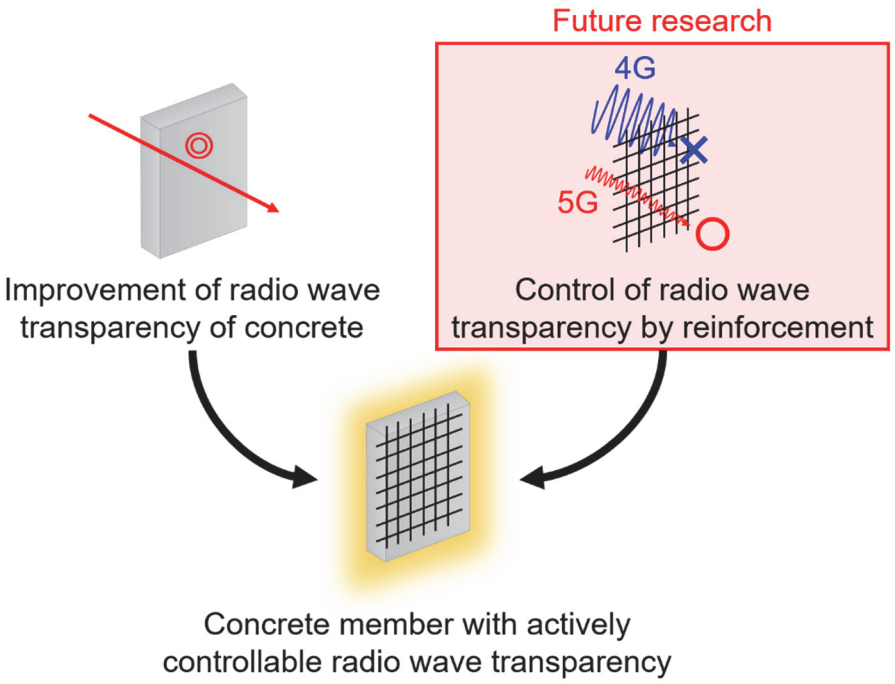

Figure 5-1 Schematic diagram of the research concept and the positioning of the future research

APPENDIX

APPENDIX 1. RADIO WAVE TRANSPARENCY UNDER VARIOUS CONDITIONS

Here, the results of radio wave transmission tests conducted under various conditions are presented, specifically those that were not included in CHAPTER 2.

A1.1. Effect of moisture absorption

To examine changes in radio wave transparency after moisture absorption following drying treatment, measurements were performed under RH0% conditions for all four specimens shown in CHAPTER 2 (W/P55% cement paste specimen, W/P55% cement mortar specimen, W/P15% cement paste specimen, and W/P15% GP specimen). Subsequently, the specimens were placed in a constant temperature and humidity chamber set at 20°C and RH40% for more than two weeks until weight stabilization, after which radio wave transmission tests were conducted again. For three specimens, excluding the W/P15% GP specimen, transmission loss was measured at 6 GHz, 10 GHz, and 33 GHz, whereas for the W/P15% GP specimen, only the transmission loss at 33 GHz was measured.

Figure A1-1 shows the transmission loss of each specimen measured in the radio wave transmission tests, alongside the results obtained under RH40% (before drying) and RH0% conditions. From **Figure A1-1**, it can be observed that even when the dried specimens were placed back in an environment with the same RH as before drying, their radio wave transparency did not return to the original state. Additionally, for the W/P55% cement paste and W/P55% cement mortar specimens, an increase in RH after drying led to an increase in transmission loss, indicating a decrease in radio wave transparency. However, for the W/P15% cement paste and W/P15% geopolymer specimens, an increase in RH after drying did not result in an increase in transmission loss. This suggests that due to the extremely low pore volume at low W/P, moisture absorption was suppressed, maintaining the internal dry state.

Thus, adopting a low W/P ratio can help stabilize radio wave transparency against humidity fluctuations, implying that in practical applications, after drying treatment, maintaining a certain level of radio wave transparency may be feasible even without additional waterproofing treatments.

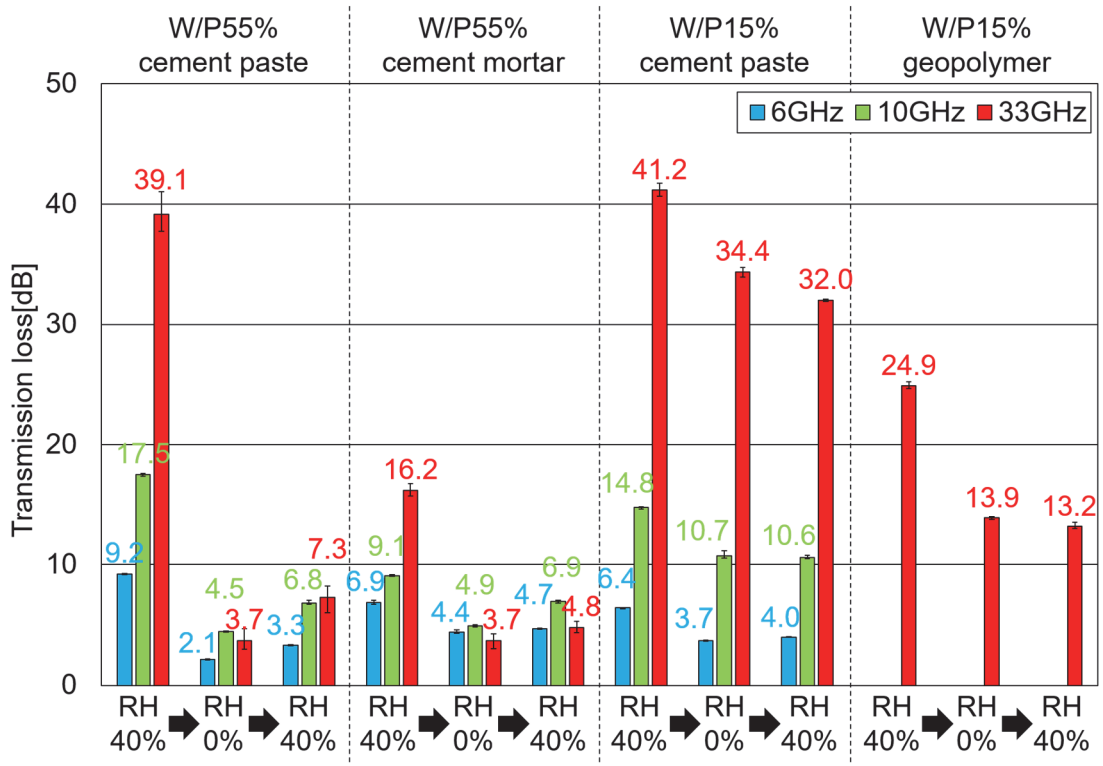

Figure A1-1 Transmission loss after moisture absorption

A1.2. Effect of aggregate size

To investigate the effect of aggregate size on radio wave transparency, a cement mortar specimen was prepared using the same mix as the W/P55% cement mortar in CHAPTER 2 but with sand particles larger than 2.5 mm as the only aggregate. The same radio wave transmission test procedure was applied. Transmission loss was measured at 6 GHz, 10 GHz, and 33 GHz, and, similar to Section A1.1, measurements were taken under RH40% and RH0% conditions, followed by another measurement under RH40% conditions.

Figure A1-2 presents the transmission loss results obtained from the radio wave transmission tests. It is evident that when only larger sand particles were used, the transmission loss was significantly lower than that of the mortar with a standard particle size distribution. However, this result is likely due to material segregation caused by low viscosity, leading to a highly porous internal structure rather than the effect of particle size itself. Indeed, large voids were visually observed on the specimen's surface immediately after demolding (**Figure A1-3**), and the compressive strength was exceptionally low at less than 10 N/mm². This indicates that the physical properties of the cementitious matrix differed significantly between the specimen with standard particle size distribution and the one with only large sand particles. Consequently, the effect of aggregate size on radio wave transparency was not clearly identified in this study, necessitating further investigation with improved testing conditions.

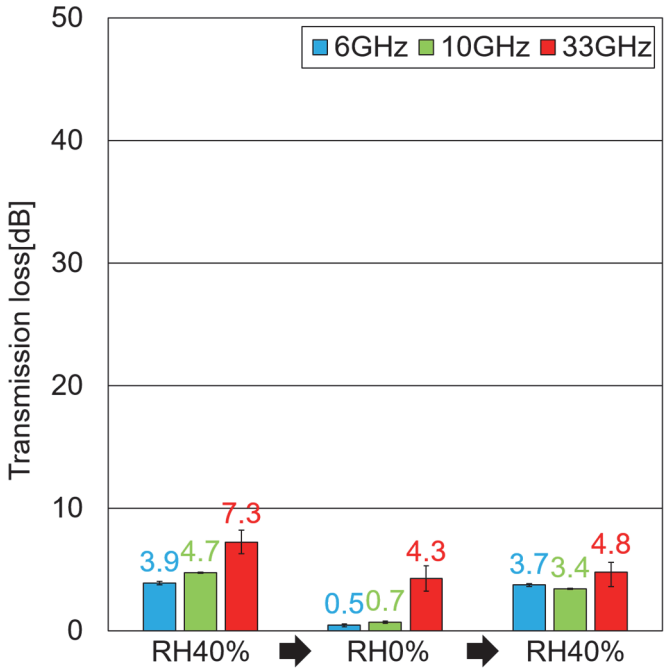

Figure A1-2 Transmission loss of W/P55% cement mortar specimen with large particle size sand

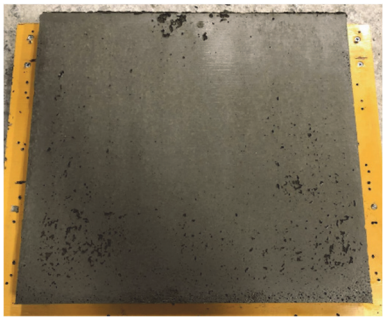

Figure A1-3 W/P55% **c**ement mortar specimen with large particle size sand

A1.3. Effect of aggregate in geopolymer

To examine the radio wave transparency of GP with added aggregates and the influence of aggregate type on radio wave transparency, mortar specimens were prepared using GP as the binder, incorporating either ordinary aggregate (crushed sand) or Coal Gasification Slag (CGS) in the same volume. The materials used in the specimens are listed in **Table A1-1** and Table A1-2, while the mix proportions are presented in Table A1-3. Unlike the low W/P mixtures in CHAPTER 2, the mix used here was based on the standardized mix conditions defined by the "361 Committee for Promoting the Practical Use of Geopolymer Technology in Civil Engineering" of the Japan Society of Civil Engineers[(1)], with a slight reduction in unit water content. To ensure workability, crushed sand with

particle sizes greater than 2.5 mm was used, as in Section A1.2. Transmission loss was measured at 6 GHz, 10 GHz, and 33 GHz, following the same testing sequence as in Section A1.1, with measurements first taken under RH0% conditions, followed by RH40%. However, the environmental conditions during the first test differed; the CGS-based specimen was tested under RH40% conditions, whereas the crushed sand specimen was tested immediately after demolding, meaning that the interior of the specimen was assumed to be water-saturated (≈ RH100%).

CGS is a vitreous slag byproduct of Integrated Gasification Combined Cycle (IGCC) coal-fired power plants. Common characteristics of CGS include its glassy, smooth-surfaced particles, minimal internal porosity, low water absorption compared to ordinary aggregates, high elasticity modulus, and brittle nature (it can be crushed with a hammer). The key properties of CGS relevant to this study are its glassy composition and extremely low water absorption. Since glass generally exhibits excellent radio wave transparency, CGS, being glassy, was expected to provide similar benefits. Furthermore, its low water absorption suggests that it could help reduce internal moisture content compared to ordinary aggregates, potentially improving radio wave transparency.

The transmission loss results obtained from the radio wave transmission tests are shown in **Figure A1-4**. It can be observed that adding aggregates to GP improved radio wave transparency compared to low W/P GP without aggregates. Although a direct comparison is difficult due to differences in mix proportions, this suggests that, similar to cementitious materials, adding aggregates to GP could further enhance radio wave transparency. However, when comparing the specimens using CGS and crushed sand as aggregates, the transmission loss for radio waves at 33 GHz was lower in the crushed sand-based specimen, indicating higher radio wave transparency. A comparison of the chemical compositions of CGS and crushed sand (hard sandstone) (**Table A1-4**) reveals a significant difference in SiO_2 content, with crushed sand containing approximately twice as much SiO_2 as CGS. This suggests that using crushed sand may yield superior radio wave transparency. Additionally, since CGS is glassy and has a smooth surface, it likely exhibits weaker adhesion to GP than crushed sand, potentially leading to discontinuities at the GP-CGS interface, which may hinder radio wave propagation. As higher frequency waves have shorter wavelengths and are more susceptible to small-scale discontinuities, it is likely that while 6 GHz and 10 GHz waves were not significantly affected by the aggregate interface, 33 GHz waves were more strongly impacted. Furthermore, since CGS contains a certain amount of calcium components, it may react with the alkali in the geopolymer, leading to the formation of hydration products around the aggregate. The non-evaporable water contained in these hydration products is likely contributing to radio wave shielding.

Contrary to expectations, the results indicate that CGS does not significantly improve radio wave transparency and may even reduce it at higher frequencies.

Table A1-1 Materials of geopolymer mortar specimen

Type	Name	Mark	Ingredients / Physical properties
Active Filler (P)	Fly ash	FA	JIS Type II Specific surface area: 3690 cm^2/g Specific gravity: 2.29 g/cm^3
Alkaline solution (L)	Sodium silicate solution	SS	Listed in **Table A1-2**
	Sodium hydroxide	SH	Granular, Purity: 98.0% or higher
	Water	LW	Deionized water
Fine aggregate	CGS	S	From Nakoso IGCC power plant, Fukushima Surface dry density: 2.79 g/cm^3 Water absorption rate: 0.25-0.29%
	Crushed sand		Hard sandstone from Hachioji, Tokyo Surface dry density: 2.65 g/cm^3 Water absorption rate: 1.30%
Chemical admixture	Superplasticizer	SP	Polycarboxylic acid ether-based

Table A1-2 Ingredients and physical properties of sodium silicate solution manufactured by FUJIFILM Wako Pure Chemical Corporation

Test case	Specified value
Iron (Fe)	～0.03%
Sodium oxide (Na_2O)	17.0～19.0%
Silicon dioxide (SiO_2)	35.0～38.0%
Molar concentration (SiO_2/Na_2O)	2.06～2.31
Concentration	52.0～57.0%

Table A1-3 Mix proportions of geopolymer mortar specimens (TW: Total water volume)

Type of fine aggregate	Unit weight (kg/m^3)							A/W	Si/A
	P	L			S	SP	TW		
	FA	SS	SH	LW					
CGS	586	165	19	102	1462	0	86.3	0.297	0.707
Crushed sand	566	165	19	102	1412	P× 1.0%	86.3	0.297	0.707

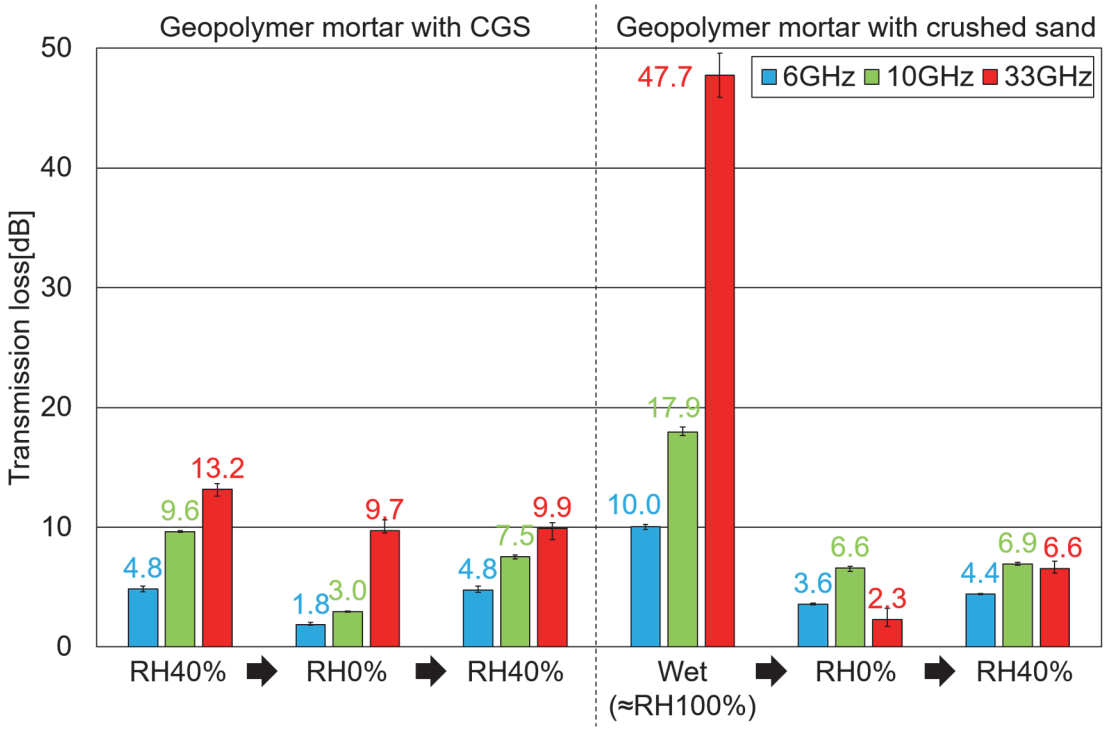

Figure A1-4 Transmission loss of geopolymer mortar specimens

Table A1-4 Chemical composition of fine aggregates

Ingredient	Content (%)	
	CGS	Crushed sand (Average of Honshu-directed oblique sandstone)[2]
SiO_2	31.2-33.5	72.27
Al_2O_3	19.0-19.9	11.91
CaO	16.6-17.6	2.43
Fe_2O_3	5.0-5.1	0.71
K_2O	0.62-0.70	2.04
TiO_2	1.5	0.39
MgO	3.2-3.7	1.18
SO_3	0.79-0.86	-
SrO	1.1	-
MnO	0.06-0.07	0.06
ZnO	<0.01	-
P_2O_5	0.30-0.31	0.08
Na_2O	10.5-11.1	-
FeO	-	2.14
Na_3O	-	3.22
H_2O+	-	1.72
H_2O-	-	0.23
CO_2	-	2.31
C	-	0.11

A1.4. Effect of coating

As shown in Section A1.1, even if drying treatment initially enhances radio wave transparency, subsequent moisture absorption may deteriorate it again. For practical applications as construction materials, it is necessary to maintain high radio wave transparency under typical humidity conditions while preventing fluctuations due to humidity changes. The simplest and most effective approach to achieving this goal is surface coating, which was applied in this study. A surface coating material that prevents moisture ingress while allowing radio waves to pass through was selected and applied to the specimens used in the Section A1.3 investigation. The specific surface coatings used are listed in **Table A1-5**.

The experimental procedure was as follows. First, the specimens tested under RH40% (after drying) conditions in Section A1.3 were dried again in a RH0% chamber for more than two weeks. Next, the surface coating material was applied to the dried specimens, and after the coating hardened,

the specimens were placed in a constant temperature and humidity chamber set at 20°C and RH40% for approximately two weeks before conducting radio wave transmission tests. Before and after chamber placement, specimen weight was measured to confirm that no moisture absorption had occurred. Finally, after being submerged in water for over two weeks, the specimens underwent another round of radio wave transmission tests.

Figure A1-5 presents the transmission loss results obtained from these tests. Comparing **Figure A1-4** and **Figure A1-5**, the glass-coated specimen (Geopolymer mortar with CGS) showed no significant difference in transmission loss between RH0% and RH40% (after drying), indicating no clear moisture suppression effect from the glass coating. In contrast, the epoxy resin-coated specimen (Geopolymer mortar with crushed sand) exhibited less increase in transmission loss following humidity exposure compared to the uncoated specimen, demonstrating that epoxy resin coating effectively suppressed moisture absorption and maintained radio wave transparency. However, after prolonged water immersion, transmission loss increased significantly regardless of the surface coating material, suggesting that the tested coatings lost their moisture-blocking effect in continuously wet conditions. Nevertheless, the epoxy resin-coated specimens exhibited lower transmission loss than the glass-coated ones after water immersion, indicating that the epoxy resin coating provided some degree of moisture resistance.

Table A1-5 Surface coating materials

Specimen	Coating type	Ingredients / Physical properties
Geopolymer mortar with CGS	Glass coating	Two-component hybrid coating agent, Completely inorganic (ハイバリアー, AQ SHIELD)
Geopolymer mortar with crushed sand	Epoxy coating	Two-component epoxy resin primer (R Primer, SHO-BOND)

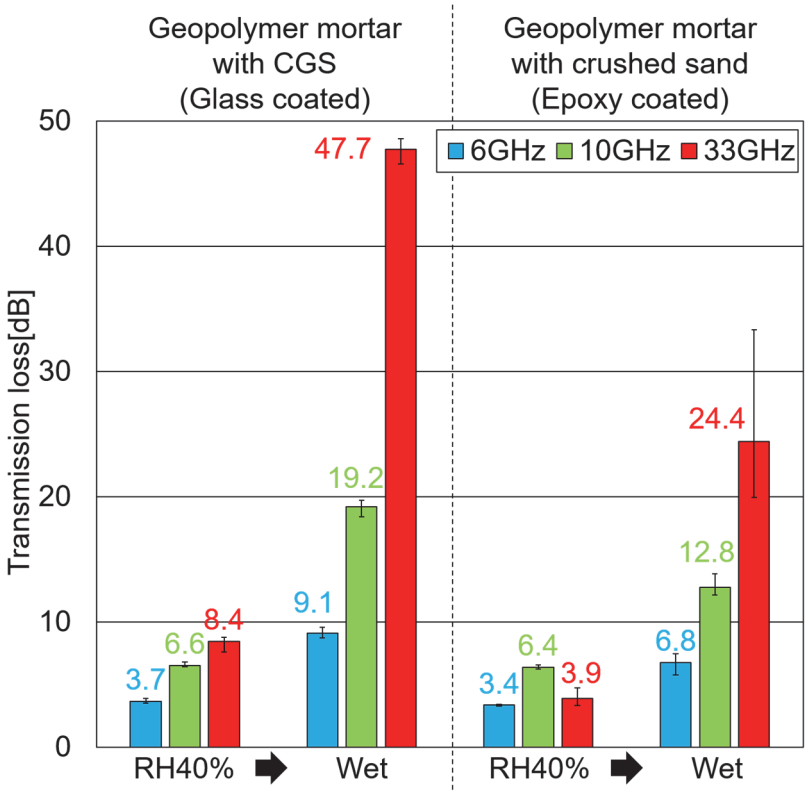

Figure A1-5 Transmission loss of coated geopolymer mortar specimens

APPENDIX 2. PROPOSAL OF VOLUME CHANGE MEASUREMENT METHOD

This section describes an analytical method discovered during the investigation in CHAPTER 4, which has the potential to serve as a novel technique for measuring volume changes in cementitious materials. As stated in Sub-section 4.3.1, when conducting *in situ* observations of cementitious materials using confocal Raman microscopy (CRM), it is necessary to optically adjust the focus in response to the volumetric changes of the sample to maintain a consistent focal plane across all scans. This requirement suggests that measuring the temporal changes in the focal position could enable the quantification of the sample's volumetric changes.

In cementitious materials, volumetric changes are primarily governed by post-solidification deformations. Numerous instruments, such as strain gauges and dilatometers, are available for measuring volumetric and length changes in solidified materials. However, these instruments cannot track deformations in fluidic substances, making them unsuitable for use with uncured materials. Existing methods for measuring volumetric changes from the fresh to the hardened state typically involve monitoring the displacement of the upper or side surfaces of specimens placed in sealed containers or molds. This approach is standardized in ASTM C1608-17 as a method for measuring the chemical shrinkage of cement paste. While such methods allow for overall volumetric change measurements, they are not capable of capturing localized volumetric changes at the microscale or identifying their underlying causes. CRM, on the other hand, enables nanometer-scale positioning in the height direction, allowing for the measurement of volumetric changes in specific microstructures or different compositional regions. Furthermore, CRM can simultaneously track phase transitions and microstructural changes occurring within the sample due to ongoing reactions. Therefore, CRM has significant potential as a powerful tool for analyzing volumetric change behavior in greater detail while simultaneously elucidating its underlying mechanisms.

To explore the applicability of CRM as a volumetric change measurement technique for geopolymers (GP), additional experiments were conducted under various conditions, including those used in CHAPTER 3, beyond those examined in CHAPTER 4. The sample conditions are listed in **Table A2-1**, and the mix proportions are provided in Table A2-2. The materials used were the same as those described in CHAPTER 4. Although valid Raman images were not obtained for some conditions, the corresponding data have been omitted from this thesis. **Figure A2-1** presents the temporal changes in the optical focal position (focus shift), referenced to the initial scan where the focus was aligned. Here, focus shift represents changes in the height of the sample's upper surface, where a positive focus shift indicates expansion, and a negative shift suggests shrinkage or settlement of the sample.

Figure A2-1 demonstrates that the focus shift behavior varies significantly depending on the mix proportions and curing conditions, indicating that this method effectively captures differences in volumetric change behavior due to these parameters in uncured materials. Notably, positive values

were observed only in the heated samples ("Normal," "Si Rich," and "SH Only"), confirming that this method successfully detects thermal expansion in response to heating.

Thus, measuring the temporal changes in the optical focal position using CRM suggests a high potential for continuously tracking the volumetric changes of materials from the fresh to the hardened state. In this study, the optical focal position was used as the reference; however, CRM also offers a "Raman focus," where the Raman spectral peak intensity is maximized. For materials with crystalline phases, using the Raman focus as a reference could enable even more precise measurements. Furthermore, by integrating this approach with CRM's primary function of chemical analysis, it becomes possible to simultaneously measure phase transitions and microstructural changes occurring during reactions. Consequently, CRM-based analysis is expected to provide comprehensive insights into the volumetric change behavior of cementitious materials at the microscale, along with its underlying mechanisms.

Table A2-1 Conditions of samples for volume change measurement using CRM

	Alkali/Water	Silica/Alkali	Liquid/Powder	Curing Temp.
Normal	0.125	0.700	0.90	60℃
Normal (Room Temp)				Room(≃20℃)
Si Rich	0.108	1.046		60℃
SH Only	0.162	0		
Cement	-	-	0.90	Room(≃20℃)

Table A2-2 Mix proportions of geopolymer samples for volume change measurement using CRM

	Unit volume(kg/m^3)					A/W	Si/A	L/P
	P	L						
	FA	SS	SH	LW	TW			
Normal	1237	412	65	148	405	0.125	0.700	0.90
Si Rich	1237	535	36	74	407	0.108	1.046	0.90
SH Only	1237	0	146	405	405	0.162	0	0.90

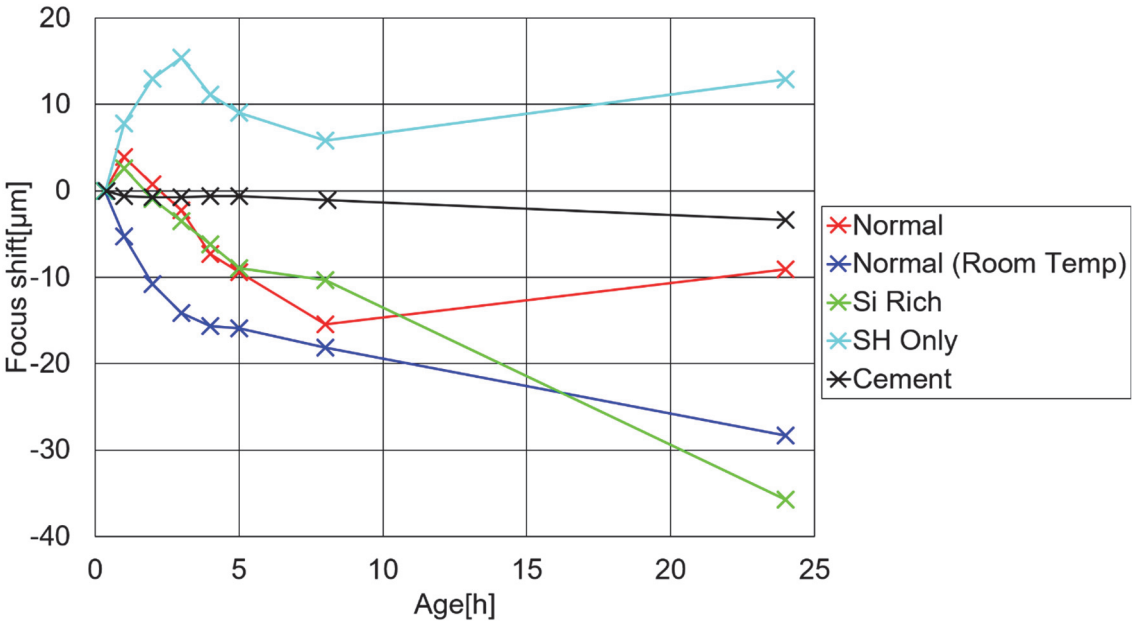

Figure A2-1 Time variation of focus shift for each sample

References

(1) 土木学会. コンクリート技術シリーズ No.132 土木分野におけるジオポリマー技術の実用化推進のための研究小委員会（361 委員会）成果報告書. 2022.

(2) Kataoka, M., Teraoka, Y. Chemical Composition of Sandstones in Japan. Annual report of the Faculty of Education, University of Iwate. 1981, Vol. 40, No. 2, pp. 55‐66.